



**HAL**  
open science

# Local shear rearrangements in glassy systems : from micromechanics to structural relaxation in supercooled liquids

Matthias Lerbinger

► **To cite this version:**

Matthias Lerbinger. Local shear rearrangements in glassy systems : from micromechanics to structural relaxation in supercooled liquids. Physics [physics]. Université Paris sciences et lettres, 2020. English. NNT : 2020UPSL006 . tel-03151944

**HAL Id: tel-03151944**

**<https://pastel.hal.science/tel-03151944>**

Submitted on 19 Mar 2021

**HAL** is a multi-disciplinary open access archive for the deposit and dissemination of scientific research documents, whether they are published or not. The documents may come from teaching and research institutions in France or abroad, or from public or private research centers.

L'archive ouverte pluridisciplinaire **HAL**, est destinée au dépôt et à la diffusion de documents scientifiques de niveau recherche, publiés ou non, émanant des établissements d'enseignement et de recherche français ou étrangers, des laboratoires publics ou privés.



**THÈSE DE DOCTORAT**

**DE L'UNIVERSITÉ PSL**

Préparée à l'ESPCI Paris au laboratoire PMMH,  
Physique et Mécanique des Milieux Hétérogènes

**Local shear rearrangements in glassy systems:  
From micromechanics to structural relaxation in  
supercooled liquids**

**Réarrangements locaux dans les verres:  
des propriétés micromécaniques aux processus de  
relaxation structurale dans les liquides surfondus**

Soutenue par

**Matthias Lerbinger**

Le 20 Novembre 2020

École doctorale n°564

**Physique en Île-de-France**

Spécialité

**Physique**

Composition du jury :

David Rodney Professeur, Université Lyon 1	<i>Président, Rapporteur</i>
Andreas Heuer Professeur, Universität Münster	<i>Rapporteur</i>
Leticia Cugliandolo Professeur, Sorbonne Université	<i>Examinatrice</i>
Beatrice Ruta Chargée de recherche, Université Lyon 1	<i>Examinatrice</i>
Damien Vandembroucq Directeur de recherche, ESPCI	<i>Directeur de thèse</i>
Sylvain Patinet Chargé de recherche, ESPCI	<i>Co-Directeur de thèse</i>



---

# Acknowledgements

First, I would like to thank my two advisors Damien and Sylvain. I am very grateful that they were always for advice and answered my questions with great patience. Their guidance was essential for the success of this thesis and I am very thankful for all the things they taught me along the way. It was my great pleasure working with them together. I am very thankful for the many fruitful scientific and non-scientific discussions I had with the other group members Armand, David and Dheeraj. Particularly Armand was a very good ally in all circumstances over the full course of the thesis.

The time at PMMH would have been much less pleasant without my fellow labmates: thank you very much Benoît, Gaspard, Hector, Jean and PH for welcoming me in your office which quickly become our office. Thank you for introducing me to the regular coffee breaks, which would have not been the same without Manon.

I would not have come so far without my family, especially my parents, sisters Marie and Alica. Throughout the three years, I have had nothing but unconditional support and encouragement from them and none of this would have been possible without them. It is so much easier to reach for your goals when you know you will have someone in your corner.

Lastly, I am much obliged to my sister Alicia for proofreading the manuscript multiple times, correcting typos and improving its readability tremendously by adding commata.



---

# Preface

In the 20<sup>th</sup> century, a lot of progress was made in understanding the physics of solids. The greatest advance was achieved for materials characterized by long range atomistic order. However, only a portion of condensed matter shows a long range atomistic order. In the solid phase, many materials are characterized by a lack thereof. These materials are called amorphous. This class of matter does not crystallize at the melting temperature. Instead, it keeps its liquid nature and enters the supercooled regime. In this regime, upon further cooling, the kinetics of the system drastically slow down. At one point, the dynamics have slowed down so much, that the cooling rate is too fast for the kinetics of the system. As a consequence, the system cannot remain in the equilibrium phase and as a result, falls out of it and forms a glass. This describes, in short, the glass transition. In addition to the dynamic slowdown, a series of other phenomena start to appear in the supercooled regime, for instance, dynamical heterogeneities and non-exponential relaxation.

Despite decades of research efforts, to date there exists no theory that describes the glass transition and its attendant phenomena in its entirety. Moreover, in 1995, Nobel prize laureate P. W. Anderson called the glass transition “the deepest and most interesting unsolved problem in solid state theory” [5]. Still, progress has been made: first, there exist now well-established theories that capture the glass transition partially. Most of them focus either on the thermodynamic or dynamic nature of the transition; yet, there are also other concepts trying to explain the kinetic behavior using the mechanical properties of the system. Second, it was possible to identify similar phenomena accompanying the glass transition in other kinds of systems, for example the jamming transition in granular material. This hints at a more universal nature of the underlying transition. Third, it was shown, that dynamical heterogeneities, a key feature of glassy dynamics, can be directly related to the underlying structure. This discovery opened up the search for structural indicators which explain the kinetic behavior of glasses. In the last 10-15 years, a flurry of structural indicators has been proposed, ranging from a coarse grained description of the structure to complex pair correlation functions. Some of them achieve a high degree of correlation between dynamics and structure. However, the vast majority of them does not allow any conclusion on the nature of the fundamental process of structural relaxation. Yet, an answer to this question may lead the way to new theoretical ideas to elucidate the glass transition.

To answer this question, a different point of view is adopted in this thesis: a highly viscous liquid is regarded as a flowing solid. This perspective roots in the potential energy description of liquids. To support this interpretation of liquids, extensive numerical simulation of glass forming liquids are

---

performed. The structure of the glassy systems is characterized through the local yield stress method. In the first part, the real space measurement of local yield stresses demonstrates the encoding of a discrete and finite number of shear transformations into the structure of a glass. In the second part, local slip thresholds are linked to structural relaxation in the supercooled regime.

This manuscript is organized as follows: in chapter [1](#), the glass transition and its accompanying phenomena are introduced. Additionally, some theoretical concepts that were proposed over the last decades to explain the glass transition are shortly described. Furthermore, a few structural indicators, which were previously used to relate glassy dynamics to the amorphous atomistic structure are reviewed. Chapter [2](#) gives an overview of the details for the two dimensional model system as well as the principal computational methods which have been used throughout this work. The scientific results of this thesis are presented in the chapters [3](#) and [4](#). In the former, the focus is on the micromechanical response of a small piece of glass in the athermal, quasistatic limit. In the latter, a strong connection between the structure, characterized through local mechanical properties, and equilibrium dynamics of a supercooled liquid is established. The article in appendix [A](#) is on a related subject: the evolution of local yield stresses during shear banding is examined.

---

# Résumé

Sous l'effet d'un refroidissement lent, un liquide subit à sa température de fusion une transition de phase pour former un cristal. Cette cristallisation peut être évitée si le refroidissement se fait suffisamment rapide. Dans ce cas, le liquide entre dans le régime surfondu. Dans ce régime, lors d'une nouvelle diminution de la température, la viscosité augmente de plusieurs ordres de grandeur sur une petite plage de températures. Les réarrangements atomiques ou moléculaires finissent par prendre de plus en plus de temps et le retour à l'équilibre n'est plus permis par la vitesse de refroidissement; le système finit donc par tomber hors équilibre et forme un solide amorphe : un verre. Par convention, ce changement d'état définit la transition vitreuse. Par conséquent, la question se pose de savoir ce qui provoque un ralentissement aussi drastique de la dynamique ? En physique, les divergences de longueur et d'échelle de temps sont en général des indicateurs d'une transition de phase. La transition vitreuse est-elle une transition purement dynamique d'une "dynamique liquide" à une "dynamique vitreuse" ou le changement drastique dans les observables dynamiques décrits ci-dessus est-il une conséquence d'un changement fondamental de l'état fluide à un état vitreux idéal ? En d'autres termes, la transition vitreuse est-elle une transition de phase cinétique ou thermodynamique ? La transition vitreuse s'accompagne d'un certain nombre de phénomènes complexes, notamment l'apparition d'hétérogénéités dynamiques, la relaxation non exponentielle et la croissance super-Arrhénienne des quantités de transport.

Le premier chapitre commence par un panorama des études sur la transition vitreuse et des discussions sur la nature de la transition elle-même. Ensuite, les phénomènes mentionnés ci-dessus sont exposés et discutés. Au cours des dernières décennies, des idées théoriques variées ont été proposées pour décrire la transition vitreuse. Les concepts théoriques les plus pertinents pour les chapitres suivants sont exposés dans ce chapitre introductif. Dès les années 1960, Goldstein a proposé un modèle utilisant le paysage d'énergie potentielle pour expliquer le ralentissement cinétique drastique qui accompagne la transition vitreuse. Dans cette description, le système "vit" sur une surface énergétique de grande dimension, le paysage d'énergie potentielle. Au fil du temps, le système se déplace le long du paysage. Un minimum dans l'énergie potentielle est associé à une configuration localement stable. Les minima locaux du paysage sont séparés par des barrières d'énergie. Goldstein propose que le système peut franchir les barrières grâce à des sauts activés. Un tel saut dans l'espace de phase correspond à un réarrangement localisé, n'impliquant qu'une poignée d'atomes dans l'espace réel. Dans l'hypothèse d'une dynamique activée, le temps de saut augmente de façon exponentielle à mesure que la hauteur de la barrière augmente, ce qui explique le ralentissement dynamique. Pourtant, cette théorie échoue à des

---

températures plus élevées, où la hauteur des barrières est comparable à l'énergie thermique. Dans ce régime, la dynamique n'est plus régie par les sauts activés. De plus, le système est en régime fluide.

La théorie du couplage de modes adopte une approche complètement différente : il s'agit d'une théorie *ab initio* qui ne prend en compte que les propriétés statiques et indépendantes du temps. Bien que les données d'entrée soient peu nombreuses, elle décrit correctement le processus de relaxation en deux étapes et trouve un bon accord concernant la forme de la fonction de relaxation des liquides réels. Cette théorie prévoit également une divergence en loi de puissance du temps de relaxation à une température critique. La transition vitreuse réelle est en fait observée à une température beaucoup plus basse. La transition, prédite par la théorie du couplage de modes, n'a jamais été observée ni dans les expériences ni dans les simulations numériques. Cela soulève la question immédiate de savoir pourquoi la théorie prédit une telle transition. La réponse est que la dynamique activée n'est pas prise en compte. Comme la température est abaissée, les dynamiques activées jouent un rôle de plus en plus important, la théorie du couplage de modes ne parvient pas à prédire avec précision le comportement cinétique dans le régime surfondu. Cette divergence entre la théorie et la réalité s'accroît à mesure que l'on se rapproche de la température de transition vitreuse. Adam et Gibbs ont fait valoir que les réarrangements moléculaires sont de nature coopérative. Ainsi, le liquide peut être divisé en régions de réarrangement coopératif. Si la température est abaissée, la taille de ces régions augmente. Chacune de ces régions a accès à un nombre fini de configurations par le biais de réarrangements. En supposant que la barrière énergétique séparant deux configurations est proportionnelle au nombre de particules contenues dans une région, le modèle prédit une transition de phase vers un état vitreux idéal à une température beaucoup plus petite que la transition vitreuse dynamique. Un avantage de cette approche théorique est son élégance et sa simplicité. En outre, elle fournit une explication claire à l'augmentation super-Arrhénienne des temps de relaxation des liquides fragiles. Cependant, cette approche ne permet pas de saisir tous les phénomènes des systèmes vitreux : tout d'abord, aucun concept clair de l'état idéal du verre n'a été proposé. Deuxièmement, elle ne peut pas décrire ce qui se passe à des températures plus élevées - ni le passage d'une dynamique non activée à une dynamique activée, ni la chute hors d'équilibre à la température de la transition dynamique vitreuse. Les théories mentionnées ci-dessus considèrent la transition vitreuse comme une transition purement dynamique ou thermodynamique. Une approche alternative ou complémentaire consiste à adopter un point de vue mécanique pour étudier le ralentissement dynamique. Comme l'accent est mis sur les propriétés mécaniques, le liquide est considéré comme un solide qui s'écoule. Ce point de vue original permet d'utiliser des modèles et des outils qui ont été précédemment développés pour les solides amorphes afin de comprendre le comportement des liquides. Dans cet esprit, un modèle dit de *shoving* (bousculade) a été développé. L'idée principale du modèle est la suivante : l'écoulement dans les liquides visqueux est composé d'une série de réarrangements locaux. Chacun de ces événements se produit sur une courte échelle de temps et n'implique qu'une poignée de particules. Afin de se réarranger, les molécules doivent créer un espace supplémentaire en écartant leurs voisines. On peut montrer que le travail réversible effectué, pour pousser les particules voisines de côté, est proportionnel au module de cisaillement dépendant de la température. Ainsi, le *shoving model* peut expliquer le ralentissement de la dynamique. Cependant, dans l'hypothèse raisonnable où le module de cisaillement reste fini lorsque la

---

température diminue, le modèle de bousculade ne prévoit pas de divergence et de transition de phase correspondante. Une idée commune est qu'en raison de la nature amorphe des verres, seule une mesure locale peut élucider leur comportement mécanique et dynamique. C'est dans cet esprit que l'approche de la matrice gelée a été développée. L'objectif est d'étudier les propriétés mécaniques locales d'un système. Pour ce faire, l'ensemble du système est gelé, à l'exception d'une petite région cible. Sous l'effet d'une contrainte externe, la partie gelée du système, qui ne peut relaxer, subit une déformation affine homogène. À partir de la réponse à la contrainte de la région cible, des observations mécaniques locales sont accessibles, par exemple le module d'élasticité local. La méthode de la limite d'élasticité locale étend les concepts de la matrice gelée. Une nouvelle caractéristique de la méthode de la limite d'élasticité est l'ajout d'une composante tensorielle. La réponse mécanique locale est sondée pour différentes directions de chargement. Cette définition des contraintes locales d'élasticité en fonction de la direction de chargement rend hommage à la structure amorphe des systèmes vitreux. Dans les systèmes désordonnés, les propriétés mécaniques dépendent fortement de la direction de chargement. La relation entre les limites d'élasticité locales et la réponse d'un système soumis à une déformation globale a été examinée. Il a été démontré qu'il existe une excellente corrélation entre les contraintes d'élasticité locales et l'emplacement des réarrangements plastiques forcés par le chargement à distance. Les contraintes d'élasticité locales ont une plus grande capacité à prédire la position des réarrangements que d'autres indicateurs structurels locaux, par exemple la densité locale, l'énergie potentielle locale ou l'ordre local à courte portée. Les contraintes locales d'élasticité sont également plus performantes que les mesures de la réponse linéaire (module de cisaillement et fraction de participation les plus faibles). En outre, la corrélation entre les contraintes de seuils locales et la position des réarrangements dépend de la préparation du système. Plus le système est relaxé, plus la corrélation est élevée et plus elle persiste longtemps. La méthode de la limite d'élasticité locale présente une série d'avantages par rapport à d'autres indicateurs locaux : tout d'abord, il s'agit d'une mesure spatiale réelle. Par conséquent, toutes les observables ont une signification physique directe et n'ont pas besoin d'une interprétation supplémentaire. Un deuxième avantage est donné par son approche non perturbative. Contrairement, par exemple, au calcul des soft modes, il n'y a pas de développement d'ordre supérieur du paysage d'énergie potentiel concerné. Enfin, en raison de la nature locale de la mesure, le système peut être divisé en parties et le calcul des contraintes locales peut être parallélisé pour réduire le temps de calcul nécessaire.

Dans le 2e chapitre, le système modèle 2D ainsi que les principales méthodes de calcul sont présentés. Tout d'abord, les paramètres du potentiel d'interaction pour le liquide formateur de verre, un mélange binaire Lennard-Jones qui a été utilisé tout au long de cette thèse, sont donnés. Ensuite, les détails des protocoles de préparation sont exposés pour obtenir les configurations vitreuses initiales. La première partie du 2e chapitre se termine par une description de méthodes de simulation - soit en appliquant une déformation globale, soit en appliquant une dynamique à l'équilibre thermique. Enfin, l'ensemble iso-configurationnel est présenté. Ensuite, le temps de relaxation du liquide de formateur de verre est estimé pour différentes températures à l'aide de la fonction de diffusion auto-intermédiaire. Une attention particulière est accordée à la dépendance de la taille du système de la fonction de diffusion auto-intermédiaire. Troisièmement, le temps de relaxation est utilisé pour déterminer deux points

---

de référence fondamentaux pour le matériau étudié : la première température de référence est la température de départ (ou “onset temperature” en anglais). Elle marque le point auquel la relaxation non exponentielle commence à s’installer pour un verre de type fragile. Lorsqu’il est refroidi en dessous de la température de départ, le liquide surfondu commence également à ressentir l’influence du paysage d’énergie potentielle sous-jacente et la dynamique activée commence à s’installer. La deuxième température de référence est la température critique de la théorie de couplage de modes. Ce point indique à quel moment la dynamique activée devient le principal mécanisme de diffusion. Dans la quatrième section du 2e chapitre, les états inhérents et la dynamique inhérente sont introduits : la plupart des configurations étudiées sont préparées dans le régime surfondu. Dans ce régime, le système passe la plupart de son temps à vibrer autour d’un minimum local de l’énergie potentielle. Ce n’est que de temps en temps qu’il saute d’un minimum local à un autre. Ces temps de transition sont négligeables par rapport au temps passé à vibrer et doivent être considérés comme instantanés. On attribue à chaque configuration sa structure inhérente correspondante en minimisant l’énergie de la configuration thermalisée. En minimisant toutes les configurations thermalisées, on obtient un deuxième ensemble de configurations définissant la dynamique des états inhérents. En étudiant la dynamique des états inhérents, il est possible de suivre le système d’un minimum local à un autre. Un avantage de cette description est que la dynamique des états inhérents permet de se concentrer sur l’image des liquides sous forme solide. Cinquièmement, la détection des réarrangements atomiques est abordée. Au fil du temps, plusieurs méthodes ont été proposées pour détecter les réarrangements d’atomes dans les matériaux amorphes. L’utilisation de la réponse harmonique s’est avérée être un indicateur fiable pour repérer les événements locaux. La réponse harmonique, également appelée force résiduelle, est calculée à partir du développement de second ordre du paysage d’énergie et du champ de déplacement entre des états inhérents voisins. Il est démontré que la réponse harmonique est fortement localisée sur les centres de relaxation. Les atomes dont les forces résiduelles disparaissent ont connu un déplacement associé à une élasticité linéaire. Le chapitre se termine par une description détaillée de la méthode de la limite d’élasticité locale. Cette méthode permet d’accéder à la réponse mécanique locale d’une configuration inhérente de manière directe et non perturbatrice, tout en contrôlant les échelles de longueur et les directions de chargement sur lesquelles elle est échantillonnée

Dans le 3ème chapitre, la limite inférieure de cette description continue est sondée. La première partie du chapitre 3 est consacrée à l’optimisation des paramètres de la méthode de la limite d’élasticité locale. Une échelle de longueur très importante est la taille à laquelle la réponse mécanique locale est sondée. Son influence sur la mesure est étudiée en discutant de la relation entre les seuils de limite d’élasticité locale et l’activité plastique due à la charge à distance. D’une part, on recherche une longueur de sondage optimale qui maximise la corrélation entre l’activité plastique et les seuils de contrainte locaux. D’autre part, il est intéressant de voir comment la taille de la zone de sondage affecte la distribution globale des barrières de contrainte locales. Dans la deuxième partie du chapitre 3, la dépendance des contraintes locales d’élasticité par rapport à la direction de la charge est examinée. Il est montré que sur une gamme de directions de chargement, la même transformation de cisaillement est activée. Dans une telle plage angulaire, la limite d’élasticité locale critique est caractérisée par

---

un puits. Il est intéressant de noter qu'un tel puits persiste si le centre de l'inclusion est légèrement déplacé. En outre, il est démontré que ces minima de contrainte dépendent fortement de la pression : une pression plus élevée s'accompagne d'une limite d'élasticité critique plus importante ; en revanche, une pression plus faible entraîne une réduction de la limite d'élasticité locale critique. Enfin, on constate qu'un minimum de contrainte, c'est-à-dire la limite d'élasticité locale critique d'une transformation par cisaillement, est décrit avec précision par un critère d'élasticité de Mohr-Coulomb.

Au cours des dernières années, de nombreux indicateurs structurels, également appelés paramètres d'ordre, ont été proposés pour saisir le changement structurel subtil qu'un liquide subit lors de son refroidissement. L'argument avancé repose généralement sur la capacité de l'indicateur spécifique à prédire la dynamique du liquide surfondu, lorsque seule la configuration initiale du matériau est connue. Pourtant, la plupart des paramètres d'ordre proposés ont un dénominateur commun : ils ne permettent aucune conclusion sur la nature du mécanisme de relaxation réel. Cela est cependant nécessaire pour mieux comprendre la relaxation structurelle elle-même. Dans le 4<sup>e</sup> chapitre, un lien étroit est établi entre les contraintes d'élasticité locales et la dynamique des liquides surfondus à la température d'équilibre. Pour évaluer cette relation sur une large gamme du régime de surfusion, des configurations initiales sont préparées à trois températures différentes. De la température la plus élevée à la plus basse, le temps de relaxation augmente de plusieurs ordres de grandeur. Trois observables cinétiques sont choisies pour saisir la dynamique des liquides surfondus : la propension dynamique, le temps de relaxation locale et le premier temps de passage. La structure de la configuration initiale est caractérisée par des seuils de contrainte locaux. Le calcul des coefficients de corrélation entre les barrières de contrainte locale et les trois observables cinétiques donne des résultats similaires : l'amplitude du coefficient de corrélation dépend fortement de la température : plus la température est basse, meilleure est la corrélation. Dans le régime de surfusion profond, les valeurs obtenues pour la corrélation entre les seuils de contrainte locale et les quantités cinétiques sont comparables aux meilleurs résultats obtenus par les techniques d'apprentissage machine et avec les autres paramètres d'ordre structurel. Cependant, la limite d'élasticité locale a un avantage sur les autres paramètres d'ordre : il est possible de tirer une conclusion sur le processus fondamental de relaxation structurelle. Ce processus élémentaire peut être considéré comme un événement de cisaillement fortement localisé le long d'un plan faible caractéristique. Ensuite, deux autres résultats sont présentés : tout d'abord, la distribution non Poissonnienne des premiers temps de passage est discutée. Ensuite, un modèle est proposé qui relie le premier temps de passage d'une inclusion à la plus petite barrière de contrainte de mesure d'un patch.

L'annexe A reproduit enfin un article paru dans *Physical Review E*, intitulé "Rejuvenation and Shear Banding in Model Amorphous Solids". M.L. a contribué à la publication en préparant les configurations initiales, en estimant la température de couplage des modes et en participant activement aux discussions lors des réunions de groupe.



# Table of contents

<b>1</b>	<b>Introduction</b>	<b>1</b>
1.1	The glass transition . . . . .	1
1.2	Phenomenology of supercooled liquids . . . . .	3
1.3	Common theories of the glass transition . . . . .	5
1.4	Temperature scales . . . . .	8
1.5	The search for an order parameter . . . . .	9
1.6	Plasticity in amorphous solids . . . . .	12
1.7	An elastic model of the glass transition: the shoving model . . . . .	12
1.8	Local yield stress method . . . . .	14
1.9	Thesis chapters in context . . . . .	15
<b>2</b>	<b>Materials and methods</b>	<b>17</b>
2.1	Binary Lennard-Jones mixture and molecular dynamic simulation . . . . .	17
2.2	Relaxation time . . . . .	20
2.2.1	Static structure factor . . . . .	20
2.2.2	Self-intermediate scattering function . . . . .	22
2.3	Characterization of the binary mixture: $T_{onset}$ and $T_{MCT}$ . . . . .	24
2.4	Inherent structures and inherent state dynamics . . . . .	30
2.5	Detection of rearrangements using the harmonic response . . . . .	31
2.6	Implementation of the local yield stress method . . . . .	33
<b>3</b>	<b>Micromechanics</b>	<b>37</b>
3.1	Preliminary remarks . . . . .	37
3.2	Length scale of the probing zone . . . . .	38
3.2.1	Optimal length scale of the probing zone . . . . .	39
3.2.2	Statistical size effects . . . . .	42
3.3	Characterization of local rearrangements . . . . .	42
3.3.1	Angular dependence of local yield stress thresholds . . . . .	44
3.3.2	Spatial resolution of local yield stress thresholds . . . . .	46
3.3.3	Pressure dependency of local yield stress thresholds . . . . .	47

## Table of contents

---

3.3.4	Yield criterion . . . . .	48
3.3.5	Problems to detect wells in the shear stress landscape . . . . .	51
3.3.6	Suggested solutions . . . . .	53
3.4	Conclusions . . . . .	54
<b>4</b>	<b>Relation between local yield stresses and the dynamics of supercooled liquids</b>	<b>55</b>
4.1	Preliminary remarks . . . . .	55
4.2	Simulation setup . . . . .	56
4.3	Correlation between local yield stresses and the dynamics of supercooled liquids . . . . .	60
4.3.1	Local yield stresses and the location of local rearrangements . . . . .	60
4.3.2	Correlation between local yield stresses and dynamic observables . . . . .	62
4.3.3	On the influence of the coarse graining procedure . . . . .	70
4.3.4	Comparison with other structural indicators or computational methods . . . . .	72
4.4	First passage time as a random variable . . . . .	74
4.5	Escape time $\tau_{esc}$ . . . . .	77
4.6	Conclusions . . . . .	79
4.7	Perspectives . . . . .	81
<b>5</b>	<b>Conclusions</b>	<b>83</b>
	<b>References</b>	<b>85</b>
	<b>Appendix A Rejuvenation and shear banding in model amorphous solids</b>	<b>93</b>

# Chapter 1

## Introduction

### 1.1 The glass transition

A liquid that is given enough time upon cooling will undergo at its melting temperature  $T_M$  a phase transition and form a crystal. Crystallization can be avoided by a sufficiently fast cooling rate [18, 33]. In this case, the liquid will enter the supercooled regime. In this regime, upon a further decrease of the temperature, the viscosity will increase several orders of magnitude over a small temperature range. Eventually, rearrangements of atoms and molecules take more time than allowed by the cooling rate; the system will consequently fall out of equilibrium and form a glass [30, 111]. Conventionally, this point defines the glass transition and its corresponding temperature  $T_g$ . However, this is not a precisely defined temperature, as  $T_g$  depends on the protocol, but the temperature of the glass transition varies only by a few degrees (3 – 5K) when the cooling rate changes by an order of magnitude [33]. To add some orders of magnitude to the drastic kinetic slowdown: around the melting temperature  $T_M$ , the relaxation time is in the order of a few picoseconds [18]. Close to  $T_g$ , the relaxation time is  $\tau_\alpha \approx 100$ s, 14 orders of magnitude larger. At the same time, the temperature has only decreased by one third  $T_g \approx 2/3 T_M$  [18, 33].

Consequently, the question arises as to what causes such a drastic dynamic slow down? In physics, diverging length and time scales are usually indicators of a phase transition. Is the glass transition a purely dynamical transition from “liquid dynamics” to “glassy dynamics” or is the drastic change in dynamical observables described above a consequence of a fundamental change from a fluid state to an ideal glassy state? In other words, is the glass transition a kinetic or a thermodynamic phase transition? Even the kind of phase transition is a subject of debate. Stillinger et al. argue in ref. [33] that the glass transition is not a real phase transition in the sense that it is not accompanied by a discontinuous change of any physical variable (e.g. volume or enthalpy). Although, there is a sudden and abrupt change in the slope of the observables, a discontinuity is detected neither in the observables nor their respective derivatives. This is schematically shown in figure 1.1. Contrary, Dyre claims that the glass transition is a second order phase transition in the Ehrenfest sense with a continuity of volume and entropy. But their respective derivatives are discontinuous [38, 45].

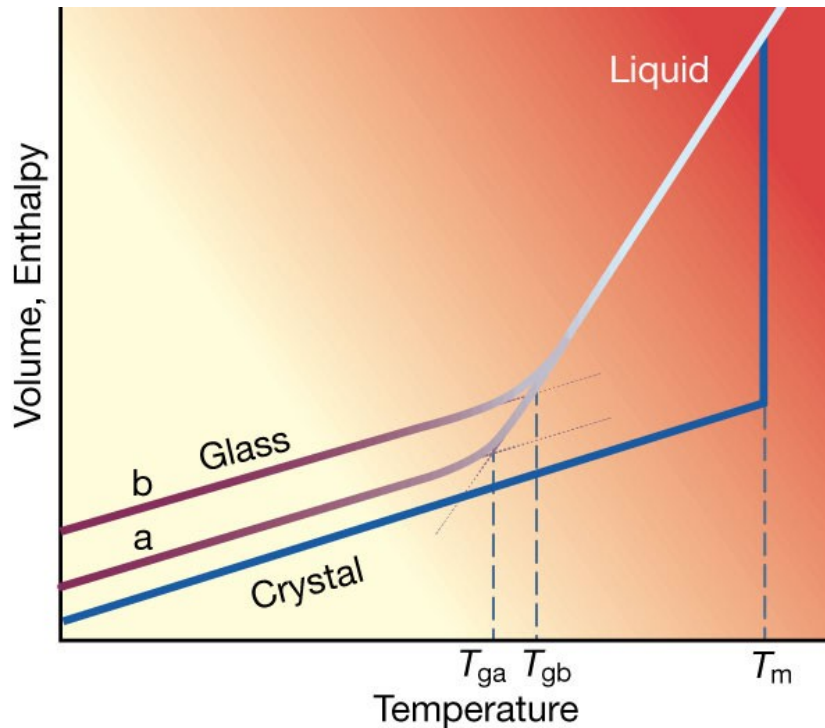


Fig. 1.1 Schematic representation of the volume  $V$  or enthalpy  $H$  as a function of temperature  $T$ . To obtain a glass, one starts with an equilibrated liquid at high temperature (top right corner). Cooling down the liquid fast enough across the melting temperature  $T_m$  to avoid crystallization (dark blue line), the system will stay equilibrated and enter the supercooled regime. Depending on the cooling rate, sooner or later the system will fall out of equilibrium and form a glass ( $T_{ga}, T_{gb}$ ). The slower the cooling, the lower the glass transition temperature. Although, there is a sudden and abrupt change in the slope of  $V(T)$  and  $H(T)$  at the glass transition temperature, Stillinger et al. argue that there is no discontinuity of any physical observable [33]. Figure taken from ref. [33].

Glasses and crystalline solids have mechanical rigidity in common [30, 40]. Yet, on a molecular level, glasses are much more comparable to liquids. Both share a disordered molecular structure and a lack of long-range order [18]. Conventional correlation functions, such as the static structure factor or the radial distribution function, fail to differentiate a liquid at high temperature from its supercooled counterpart and a glass. One might be even tempted to say, that supercooled liquids and glasses are structurally “unexciting” [30]. From a structural point of view, a glass is a liquid that stopped flowing, i.e. a frozen liquid. [22].

Not only do supercooled liquids feature a drastic dynamical slowdown and subsequently fall out of equilibrium, moreover, they also exhibit several unusual properties. Some of them will be presented and discussed in the ensuing paragraphs.

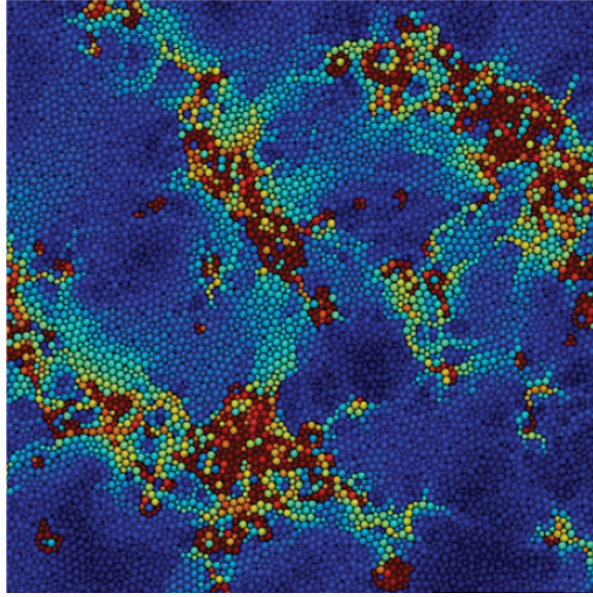


Fig. 1.2 The dynamics of glassy systems are spatially heterogeneous. Atoms colored dark red have moved more than one particle diameter, dark blue atoms did not move at all. Figure taken from ref. [61].

## 1.2 Phenomenology of supercooled liquids

### Dynamical heterogeneities and decoupling of transport constants

A signature of glassy dynamics is the appearance of dynamical heterogeneities [41]. In the supercooled regime, well below the melting temperature, the dynamics in some regions of the material can be orders of magnitudes faster than the dynamical behavior of neighboring regions [42]. Figuratively speaking, dynamical heterogeneities correspond to clusters of highly mobile particles and regions where the particles do not move at all [31]. An example of dynamic heterogeneity is shown in figure 1.2. Each particle's color corresponds to the overlap with its initial position. Dark blue atoms did not move at all, whereas dark red particles have been displaced more than one particle diameter. As one can see, highly mobile (red) particles as well as immobile particles are clustered together. Structural relaxation is therefore not uniformly distributed as it is in a normal liquid [86]. Dynamical heterogeneities become more and more pronounced as the temperature is lowered [22]. Furthermore, it is widely believed that the emergence of dynamical heterogeneities leads to the breakdown of the Stokes-Einstein relation [58]. For a liquid at high temperature  $T$ , the Stokes-Einstein relation [48] links the diffusion coefficient  $D$  and viscosity  $\mu$

$$D \frac{\mu}{T} = \text{const.} \quad (1.1)$$

In a supercooled liquid, this relation breaks down as  $1/D$  does not increase as fast as  $\mu/T$  [18]. As a result, the product  $D \frac{\mu}{T}$  increases by 2-3 orders of magnitude at the glass transition temperature  $T_g$  compared to the constant (high temperature) value [18].

### Non-exponential relaxation

The relaxation process of a liquid is characterized by an exponential decay. As the temperature is lowered, a two step relaxation emerges. This can be illustrated using a correlation function, such as the self-intermediate scattering function  $\mathcal{F}$ . In the supercooled regime, a plateau develops after a first decay, the so-called  $\beta$ -relaxation. At these intermediate times,  $\mathcal{F}$  remains constant. The length of the plateau strongly depends on the temperature. For sufficiently long times, the decorrelation process continues and  $\mathcal{F}$  decays to zero. This second decorrelation is called  $\alpha$ -relaxation. Physically, the  $\beta$ -relaxation corresponds to thermal vibrations of the atoms, whereas the  $\alpha$ -relaxation is a measure of how long it takes an atom to break out of the cage formed by the surrounding particles.

The  $\alpha$ -relaxation is not a simple exponential decay, but can more accurately be described by a Kohlrausch-Williams-Watts stretched exponential

$$\mathcal{F} \propto \exp \left[ \left( -\frac{t}{\tau} \right)^\beta \right], \quad (1.2)$$

with the characteristic decay time  $\tau$ . The parameter  $\beta$  depends on the temperature and can take values between  $0 < \beta < 1$ . It characterizes the discrepancy from strict exponential behavior [97].

The temperature, below which non-exponential relaxation starts to set in, is called the onset temperature  $T_{onset}$ . It is a reference point for any glass forming liquid [4].

According to refs. [41, 91], two images can be used to explain the non-exponential nature of the relaxation process in supercooled liquids. In the first image, the supercooled liquid is made up of a set of environments. Each environment relaxes almost exponentially but the relaxation time differs from environment to environment. Hence, the distribution of exponential relaxation processes on the microscopic level yields a non-exponential relaxation process on the macroscopic level. In the second image, each molecule of a supercooled liquid itself relaxes intrinsically in a non-exponential way. However, the existence of dynamical heterogeneities strongly supports the first image.

### Super-Arrhenius growth of transport quantities

As the temperature is lowered, a non-exponential growth of transport quantities (e.g. viscosity) is observed for some materials. Below a crossover temperature  $T_{onset}$ , the viscosity diverges faster than an exponential function (non-Arrhenius or super-Arrhenius behavior). Yet, this behavior is not universal to all glass forming liquids. For instance, for  $SiO_2$  and  $GeO_2$  the viscosity increases exponentially (Arrhenius behavior) [40]. Depending on their behavior, materials can be classified as “strong” (Arrhenius) and “fragile” (super-Arrhenius) [7]. A schematic representation of the two behaviors is shown in figure 1.3, the well known Angell plot. Empirically, it has been shown that the relaxation time of fragile liquids can be reasonably described over several orders of magnitude via the Vogel-Fulcher-Tamman (VFT) equation [44, 113, 121]

$$\tau = \tau_0 \exp \left( \frac{A}{T - T_0} \right), \quad (1.3)$$

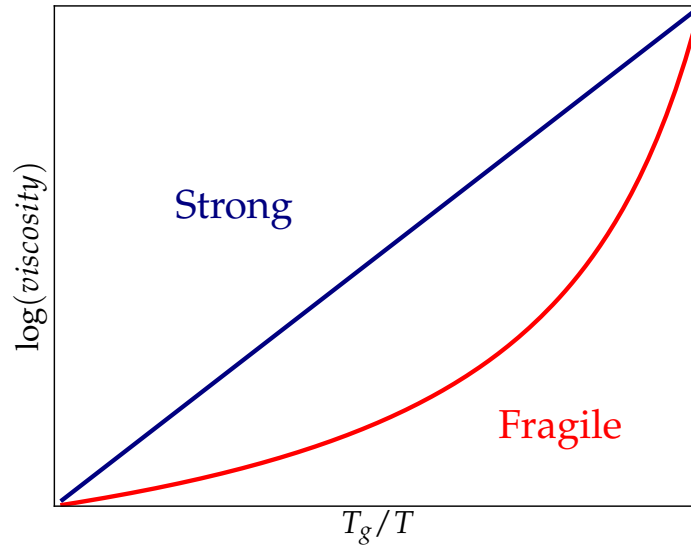


Fig. 1.3 Schematic representation of the Angell plot [7]. Supercooled liquids can be classified according to their growth of viscosity. Strong liquids show an exponential increase, whereas for fragile liquids the viscosity increases faster than an exponential function.

with the constants  $\tau_0$  and  $A$ , and  $T_0$  the temperature of the glass transition. The VFT-law predicts a phase transition into an ideal glass state at a finite temperature  $T_0$ . Aside from the equation (1.3), several alternative fits are possible for fragile glass formers, for instance, the Bässler law [15]

$$\tau \propto \exp\left(\left(\frac{T_0}{T}\right)^2\right). \quad (1.4)$$

### 1.3 Common theories of the glass transition

Generally, most theoretical approaches that try to explain the glass transition, can be divided into two categories: the first point of view concentrates exclusively on time-dependent phenomena (dynamics); for the second approach, the drastic kinetic slowdown results from an underlying thermodynamic ideal phase transition [111]. In the following, theoretical ideas most relevant to the work presented in the ensuing chapters will be shortly introduced.

#### Potential energy landscape

Efforts have been made to understand the phenomena of glassy dynamics using the concept of the potential energy landscape. A particularly popular image was outlined by Goldstein [46]. In this description, the system “lives” on a high dimensional surface, the potential energy landscape. Over

## Introduction

---

time, the system moves along the energy landscape. A minimum in the potential energy landscape is associated with a locally stable configuration. Local minima of the landscape are separated by energy barriers. Goldstein assumes that the system can overcome the energy barriers through activated jumps, as the height of the energy barriers is much larger than the thermal energy  $\Delta E \gg k_B T$ . Such a jump in phase space corresponds to a localized rearrangement, involving only a handful of particles in real space [30]. A welcome feature of Goldstein's scenario is that it allows a natural explanation of the two step relaxation process: small vibrations around minima in phase space can be linked to vibrations of atoms in real space; they are responsible for the relaxation on short timescales ( $\beta$ -relaxation) whereas the hopping from one minima to another can be related to a small number of atoms changing their neighbors (localized rearrangements). Under the assumption of activated dynamics, the hopping time increases exponentially with increasing energy barrier height. Thus, the time atoms need to break out of the cages formed by their neighbors can be associated with the  $\alpha$ -relaxation time. This theory fails at higher temperatures, where the thermal energy is comparable to the height of energy barriers  $\Delta E \sim k_B T$ . In this temperature regime, the dynamics are no longer governed by activated jumps but the system is now in the fluid regime. Nonetheless, it is possible to identify a crossover temperature  $T_X$ : below  $T_X$ , the dynamics are predominately activated, while above they are not.

Bouchaud's trap model is reminiscent of Goldstein's description: the system's dynamics are seen as the motion of a single phase point wandering through the energy landscape [34, 82]. Barriers separate the valleys (traps) from each other. They can only be overcome by activated processes. In its most simplified version, the model does not consider interactions between traps. A single master equation, written in terms of the probability  $P(E, t)$ , that the system is in a trap of depth  $E$  at time  $t$  suffices to describe the dynamics of the system.

$$\frac{\partial P(E, t)}{\partial t} = -\Gamma_0 e^{-\beta E} P(E, t) + \Gamma(t) \rho(E), \quad (1.5)$$

with  $\Gamma(t) = \Gamma_0 \int dE e^{-\beta E} P(E, t)$  the average hopping rate at time  $t$  and the attempt frequency  $\Gamma_0$ .

The beauty of the trap model is given by the fact that all the complexity of the glassy material is contained in the probability distribution of trap depths  $\rho(E)$  [18]. Various distributions can be considered for the trap depth  $E$ , e.g., a Maxwell-Boltzmann or Gaussian distribution can be used to study equilibrium dynamics of supercooled liquids [37, 50, 82]. A weakness of the trap model lies in its exemplary mean field approach: it remains a point of debate, how the notion of traps and rugged energy landscapes can be interpreted in real space [18].

## Mode coupling theory

Another theory that tries to explain glassy dynamics is the mode coupling theory. This theory was originally introduced in the 1980s [16, 73]. Without going into the mathematical details of the theory (an introduction can be found in [58] and the references therein), the mode coupling theory is an ab initio theory that makes no phenomenological assumptions and takes as input only static, time independent

properties such as the static structure factor [58]. Albeit the little input, it correctly describes the two step relaxation process [115]. Furthermore, the theory finds a good agreement regarding the shape of the relaxation function of real liquids. Lastly, the mode coupling theory predicts a power-law divergence of the relaxation time at a critical temperature  $T_{MCT}$

$$\tau_\alpha \propto (T - T_{MCT})^{-\gamma}, \quad (1.6)$$

with  $\gamma > 0$ . However, the critical temperature is much higher than the glass transition temperature  $T_{MCT} \gg T_g$  [30, 58, 115]. This divergence can be seen as a success and failure at the same time. Success, as the mode coupling theory, despite only static input, predicts a transition, but failure as this transition has never been observed in neither experiments nor numerical simulations [19]. This raises the immediate question, as to why the theory predicts such a transition. The answer is that activated dynamics are not taken into account. As the temperature is lowered and activated dynamics play an increasingly important role, the mode coupling theory fails to accurately describe the kinetic behavior in the supercooled regime. The discrepancy between theory and reality becomes worse closer to the glass transition temperature  $T_g$ . A solution is to interpret the critical temperature  $T_{MCT}$  differently, not as the temperature of the phase transition but as a crossover temperature [115]. Similar to the situation in Goldstein's picture,  $T_{MCT}$  marks the passing from non-activated to activated dynamics. One can even take the analogy one step further and identify  $T_{MCT}$  with the temperature at which Goldstein's approach fails [30]

$$T_X \approx T_{MCT}. \quad (1.7)$$

Another caveat of the approach is that due to the mean field nature of the theory, it cannot detect dynamical heterogeneities and consequently fails to predict a violation of the Stokes-Einstein relation [58, 115]. Lastly, since it is a purely dynamical theory, it cannot be used to describe thermodynamical properties of the system such as entropy. To conclude, despite its numerous shortcomings, the mode coupling theory remains an important pillar for the understanding of glassy dynamics, as all predictions of the theory have been vigorously tested against numerical simulations and experiments [18]. Moreover, in its well-known limits, the mode coupling theory delivers its results in an efficient and flexible way. Additionally, the original theory was modified, in order to address certain shortcomings, but it has to be stated that the overall universality of the theory is established [6].

#### Cooperatively rearranging regions

Adam and Gibbs [2] made the argument, that molecular rearrangements only take place cooperatively. Thus, the liquid can be divided into cooperatively rearranging regions. As the temperature is lowered, the size of these regions increases. Each of these regions has access to a finite number of configurations through rearrangements. By counting all accessible configurations, the configurational entropy  $S_{conf}$  of the system can be estimated. Assuming, that the energy barrier separating two configurations is proportional to the number of particles contained in a region, the model predicts a phase transition into

an ideal glass state at  $T_K$ . This temperature is much lower than the (dynamic) glass transition temperature  $T_g$ . The first and foremost advantage of this theoretical approach is its elegance and simplicity. It delivers a clean explanation of the stronger than Arrhenius increase of relaxation times of fragile liquids [38] and, furthermore, the VFT-law emerges naturally [30]. However, this approach does not capture all phenomena of the glassy systems: first, no clear concept of the ideal glass state has been proposed [38]. Second, it cannot describe what happens at higher temperatures - neither the crossover from non-activated to activated dynamics at  $T_{MCT}$ , nor the falling out of equilibrium at  $T_g$  [30].

In the last decades, Kirkpatrick, Thirumalai and Wolynes played an important role to merge three independent lines of research (cooperatively rearranging regions, mode coupling theory and spin glasses) into what is now known as the Random First Order Transition Theory [63, 64]. Main pillar of this theory is the evolution of the free energy landscape with temperature or density [8]. However, it is not feasible to examine the high dimensional free energy landscape of a real system, characterized by particle interactions. As a consequence, it is limited to simplified models and mean field approximations.

Over the past decades, numerous other theories on the glass transition have been proposed. Some of them are based on the theoretical concepts described above and extend them, others explore new pathways. But to describe all of them, is out of the scope of this introduction.

## 1.4 Temperature scales

In the previous paragraphs, a series of temperatures has been introduced. In the following, they are going to be revisited and put into perspective (see figure 1.4): at the melting temperature  $T_M$ , the liquid-crystal first order phase transition is located. A sufficiently fast cooling rate avoids crystallization to enter the supercooled regime. For fragile liquids, the onset temperature  $T_{onset}$  marks the beginning of non-exponential relaxation and the underlying potential energy landscape starts to influence the dynamics. At the crossover temperature  $T_{MCT}$ , the mode coupling theory falsely predicts a divergence of the relaxation time, because activated dynamics are not accounted for. Below  $T_{MCT}$ , the underlying potential energy landscape starts to heavily influence the dynamics of the supercooled liquid and activated dynamics become the principal mechanism of diffusion. Upon further cooling, the relaxation time continues to increase rapidly. Depending on the cooling protocol, the system falls out of equilibrium and forms a glass at  $T_g$ . There is one more temperature of note that has not been mentioned so far, the Kauzmann temperature  $T_K$ . Kauzmann stated, that upon cooling, the entropy of a supercooled liquid decreases at a higher rate than that of a glass or the ground state crystal [60]. Extrapolating this observation leads to  $T_K$ , where the entropy of the supercooled liquid is equal to the one of the crystal [30]. This is the famous Kauzmann paradox. Kauzmann himself points out that “certainly the entropy of the liquid can never be very much less than that of the solid” [60]. To prepare a system at  $T_K$  is out of reach for experimental and numerical studies.

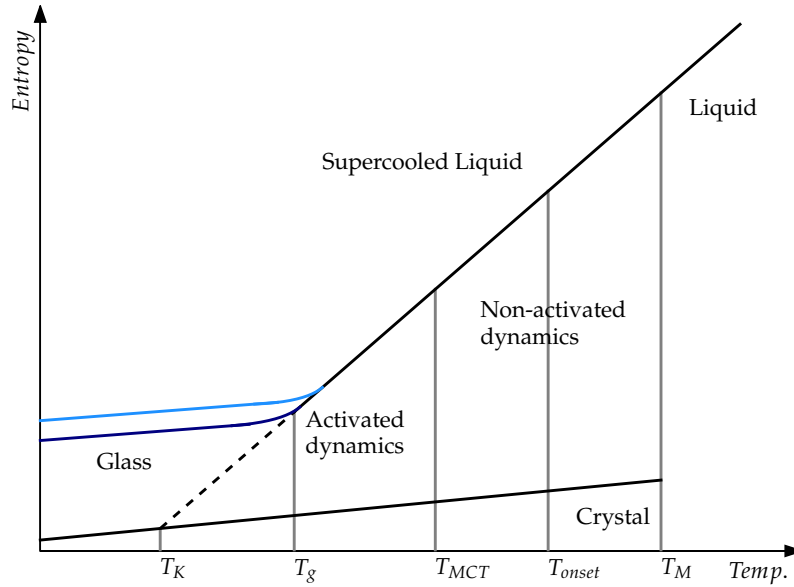


Fig. 1.4 Schematic representation of the entropy as a function of temperature. Important temperatures for supercooled liquids and glasses as indicated as well.

## 1.5 The search for an order parameter

None of the theories previously introduced can describe the glass transition with all of its rich phenomenology to its full extent. Alternatively, one can focus on the construction of an order parameter that is able to detect the subtle structural changes the system undergoes as it is cooled down. Any structural indicator has to prove itself by its potential to predict the kinetic behavior of the system. In other words, how does the order parameter correlate with the system's dynamics? In the last 10-15 years, many different structural indicators were proposed. In the following paragraphs, a selection of them will be presented and discussed.

In a series of works, Widmer-Cooper, Harrowell et al. [123–125, 127, 128] performed a thorough analysis on how different measures, local or global, correlate with the kinetic behavior observed in molecular dynamic simulations of glassy systems. To emphasize the influence of structure and minimize the effect of thermal fluctuations, they performed molecular dynamic simulations in the isoconfigurational ensemble. In this ensemble, multiple independent runs are started from the same configuration but the particles' momenta are drawn from the appropriate Maxwell-Boltzmann distribution for each run. They introduce the dynamic propensity  $\mathcal{D}_i(t)$  as the mean squared displacement of a particle  $i$ , when averaged over the isoconfigurational ensemble at a given time scale  $t$

$$\mathcal{D}_i(t) = \langle (\mathbf{r}_i(t+t_0) - \mathbf{r}_i(t_0))^2 \rangle_{iso}. \quad (1.8)$$

## Introduction

---

The system under investigation is a binary mixture composed of large and small particles. A first natural approach is to study a particle's local environment [123]. The local structure is characterized by the number of small and large neighbors respectively. Already for a binary mixture, one observes a large variety of local configurations. Still, it is possible to identify a correlation for particles with very small values of dynamic propensity. Most of these atoms are of the large type and they favor a hexagonal packing, a very stable configuration known from crystals. At the same time, no correlation is found for particles with a large dynamic propensity. On average, small particles seem to move a greater distance, but it is impossible to identify a local environment from which a high mobility emerges. Hence, the local environment described using the atom's neighbors is unsuitable to explain the observed kinetic phenomena.

Surprisingly, the local potential energy shows a poor predictability of the dynamics. Widmer-Cooper et al. report in ref. [125] the correlation between the potential energy per atom of the inherent structure of the initial configuration and the dynamical propensity, calculated after a simulated timespan of 1.5 times the structural relaxation time. The correlation between the two measures is weak, as the length scales of spatial heterogeneity for the local potential energy and the dynamic propensity are not the same. The local potential energy shows similar to the local free volume more spatial fluctuations - the corresponding typical length scale is considerably shorter than the one of the dynamic propensity.

From the results described above, the authors concluded that a purely local measure cannot display the complex dynamical behavior of glassy systems. Hence, in a further study, [127, 128] they examined how low frequency normal modes can indicate irreversible rearrangements, which are responsible for structural relaxation. Low frequency modes, also called soft modes, are calculated from the dynamical matrix of the initial inherent structure. The dynamical matrix is a second order development around a local energy minimum. The eigenmodes of the smallest eigenvalues of the dynamical matrix indicate the shallowest paths out of the local energy minimum. The eigenvectors can be used to define the participation ratio - a scalar measure that quantifies the contribution of each atom to the corresponding eigenmode. By summing over the lowest modes, one considers the shallowest possible paths the system can take to escape the local minimum. The resulting participation ratio field, a purely static quantity, not only shows an excellent spatial correlation with the location of irreversible relaxation events but the correlation also persists over a long period of time. This indicates that the underlying soft modes structure survives many rearrangements and changes in the inherent structure. Nevertheless, three observations need to be pointed out: first, the participation ratio does not allow any statement about timescales. It is not possible to say when a soft mode contributed to a relaxation event. Low frequency modes describe the curvature of a local minimum in the potential energy landscape but allow no assessment of the corresponding barrier heights. These, however, would be needed to predict timescales of rearrangements. Second, by design, the soft modes method is a perturbative approach. The dynamical matrix does not take the potential energy in its entirety into account, but rather uses a development up to second order. Lastly, this approach is computationally costly, since it involves the diagonalization of a matrix of size  $dN \times dN$ , where  $N$  is the number of particles and  $d$  the spatial dimension.

In recent years, a supervised machine learning method developed by Schoenholz et al. has produced remarkable results [32, 99–101]. This method uses several hundreds of so-called structure functions to describe the local structure of the glass. These can be divided into two families of functions, with many different sets of parameters, that are used to describe the radial density as well as the bond orientation properties of particles [32]. These functions span an  $\mathbb{R}^M$  dimensional space, with each of them corresponding to one orthogonal axis. Thus, every particle in real space can be mapped to a point in the  $M$ -dimensional space. The idea is to determine a hyperplane that separates soft particles, particles that are about to rearrange, from hard particles that do not rearrange, using a support vector machine method. To determine this hyperplane, data from molecular dynamic simulations is needed to train the system to distinguish soft from hard particles; however, the hyperplane itself is a purely structural quantity. The shortest distance between an atom and the hyperplane defines the order parameter, the so-called softness.

As aforementioned, this method is producing very impressive results, among them: first, in the supercooled regime, 90% of particles that undergo a rearrangement are classified as soft. This excellent classification allows to express a probability of rearrangement for every particle as a function of its softness. Using this probability it is furthermore possible to describe the non-exponential relaxation process in glassy systems. Lastly, one can also make statements about the structure in real space: one of the most important features seems to be the number of nearest neighbors. The more neighbors, the smaller the softness and the less likely a particle is to rearrange. This message is coherent with the cage and free volume picture, where a higher local density, on the scale of first neighbors, suppresses rearrangements. The measure of softness can be used not only to predict the dynamics at equilibrium but also to describe out of equilibrium processes, such as aging in glassy systems [100].

Another promising approach is to examine the transition paths of local relaxation events. For instance, the minimum energy path connecting the initial and final state can be determined using the nudged elastic band method [49]. By default, the transition with the smallest energy barrier has statistically the greatest weight. Alternatively, one can focus on the search of saddle points of the potential energy in order to identify activated states [92, 93]. In both cases, the idea is that an insight into the complex energy landscape will lead the way to a better understanding of the basic mechanism of structural relaxation.

All structural indicators, introduced above, that show a strong correlation between structure and dynamics, have a common denominator: they do not allow any conclusion on the fundamental process that governs structural relaxation in amorphous solids. Yet, identifying and understanding the elementary relaxation unit can be the critical point in understanding the origin of glassy dynamics and ultimately the glass transition.

Commonly, the structure of glasses is often described as a frozen liquid. But what if one reverts this picture and treats a liquid as a solid that flows? Adopting this minority point of view, allows the use of models and tools, which were previously developed for amorphous solids to examine the behavior of liquids. In this spirit, theoretical concepts that take the mechanical properties of a system into account have been proposed in the 40s and 50s of the previous century [83, 116]. More recently, Bulatov and

Argon point out that, among others, plasticity as well as structural relaxation in amorphous matter have the localized inelastic rearrangements in common [27]. In fact, they use the same 2D mesoscale model to examine both plastic flow in disordered solids and the glass transition [26–28].

Since the mechanical behavior of amorphous solids differs considerably from their crystalline counterparts, a brief summary of plasticity in disordered media is given, before an elastic model of the glass transition is discussed.

### 1.6 Plasticity in amorphous solids

Although glasses and other amorphous materials have been used by mankind for thousands of years, their mechanical behavior is still not entirely understood and remains an active field of research. In physics and material science, plasticity is the irreversible deformation of a solid due to external forces. For crystalline solids, the elementary building block of plasticity on an atomistic scale is the motion of dislocations. This mechanism is fairly well understood and part of most solid state physics textbooks [11, 54]. Due to the lack of long-range order, plastic activity cannot be governed by the same mechanism in amorphous solids. Instead, there is now a general consensus that local inelastic transformations are the fundamental mechanism of plasticity in amorphous solids [26]. Such a transformation, also known as shear transformation (ST), is the cooperative rearrangement of a handful of particles within a very short time due to external forcing (a schematic ST is depicted in figure 1.5) [52, 53, 76]. In this schema, the upper, darker colored atoms slip with respect to the lower atoms due to external forcing. The occurrence of a ST can also be visualized qualitatively using the potential energy landscape: At zero deformation, the system is in a local energy minimum. Due to the external loading, the potential energy landscape is tilted until the barrier vanishes [23, 94]. As a result, the systems rearranges, reduces the accumulated stress and finds itself in a new local energy minimum. First ideas of the ST concept date back to the late 70s [9, 10, 108] and have been continuously refined and further developed since then [43, 78–80, 114]. Although STs are a purely local phenomenon in the sense that the relative positions of the immediate neighbors do not seem to be affected [43], simulations have revealed strong spatio-temporal correlations between them [53, 78–80].

The phenomenon of STs is not unique to the atomistic length scale. Similar types of rearrangements have been observed on much larger length scales in colloidal glasses (particle size  $\sim \mu\text{m}$ ) and also in systems made out of bubbles (particle size  $\sim \text{mm}$ ) [3, 10, 59, 67, 68, 98]. This indicates that the underlying mechanism resembles a generic feature of amorphous materials [84].

### 1.7 An elastic model of the glass transition: the shoving model

In a series of papers, Dyre developed the shoving model [38–40]. A unique characteristic of this model is its dependence on the mechanical properties of the system in order to explain the drastic kinetic slowdown. Similar to plasticity in amorphous solids, flow of viscous liquids is composed of a series of flow events. Each of these events happens on short time scales and involves only a handful of particles

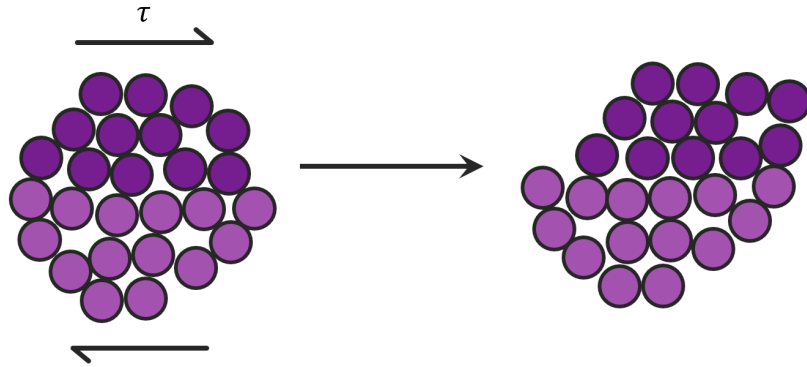


Fig. 1.5 Two dimensional schema of the elementary process of plasticity in amorphous solids: a shear transformation involves the cooperative rearrangement of few particles. Due to external forcing, the darker upper atoms move with respect to the lower atoms. Figure taken from ref. [76].

[36, 40, 110]. One can distinguish two regimes in the molecular interaction of liquids: on a short length scale, harsh repulsion dominates, whereas a much weaker attraction influences the interaction on long length scales. To rearrange, particles must come in close contact. The harsh repulsion results in high energy barriers that hinder particles from easily swapping places. Alternatively, rearranging molecules can create additional volume by shoving their neighbors aside, leading to a local decrease of density. The probability of such a density drop is given by

$$p \propto \exp\left(-\frac{W}{k_B T}\right), \quad (1.9)$$

where  $W$  is the reversible work done on the system required to create the additional volume. As the events take place on very short time scales, the mechanical response of the surrounding medium is solid like. Thus,  $W$  can be modeled through the volume increase of a sphere in an isotropic medium and calculated using standard linear elasticity theory [66]. The local volume increase leaves the density in the surrounding matrix untouched; therefore  $W$  is proportional to the temperature-dependent shear modulus  $G$

$$p \propto \exp\left(-\frac{W}{k_B T}\right) \propto \exp\left(-\frac{G(T)}{k_B T}\right). \quad (1.10)$$

As  $G$  increases upon cooling, the shoving model can explain the super-Arrhenius behavior of fragile liquids. Yet, under the reasonable assumption that  $G$  stays finite as the temperature is lowered, this model does not predict any divergence and accompanying phase transition. This model agrees very well with experimental data, as shown in figure 1.6. The viscosity of five different molecular liquids follows accurately the prediction of the model.

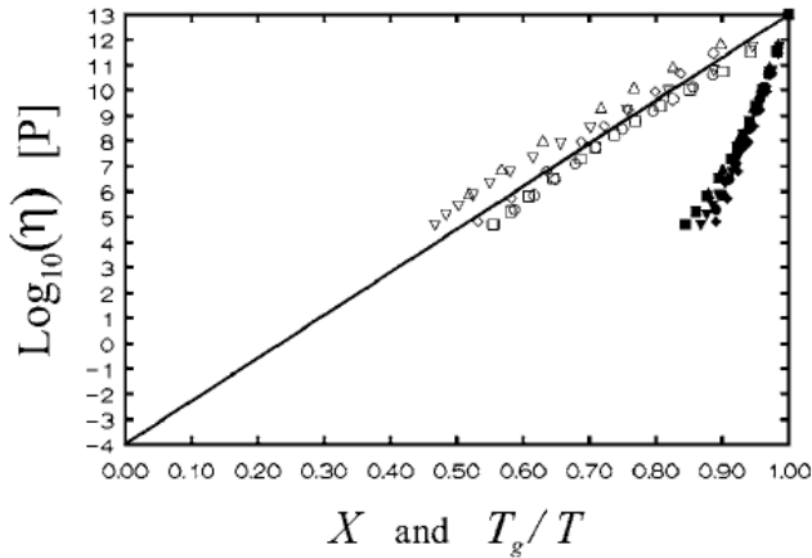


Fig. 1.6 The viscosity is shown as a function of the inverse temperature (full symbols) and as a function of  $X \propto G/T$  (open symbols) for five different molecular liquids. The full symbols demonstrate fragility. As one can clearly see, the open symbols follow the diagonal line predicted by the shoving model. Figure taken from ref. [40].

## 1.8 Local yield stress method

A common idea is that due to the amorphous nature of glasses, only a local measure can elucidate their mechanical and dynamical behavior. With this in mind, Tsamados et. al studied the spatio-temporal evolution of a local elasticity map and its relationship with dynamical heterogeneities and plastic activity [120]. A different approach, called frozen matrix, was proposed by Sollich [107]. The aim is to investigate the local mechanical properties of a system. To do so, the entire system is frozen except for a small target region. Under an imposed external strain, the frozen part of the system, which is unable to relax, will undergo an homogeneous affine deformation. From the stress response of the target region, local mechanical observables are accessible, for instance the local elastic modulus [81]. Using the frozen matrix approach, Puosi et al. were the first to identify the local yield stress along a single direction of deformation [90]. Additionally, the frozen matrix has been used to connect cavitation to weak spots in the local bulk modulus in uniaxially strained polymers [77].

The local yield stress method extends the concepts of the frozen matrix. A new feature in ref. [88] was to add a tensorial component. The local mechanical response is probed for various loading directions. This definition of local yield stresses as a function of the loading direction pays tribute to the amorphous structure of glassy systems. In disordered systems, the mechanical properties strongly depend on the loading direction. The relation between local yield stresses and the response of a system subject to global deformation has been examined [13, 14, 87, 88]. It has been shown, that there is an excellent correlation between local yield stresses and the location of plastic rearrangements forced by remote loading. Local yield stresses have a higher capability to predict the position of rearrangements

than other local structural indicators for example, the local density, local potential energy or local short range order. Local yield stresses also outperform measures of linear response (lowest shear modulus and participation fraction). Moreover, the correlation between the local yield stresses and the location of rearrangements depends on the preparation of the system. The more relaxed the system, the higher and longer persisting the correlation.

The local yield stress method has a series of advantages compared to other local indicators: first, it is a real space measurement. Consequently, all observables have a direct physical meaning and do not need an additional interpretation. A second advantage is given by its non-perturbative approach. Contrary to, for example, the calculation of soft modes, there is no higher order development of the potential energy landscape involved. Lastly, due to the local nature of the measurement, the system can be divided into parts and the calculation of local yield stresses can be parallelized to reduce the necessary computational time.

## 1.9 Thesis chapters in context

In this first chapter, a general introduction of the glass transition and its accompanying phenomena was given. Then, multiple theories and their respective shortcomings were exposed and discussed. Additionally, some order parameters that show a strong correlation between glassy dynamics (e.g. dynamical heterogeneities) and the amorphous structure were introduced.

In the following chapter 2, the 2D model system as well as the main computational methods are presented. Then, in chapter 3, the local yield stress method is applied to a small piece of glass. It is demonstrated that in the athermal quasistatic limit, there are only a finite and discrete number of shear transformations reachable through deformation. They are encoded into the amorphous atomistic structure of the material. In chapter 4, the relationship between local slip thresholds and the dynamics of supercooled liquids at equilibrium temperature is examined. In appendix A, the article “*Rejuvenation and Shear-Banding in model amorphous solids*” (c.f. also ref [14]), can be found. M.L. contributed to the publication by preparing initial configurations, estimating the mode coupling temperature and by actively participating in the discussions during group meetings.



## Chapter 2

# Materials and methods

It is difficult to validate all the consequences of the previously described theories using experimental probes only. Numerical simulation have proven to be very handy. To study and understand general phenomena, model systems are required that capture the basic physical characteristics. At the same time, the model should minimize the complexity and computational effort. Instead of simulating a specific molecular glass with characteristic bonds and charged species, a two dimensional binary mixture with a pairwise spherical symmetric interaction is used. Despite these drastic simplifications, this model system exhibits all the aforementioned phenomena of glassiness, e.g. non-exponential relaxation and dynamical heterogeneities.

In the following, the object of study and the principal numerical methods are outlined. It begins with a description and characterization of the glass forming liquid, a binary Lennard-Jones mixture, that was used throughout this thesis. Furthermore, the protocol to prepare the model systems as well as details of the molecular dynamic simulation that were used to accumulate data are given. Next, a computational advantageous tool is presented to detect local rearrangements in the trajectory. This chapter concludes with an elaborate description of the local yield stress method.

### 2.1 Binary Lennard-Jones mixture and molecular dynamic simulation

#### Interaction potential and system properties

The model system under study is a two dimensional binary mixture of large  $L$  and small  $S$  particles that interact via a slightly modified 6-12 Lennard-Jones potential in order to have a twice continuous differentiable function

$$U(r_{ij}) = \begin{cases} 4\epsilon_{ij} \left[ \left( \frac{\sigma_{ij}}{r_{ij}} \right)^{12} - \left( \frac{\sigma_{ij}}{r_{ij}} \right)^6 \right] + A & \text{for } r_{ij} < R_{in} \\ \sum_{k=0}^4 (C_k (r_{ij} - R_{in})^k) & \text{for } R_{in} < r_{ij} < R_{cut} \\ 0 & \text{for } r_{ij} > R_{cut} \end{cases} \quad (2.1)$$

## Materials and methods

Table 2.1 Interaction coefficients for the slightly modified binary Lennard-Jones potential.

	<i>LS</i>	<i>SS</i>	<i>LL</i>
$\sigma_{ij}$	1	$2 \sin(\frac{\pi}{10})$	$2 \sin(\frac{\pi}{5})$
$\epsilon_{ij}$	1	0.5	0.5

with the coefficients

$$A = C_0 - 4\epsilon_{ij} \left[ \left( \frac{\sigma_{ij}}{R_{in}} \right)^{12} - \left( \frac{\sigma_{ij}}{R_{in}} \right)^6 \right] \quad (2.2)$$

$$C_0 = -(R_{cut} - R_{in})[3C_1 + C_2(R_{cut} - R_{in})/6] \quad (2.3)$$

$$C_1 = 24\epsilon_{ij}\sigma_{ij}^6(R_{in}^6 - 2\sigma_{ij}^6)/R_{in}^{13} \quad (2.4)$$

$$C_2 = 12\epsilon_{ij}\sigma_{ij}^6(26\sigma_{ij}^6 - 7R_{in}^6)/R_{in}^{14} \quad (2.5)$$

$$C_3 = -[3C_1 + 4C_2(R_{cut} - R_{in})] / [3(R_{cut} - R_{in})^2] \quad (2.6)$$

$$C_4 = [C_1 + C_2(R_{cut} - R_{in})] / [2(R_{cut} - R_{in})^3], \quad (2.7)$$

where  $i, j \in \{L, S\}$ . The Lennard-Jones expression for interatomic distances greater than  $R_{in} = 2\sigma_{LS}$  is replaced by a smooth quartic function vanishing at a cutoff distance  $R_{cut} = 2.5\sigma_{LS}$ . The values of the interaction coefficients are listed in table 2.1. The quadratic simulation box of size  $L \times L$  ( $L = 98.8045$ ) contains - if not otherwise mentioned -  $10^4$  atoms and is equipped with periodic boundary conditions. The ratio of large to small particles is  $N_L : N_S = (1 + \sqrt{5}) : 4$ . The two types of particles are of equal mass  $m = m_L = m_S = 1$  and the density of the system is  $\rho = 1.02$ . From here onwards, all physical measurements will be expressed in terms of dimensionless units. Energies and length scales will be given in units of  $\epsilon_{LS}$  and  $\sigma_{LS}$  respectively. Subsequently, time is measured in units of  $t_0 = \sigma_{LS}\sqrt{m/\epsilon_{LS}}$ . This system is known for its good glass formability [65, 129] and has been previously used to study plasticity in amorphous solids [13, 14, 43, 87].

### Preparation protocols

All molecular dynamic simulation were performed using LAMMPS Molecular Dynamics Simulator [89]. To cover a wide range of the supercooled and glassy regime, initial configurations were prepared using the following two protocols.

**Equilibrated supercooled liquid.** The simulations are performed in the *NVT*-ensemble. The systems are equilibrated at the desired temperature for a sufficiently long period of time. The temperature is controlled using the Nose-Hoover thermostat. The duration of the equilibration is at least 100 times the relaxation time. Furthermore, it is verified that physical observables, such as the potential energy or the components of the stress tensor have stabilized.

## 2.1 Binary Lennard-Jones mixture and molecular dynamic simulation

---

**Gradual quench.** First, the systems are equilibrated at  $T = 0.93T_{MCT}$ . (The value of the critical temperature of the mode coupling theory is  $T_{MCT} = 0.378$ . For details on the method which is used to estimate  $T_{MCT}$ , see section 2.3). Next, the temperature is continuously decreased to  $T = 0.079T_{MCT}$  into the glassy state over a simulated timespan of  $10^6$ . In both stages of the preparation protocol a Nose-Hoover thermostat controls the temperature. Finally, the configurations are instantaneously quenched and relaxed using the conjugate gradient algorithm.

### Production run

**Remote loading.** In section 3.2 the connection between local yield stresses and plastic activity due to remote loading is discussed. Plastic rearrangements are activated by imposing a simple shear deformation on the initial, unstrained system, using the athermal, quasistatic shear protocol [80]. First, an affine displacement

$$\begin{pmatrix} x' \\ y' \end{pmatrix} = \begin{pmatrix} 1 & \Delta\gamma_{xy} \\ 0 & 1 \end{pmatrix} \begin{pmatrix} x \\ y \end{pmatrix} \quad (2.8)$$

is applied on every atom of the system. Next, the configuration is relaxed to mechanical equilibrium. A drop of the macroscopic shear stress indicates the occurrence of a plastic rearrangement. A small strain increment  $\Delta\gamma_{xy} = 10^{-5}$  is chosen in order to make sure that all plastic events are detected. After the occurrence of a rearrangement, a reverse loading step  $-\Delta\gamma_{xy}$  is systematically applied to ensure that the generated strains are indeed irreversible. Throughout the simulation, Lees-Edwards boundary conditions are imposed.

**Dynamics at thermal equilibrium.** In chapter 4, the relation between structure and kinetics of supercooled liquids is examined. For the dynamical aspect, molecular dynamic simulation are performed at equilibrium temperature. As for the equilibration, the production run is performed in the  $NVT$ -ensemble and a Nose-Hoover thermostat controls the temperature. Due to the fact that glassy dynamics can be very slow, a logarithmic sampling is applied. In this setup, nine snapshots of the system are saved per decade. For a linear sampling, the storage and analysis of the trajectory are not feasible.

**Isoconfigurational ensemble.** A common simulation technique to emphasize the influence of structure on the ensuing glassy dynamics, especially dynamical heterogeneities, is the isoconfigurational ensemble. It was first introduced by Widmer-Cooper et al in ref. [126] and has since been employed on a variety of systems [12, 21, 57, 62, 117]. Multiple simulation runs are started from the same initial configuration, with the initial particle velocities being drawn at random from the corresponding Maxwell-Boltzmann distribution for each run. When calculating physical quantities over the ensemble average, fluctuations due to the different initial velocities are averaged out [62]. The isoconfigurational ensemble reveals the contribution of the initial particle configuration to the subsequent dynamics.

## 2.2 Relaxation time

The strongly temperature dependent relaxation time is a measure of *how* supercooled a system is. Furthermore, this characteristic decay time allows to estimate critical, system dependent temperatures, for instance  $T_{MCT}$ , at which the mode coupling theory starts to fail.

In this section, the numerical tools, which are needed to calculate the relaxation time are presented: first, the static structure factor, and then the self-intermediate scattering function. Special attention is paid, how the latter varies with the system size.

### 2.2.1 Static structure factor

A common tool in solid state physics to describe the underlying atomistic structure of a material is the static structure factor  $S$ . Experimentally,  $S$  can be obtained from interference patterns of diffraction experiments. In a computer simulation, the exact positions of the atoms is known; consequently  $S$  can be directly calculated from any configuration. The static structure factor is defined as follows [48]

$$S(\mathbf{k}) = \frac{1}{N} \langle \hat{\rho}_{\mathbf{k}} \hat{\rho}_{-\mathbf{k}} \rangle, \quad (2.9)$$

where  $N$  is the number of particles in the system and  $\hat{\rho}_{\mathbf{k}}$  is the Fourier transform of the microscopic density

$$\hat{\rho}_{\mathbf{k}} = \int \rho(\mathbf{r}) e^{-i\mathbf{k} \cdot \mathbf{r}} d\mathbf{r} = \sum_{i=1}^N e^{-i\mathbf{k} \cdot \mathbf{r}_i}. \quad (2.10)$$

To convert the integral to a sum, the point mass nature of the system is used here. In computer simulation, the following expression is used to calculate  $S(\mathbf{k})$  [131]

$$S(\mathbf{k}) = \frac{1}{N} \left\langle \left| \sum_{i=1}^N \cos(\mathbf{k} \cdot \mathbf{r}_i) \right|^2 + \left| \sum_{i=1}^N \sin(\mathbf{k} \cdot \mathbf{r}_i) \right|^2 \right\rangle. \quad (2.11)$$

The periodic boundary conditions impose a constraint on the largest period possible and thus provide a limit for the smallest value for the wave vector [131]

$$k_{min} = \frac{2\pi}{L}, \quad (2.12)$$

with  $L$  the linear system size.

Due to the isotropic nature of liquids, the structure factor depends only on the absolute magnitude of  $\mathbf{k}$ . For this purpose,  $\mathbf{k}$ 's of similar magnitude are binned together and the averaged value for  $S(|\mathbf{k}|)$  is calculated. Unlike crystals, liquids are lacking a long-range order. Thus,  $S(|\mathbf{k}|)$  does not exhibit sharp peaks. As  $S(|\mathbf{k}|)$  is calculated from the Fourier transform of the density, it contains the averaged information of the microscopic structure of the material. The first peak of  $S(|\mathbf{k}|)$  corresponds to the average inverse length scale of the first neighbors in the system.

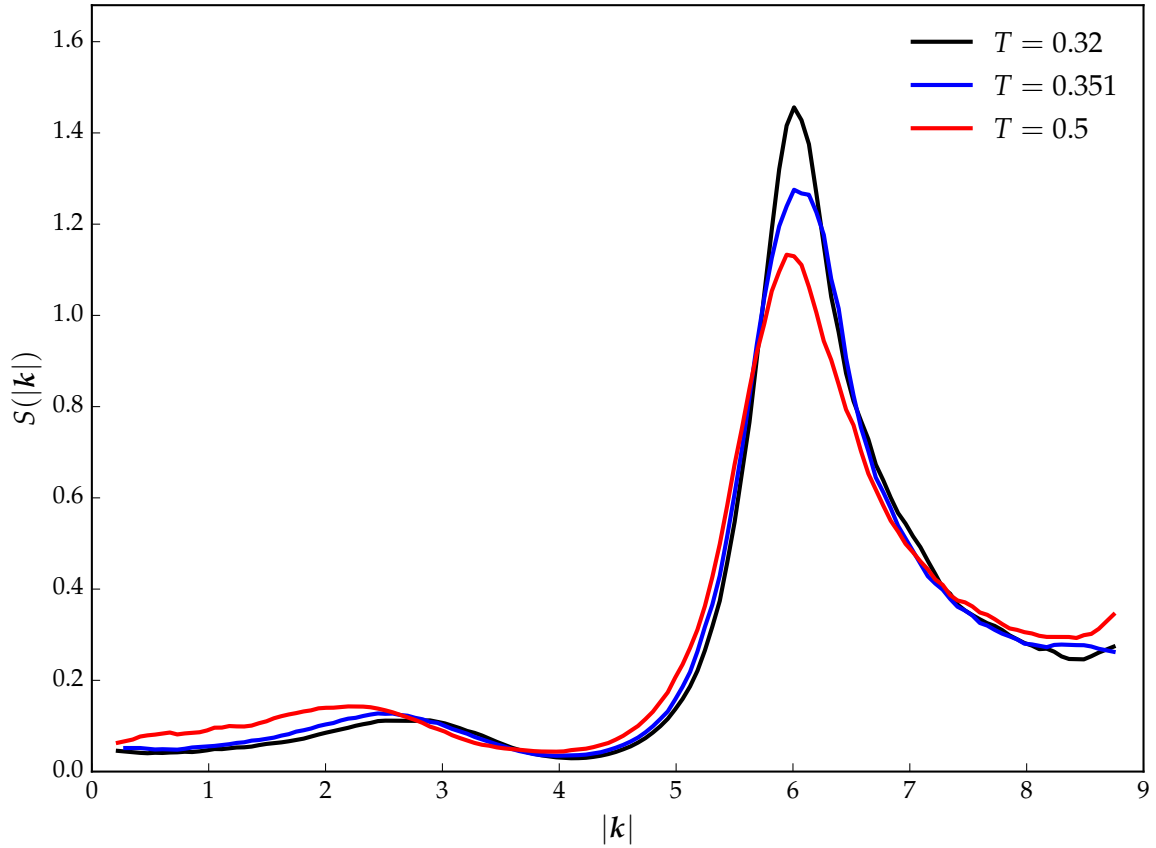


Fig. 2.1 Equation (2.11) is used to calculate  $S(|\mathbf{k}|)$ . The structural change between  $T = 0.5$  and  $T = 0.32$  is only minor and the relaxation time increases by several orders of magnitude between the two temperatures. The peak of  $S(|\mathbf{k}|)$  is at  $|\mathbf{k}_{max}| = 6.01$  for the two lower temperatures ( $T = 0.32$  and  $T = 0.351$ ) and at  $|\mathbf{k}_{max}| = 5.95$  for  $T = 0.5$ . The length  $2\pi/|\mathbf{k}_{max}|$  corresponds to the interatomic distance between nearest neighbors.

Figure 2.1 shows  $S(|\mathbf{k}|)$  for three different temperatures. Over this temperature range, the relaxation time increases several orders of magnitude (cf. section 2.2.2). Still, there are only minor differences between the three curves, which confirms that supercooled liquids structurally do not differ from their high temperature counterparts.

### 2.2.2 Self-intermediate scattering function

One way, to measure the relaxation process of supercooled liquids in experiments and computer simulations is the widely-used self-intermediate scattering function  $\mathcal{F}(\mathbf{k}, t)$  [48, 96, 102]

$$\mathcal{F}(\mathbf{k}, t) = \left\langle \frac{1}{N} \sum_{j=1}^N \exp(-i\mathbf{k} \cdot \Delta \mathbf{r}_j(t)) \right\rangle \quad (2.13)$$

$$\Delta \mathbf{r}_j(t) = \mathbf{r}_j(t_0 + t) - \mathbf{r}_j(t_0), \quad (2.14)$$

where  $N$  is the total number of particles,  $\mathbf{k}$  is the wavevector and  $\mathbf{r}_j(t)$  denotes the position of atom  $j$  at time  $t$ . To circumvent sample to sample fluctuations,  $\mathcal{F}$  is ensemble averaged, indicated by  $\langle \dots \rangle$ .

As pointed out by several publications [104–106, 130], the resulting self-intermediate scattering function as defined in equation (2.13) depends in two dimensions on the system size: persisting long-wavelength elastic vibrations will enhance the mean squared thermal displacement, leading to a faster decay of the self-intermediate scattering function at intermediate time scales. The strength of these fluctuations increases logarithmically with system size. The larger the system, the stronger the damping. The existence of long-wavelength fluctuations has also been observed experimentally in quasi 2D spherical and ellipsoidal particle suspensions [130]. Although these fluctuations are only in two dimensions present, the structural relaxation process itself is not affected. Structural relaxation does not fundamentally differ in two and three dimensions [106].

To avoid these system size dependent effects, Illing et al. propose in ref. [55] the cage relative self-intermediate scattering function

$$\mathcal{F}(\mathbf{k}, t) = \left\langle \frac{1}{N} \sum_{j=1}^N \exp\left(-i\mathbf{k} \cdot (\Delta \mathbf{r}_j(t) - \Delta \mathbf{r}_j^{cage}(t))\right) \right\rangle \quad (2.15)$$

$$\Delta \mathbf{r}_j(t) = \mathbf{r}_j(t_0 + t) - \mathbf{r}_j(t_0) \quad (2.16)$$

$$\Delta \mathbf{r}_j^{cage} = \frac{1}{N_j} \sum_{i=1}^{N_j} \mathbf{r}_i(t_0 + t) - \mathbf{r}_i(t_0). \quad (2.17)$$

As before,  $N$  is the number of particles in the system,  $\mathbf{r}_j(t)$  is the position of particle  $j$ , the wavevector  $\mathbf{k}$  and  $\langle \dots \rangle$  denotes ensemble average. However, the displacement of atom  $j$  is reduced by the center of mass motion of its neighbors. Considering the neighbor relative displacement field  $\Delta \mathbf{r}_j^{cage}$  eliminates any movement caused by a translational displacement of the simulation box. Two approaches can be used to define neighboring atoms: a Voronoi-Tessellation yields the exact number of each particle's neighbors; however, it is computationally much more advantageous to define all atoms within a cutoff distance  $R_{Shell}$  as cage forming neighbors. The system size dependence of  $\mathcal{F}(\mathbf{k}, t)$  and the effect of the cage relative displacement field are shown in figure 2.2.

Using the cage relative displacement field does not change the physical interpretation of  $\mathcal{F}(\mathbf{k}, t)$ : the self-intermediate scattering function is a measure of local density fluctuations. The length scale at which these fluctuations are probed is given by  $\mathbf{k}$ . More figuratively speaking,  $\mathcal{F}(\mathbf{k}, t)$  measures

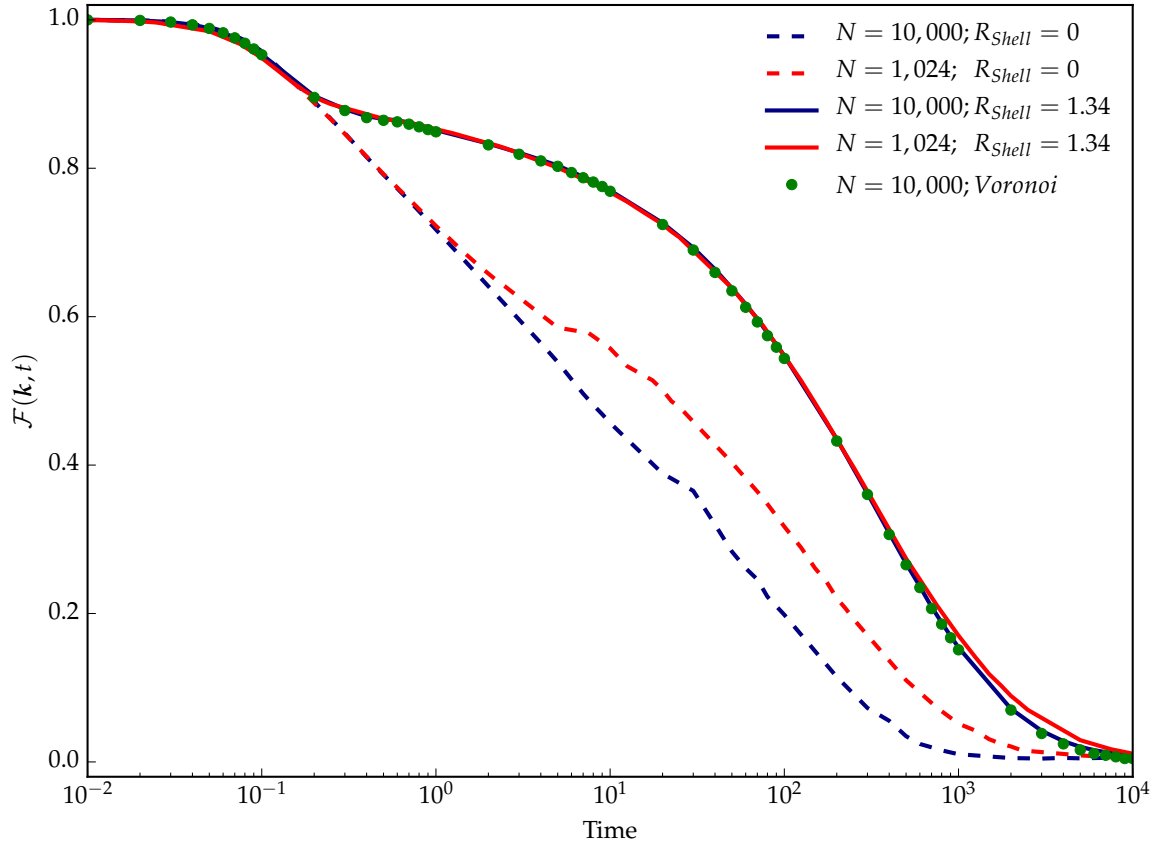


Fig. 2.2 The self-intermediate scattering function depends on the system size and is subject to damping effects if the cage relative displacement field is not used ( $R_{Shell} = 0$ ). The dotted lines decay significantly faster, as no neighbor relative movement is taken into account. For  $R_{Shell} = 1.34$ , there is an almost perfect superposition of  $\mathcal{F}(\mathbf{k}, t)$  (red and solid blue lines). Additionally, for the system containing  $N = 10,000$  atoms, the exact number of nearest neighbors was determined by Voronoi tessellation (green points), yielding the same result as  $R_{Shell} = 1.34$ , while being computationally more expensive. All curves were calculated from a supercooled liquid equilibrated at  $T = 0.351$ .

the resemblance of two molecular configurations over the inverse length scale  $\mathbf{k}$  separated by a time  $t$ . Different choices of  $\mathbf{k}$  unravel a different set of dynamics. Choosing a  $\mathbf{k}$  which corresponds approximately to one inverse particle diameter will reveal relaxation dynamics at molecular level. Reducing  $\mathbf{k}$  and thereby increasing the probing length scale leads to a longer persisting correlation, as local density fluctuations are averaged out. In the extreme case of  $\mathbf{k} \simeq 2\pi/L$ , where  $L$  is the linear system size, the correlation function will be 1 at all times, as the density is constant in the  $NVT$ -ensemble over the course of a simulation run.

As already mentioned in chapter 1, the self-intermediate scattering function has the ability to demonstrate the change of microscopic dynamics upon cooling (c.f. figure 2.3). At high temperatures,  $\mathcal{F}(\mathbf{k}, t)$  decreases exponentially; below the onset temperature  $T_{onset}$ ,  $\mathcal{F}(\mathbf{k}, t)$  shows the two-step relaxation phenomenon which is typical for glassy dynamics. The  $\beta$ -relaxation corresponds to the atoms rattling due to temperature. The  $\alpha$ -relaxation gives a time scale needed for the atoms to escape the cage formed by their neighbors. The Kohlrausch-Williams-Watts stretched exponential function describes the  $\alpha$ -relaxation

$$\mathcal{F}(\mathbf{k}, t) \propto \exp\left[\left(-\frac{t}{\tau}\right)^\beta\right], \quad (2.18)$$

with the characteristic decay time  $\tau$ . As can be seen in figure 2.4, the parameter  $\beta$  depends on the temperature and takes values between  $0 < \beta < 1$ .

The self-intermediate scattering function can be used to define the temperature dependent relaxation time  $\tau_\alpha$  of the system. With  $\mathbf{k}$  set to the value of the peak of the static structure factor, the relaxation time is defined as

$$\mathcal{F}(\mathbf{k}, t = \tau_\alpha) = \frac{1}{e}. \quad (2.19)$$

### 2.3 Characterization of the binary mixture: $T_{onset}$ and $T_{MCT}$

After properly defining the relaxation time,  $\tau_\alpha$  can be used to calculate the onset temperature  $T_{onset}$  as well as the mode coupling temperature  $T_{MCT}$ , fundamental points of reference for glass forming liquids [4]. To estimate these two temperatures for the binary mixture used in the present study, configurations containing  $N = 1,024$  atoms were prepared over a wide range of temperatures (see tab. 2.2). The self-intermediate scattering function was averaged over 250 samples per temperature.

#### Onset temperature $T_{onset}$

In the Angell plot (fig. 2.5), the relaxation time  $\tau_\alpha$  is reported as a function of the inverse temperature  $\frac{1}{T}$ . By fitting high temperature relaxation times to an Arrhenius form, the infinite temperature relaxation time  $\tau_0$  as well as the constant activation energy  $E$  can be obtained. As one can see, at lower temperatures the relaxation times  $\tau_\alpha$  are progressively higher than the high temperature extrapolation. This is the behavior of a fragile liquid in the strong-fragile classification [97]. The point, where the high temperature extrapolation breaks down, marks the beginning of non-exponential relaxation and the onset

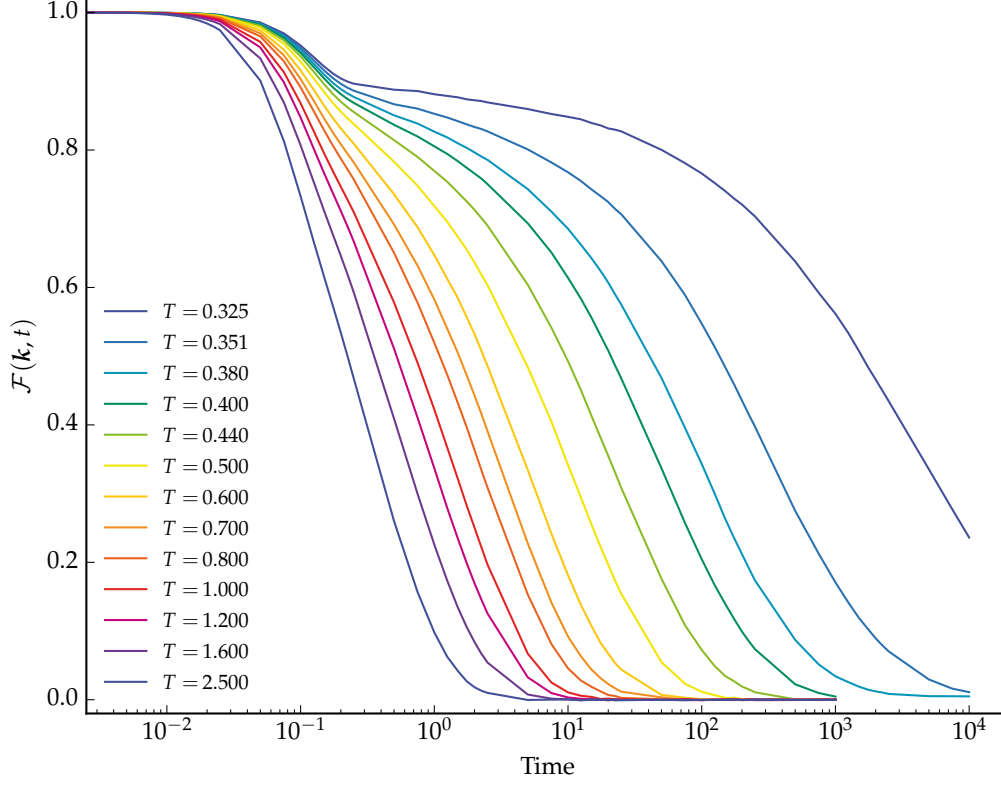


Fig. 2.3 The self-intermediate scattering function  $\mathcal{F}(\mathbf{k}, t)$  for various temperatures. At high temperatures, the decay of  $\mathcal{F}(\mathbf{k}, t)$  is exponential. At lower temperatures,  $\mathcal{F}(\mathbf{k}, t)$  shows the characteristic two step relaxation process of glassy dynamics. The size of the plateau increases as the temperature is lowered. The curves in this figure were averaged over 250 samples per temperature. Every initial configuration contains  $N = 1,024$  atoms.

Table 2.2 Initial configurations containing  $N = 1,024$  particles were prepared over a wide range of temperatures. The relaxation time was averaged over 250 samples for every temperature.

$T$	$\tau_\alpha$	$T$	$\tau_\alpha$
0.325	$4180 \pm 240$	0.500	$8.97 \pm 0.18$
0.351	$311 \pm 16$	0.600	$4.44 \pm 0.06$
0.360	$211 \pm 11$	0.700	$2.86 \pm 0.05$
0.380	$88.2 \pm 3.6$	0.800	$1.97 \pm 0.02$
0.390	$63.0 \pm 2.4$	0.900	$1.51 \pm 0.02$
0.400	$44.1 \pm 1.2$	1.000	$1.25 \pm 0.01$
0.410	$35.8 \pm 1.1$	1.200	$0.897 \pm 0.008$
0.420	$28.6 \pm 1.1$	1.600	$0.594 \pm 0.005$
0.440	$18.8 \pm 0.5$	2.000	$0.456 \pm 0.002$
0.480	$11.5 \pm 0.3$	2.500	$0.370 \pm 0.002$

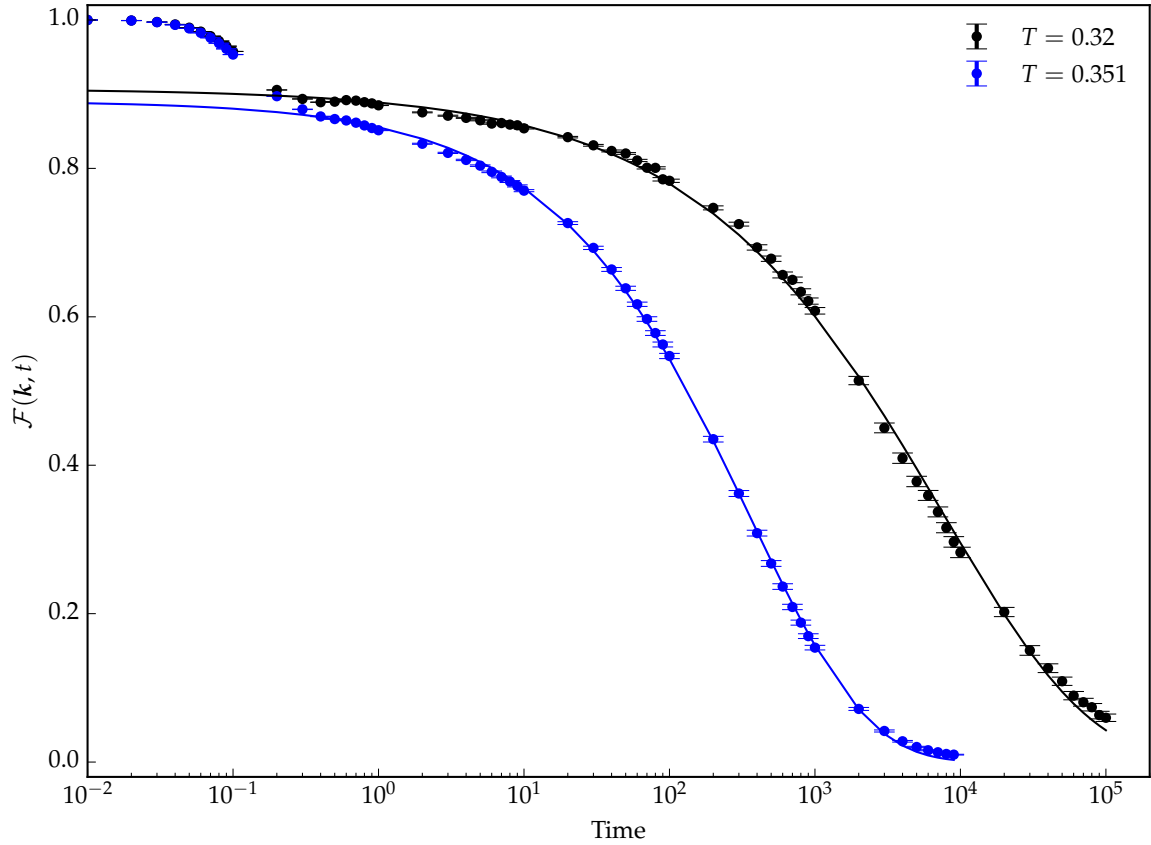


Fig. 2.4 In the deeply supercooled regime, the Kohlrausch-Williams-Watts stretched exponential (equation (2.18)) accurately describes the  $\alpha$ -relaxation. At the lower temperature ( $T = 0.32$ ), the characteristic decay time is  $\tau = 7,644 \pm 33$ . For the higher temperature ( $T = 0.351$ ), the characteristic decay time is  $\tau = 362 \pm 1$ . The parameter  $\beta$  is equal to  $\beta = 0.433 \pm 0.001$  and  $\beta = 0.547 \pm 0.001$  for the lower and higher temperature respectively.

### 2.3 Characterization of the binary mixture: $T_{onset}$ and $T_{MCT}$

Table 2.3 Measured relaxation time  $\mathcal{F}(\mathbf{k}, t = \tau_\alpha) = 1/e$  and the extrapolated relaxation time  $\tau_\alpha = \tau_0 \exp(E/T)$ . The former starts to strongly deviate from the latter at  $T = 0.48$  as non-exponential relaxation starts to set in.

	$\mathcal{F}(\mathbf{k}, t = \tau_\alpha) = 1/e$	$\tau_\alpha = \tau_0 \exp(E/T)$
$T = 0.440$	$18.8 \pm 0.5$	$15.4 \pm 0.9$
$T = 0.480$	$11.5 \pm 0.3$	$10.6 \pm 0.6$
$T = 0.500$	$8.97 \pm 0.18$	$9.0 \pm 0.5$
$T = 0.600$	$4.44 \pm 0.06$	$4.6 \pm 0.3$

of landscape influenced dynamics. The breakdown of the extrapolation is reached, when there is no longer an overlap between the measured relaxation time (using the self-intermediate scattering function) and the extrapolated relaxation time and their respective errors (c.f. table 2.3).

The inset of figure 2.5 tells a similar story. As long as the relaxation time is described by an Arrhenius form, the quantity  $T \ln(\tau/\tau_0)$  is constant. With the increasing influence of the landscape, the energy barriers sharply heighten, indicating the beginning of the landscape influenced regime. In both figures the onset temperature can be identified as

$$T_{onset} = 0.48 \pm 0.02. \quad (2.20)$$

#### Mode coupling temperature $T_{MCT}$

As second reference point, the critical temperature  $T_{MCT}$  of the mode coupling theory is estimated. As aforementioned,  $T_{MCT}$  is usually interpreted as a crossover temperature, where the kinetics change into an activated form. It is not within the scope of this thesis to examine precisely when the theory fails. Instead, the goal is to fix a temperature (range), at which activated dynamics take over the diffusive behavior. Following the protocol described in refs. [20, 30, 58, 72], the relaxation times  $\tau_\alpha$  are fitted via the power law

$$\tau_\alpha = A(T - T_{MCT})^\gamma. \quad (2.21)$$

Although the relaxation times stay finite and do not diverge as predicted by the mode coupling theory, the initial slow down is well described by equation (2.21) [72]. This is depicted in figure 2.6. From the fit for temperatures  $T \geq 0.400$ , one obtains the following values for the fit parameters:  $T_{MCT} = 0.378 \pm 0.001$ ,  $\gamma = -1.086 \pm 0.001$ , and  $A = 0.781 \pm 0.001$ .

One has to keep in mind that this procedure to estimate  $T_{MCT}$  is very sensitive to the temperatures and the corresponding relaxation times that are used for the power law fit. In particular, the resulting errors of the fit parameters listed above, do not reflect the actual uncertainties of the measurement. For instance, by leaving  $T = 0.400$  out and including all temperatures  $T \geq 0.410$ , the relaxation times  $\tau_\alpha$  are best described by the set of parameters  $T_{MCT} = 0.386 \pm 0.001$ ,  $\gamma = -1.068 \pm 0.001$  and  $A = 0.771 \pm 0.001$ . In a similar fashion, when adding an additional data point ( $T = 0.390$ ), one obtains

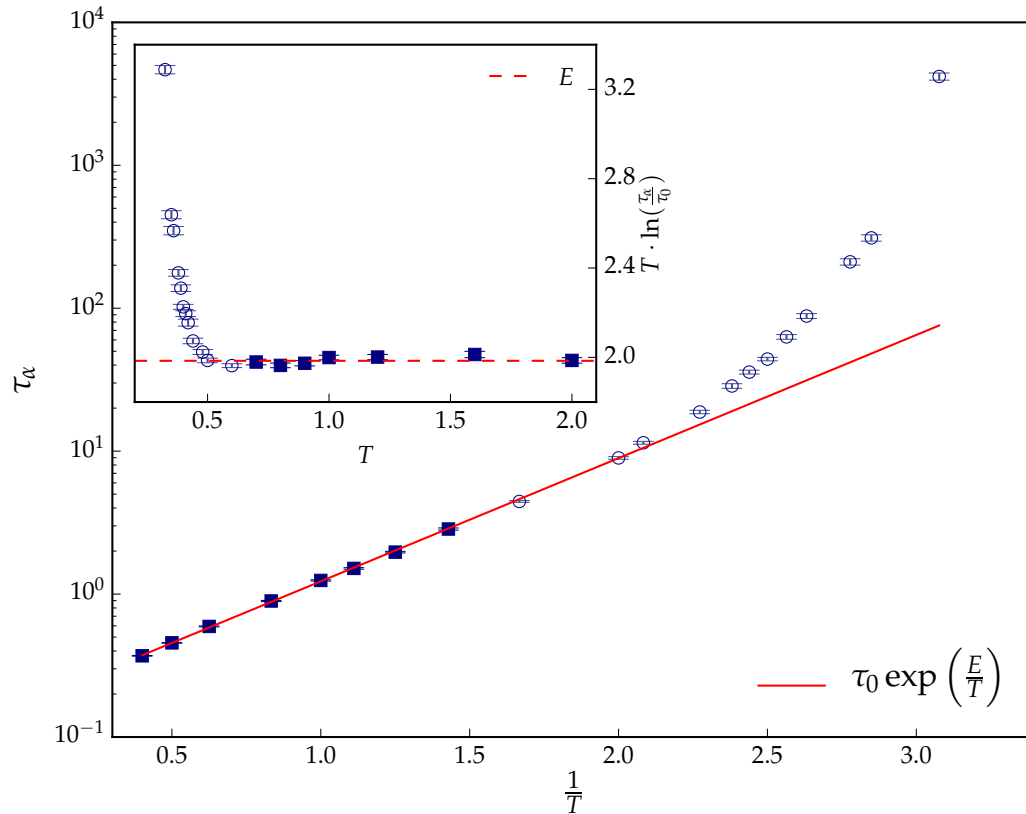


Fig. 2.5 The Angell plot shows the relaxation time  $\tau_\alpha$  as a function of the inverse temperature  $1/T$ . High temperatures ( $T \geq 0.7$ , full squares) are used to fit  $\tau_\alpha$  to an Arrhenius form  $\tau(T) = \tau_0 \exp(E/T)$ . For the infinite relaxation time  $\tau_0$  and the temperature independent activation energy  $E$ , one obtains  $\tau_0 = 0.169 \pm 0.001$  and  $E = 1.985 \pm 0.005$ . At lower temperatures, the material shows fragile behavior, as the measured  $\tau_\alpha$  are progressively higher than the fit. The beginning of the deviation from the fit marks the onset temperature  $T_{onset} = 0.48$ . Using  $\tau_0$  and the constant activation energy  $E$  from the high temperature fit,  $T \ln(\tau/\tau_0)$  is constant as long as the relaxation process shows a simple exponential decay, as shown in the inset. At the onset temperature, one observes a sharp increase, as non-exponential relaxation starts to set in.

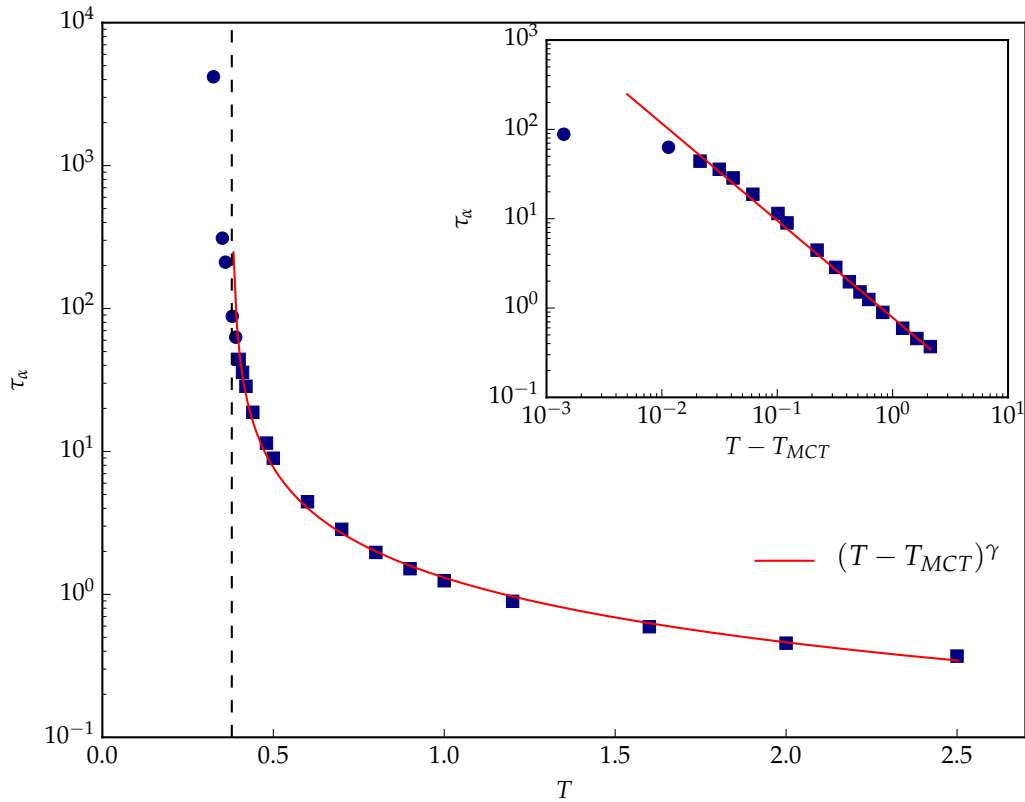


Fig. 2.6 Relaxation time  $\tau_\alpha$  as a function of temperature  $T$ . The initial kinetic slow down is well captured by the power law  $\tau_\alpha = A(T - T_{MCT})^\gamma$ . Considering only the temperatures  $T \geq 0.4$  (squares), allows an estimation for the parameters  $T_{MCT}$ ,  $\gamma$  and  $A$ . One obtains for the parameters  $T_{MCT} = 0.378$ ,  $\gamma = -1.086$ , and  $A = 0.781$ . The dashed vertical line represents the location of the estimated mode coupling temperature  $T_{MCT}$ . The inset shows the same data as the main figure but on log-log scale.

## Materials and methods

---

$T_{MCT} = 0.374 \pm 0.001$ ,  $\gamma = -1.101 \pm 0.001$  and  $A = 0.787 \pm 0.001$ . This underlines the crossover nature of the critical temperature  $T_{MCT}$ . In this temperature range, activated processes start to dominate the diffusion and thus, the mode coupling theory fails. But as aforementioned, there is no sharp transition with a diverging time scale. Still, by comparing the three sets of parameters one can estimate more realistic uncertainties for every single one

$$T_{MCT} = 0.378 \pm 0.008, \quad (2.22)$$

$$\gamma = -1.086 \pm 0.018, \quad (2.23)$$

$$A = 0.781 \pm 0.010. \quad (2.24)$$

## 2.4 Inherent structures and inherent state dynamics

Most of the systems under study are prepared in the supercooled regime, between the glass transition temperature  $T_g$  and the onset temperature  $T_{onset}$ . In this temperature range, the dynamics are influenced by the underlying potential energy landscape. Most of the time, the system vibrates around a local energy minimum and jumps only from time to time from one local minimum to another. These transition times are negligible compared to the time spent vibrating and, hence, the jumps between local minima can be regarded as instantaneous. This means that the diffusive behavior can be described through activated processes. The true, Newtonian dynamics are approximated by inherent state dynamics [102]. The inherent state dynamics are created in the following way (c.f. schema 2.7): standard molecular dynamic simulation are used to obtain a time series of configurations at a given temperature. Each configuration is attributed its corresponding inherent structure by minimizing the energy of the thermalized configuration [112]. This energy minimization is also referred to as instant quench. By minimizing all the thermalized configurations of a trajectory, one obtains another set of configurations defining the inherent state dynamics. By studying the inherent state dynamics, it is possible to follow the system from one local energy minimum to another.

One might rightly ask whether such an approximation is justified: in the deeply supercooled regime, the dynamics are heavily influenced by the underlying potential energy landscape. Hence, the approximation becomes better. At higher temperatures, close to the onset temperature  $T_{onset}$ , this description of the dynamics certainly has its weaknesses. However, below the mode coupling temperature  $T_{MCT}$ , where activated jumps become the principle diffusional process, the approximation becomes more accurate.

There is one more advantage to this description of the dynamics: inherent dynamics allow to focus on the solid-like picture of liquids. This enables to study the glassy dynamics of supercooled liquids from a mechanical point of view.

Throughout this thesis, all energy minimizations were performed using the conjugate gradient algorithm implementation of LAMMPS and are run up to machine precision.

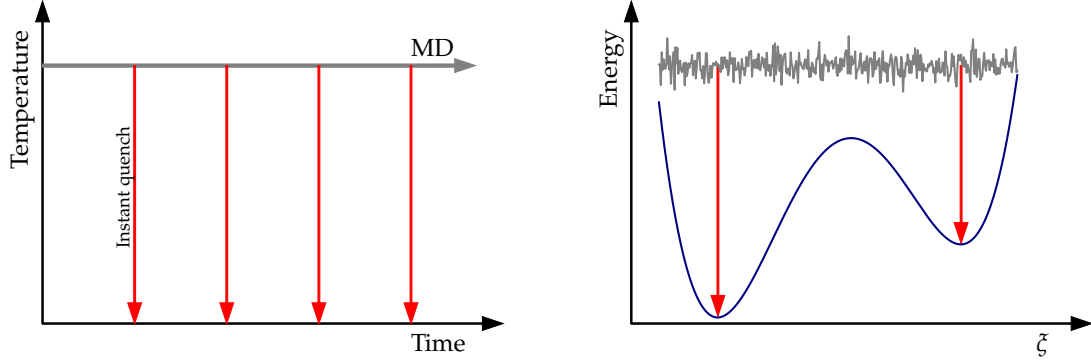


Fig. 2.7 Schema to obtain the inherent state dynamics: Standard molecular dynamic simulation are performed at a given temperature (gray arrow on the left). Periodically, snapshots are instantaneously quenched to zero temperature (red arrows) to obtain inherent states. In phase space, inherent states correspond to local minima of the potential energy landscape (blue line in the schema on the right hand side).

## 2.5 Detection of rearrangements using the harmonic response

In the literature, several methods have been proposed and discussed to detect atomistic rearrangements in amorphous materials [29, 32]. Though, the results are very similar [85]. First applied by Lemaître in a slightly different context [69], using the harmonic response of atoms has proven to be a good indicator to detect local events. In the landscape dominated regime, one studies the inherent dynamics and thus follows the system from one local energy minimum to another. The high dimensional potential energy landscape is approximated by a second order development around the minimum

$$E = E_0 + \frac{1}{2} \sum_{\langle \alpha, \beta \rangle} \sum_{\langle i, j \rangle} \mathcal{H}_{\alpha i \beta j} u_{\alpha i} u_{\beta j} + o(\|\vec{u}\|^2), \quad (2.25)$$

with the constant  $E_0$  and the displacement field  $\vec{u}$ . The first sum runs over all pairs of atoms  $\alpha, \beta$  and the indices  $i, j$  correspond to cartesian coordinate components.  $\mathcal{H}_{\alpha i \beta j}$  stands for the corresponding element of the Hessian  $\mathcal{H}$ , whereby

$$\mathcal{H}_{\alpha i \beta j} = \frac{\partial^2 E}{\partial u_{\alpha i} \partial u_{\beta j}}. \quad (2.26)$$

In analogy with a particle trapped in a harmonic potential  $V = \frac{k}{2}(x - x_0)^2$ , where the force is given by  $F = -k(x - x_0)$ , the Hessian  $\mathcal{H}$  can be mapped to the spring constant. Therefore, the component of the residual force  $F_{\alpha i}$  acting on an atom  $\alpha$  is given by

$$F_{\alpha i} = \sum_{\beta} \mathcal{H}_{\alpha i \beta i} u_{\beta i} + \mathcal{H}_{\alpha j \beta j} u_{\beta j}. \quad (2.27)$$

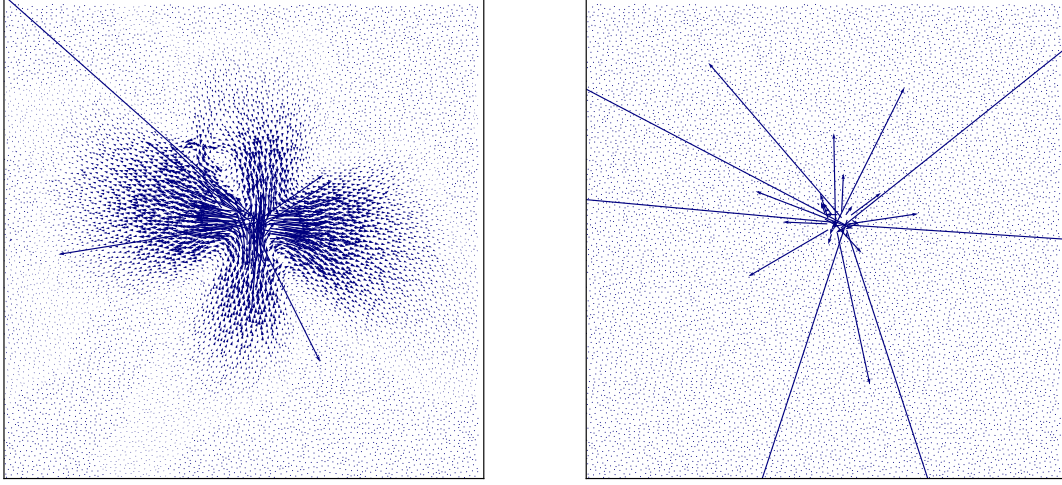


Fig. 2.8 On the left hand side, the displacement field (magnified 500 times) between two neighboring inherent states is shown. Remarkable is the long-range quadrupolar symmetry. It is a characteristic feature of Eshelby inclusions (shear rearrangements) more commonly discussed in the framework of amorphous plasticity. On the right hand side, the resulting residual forces are shown. As one can see, the harmonic response is strongly localized on the relaxation center. Atoms with vanishing residual forces have experienced a displacement associated with linear elasticity.

The image to bear in mind in this context is an atom connected to its neighbors through springs. Using this method, any atomistic displacements associated with linear elasticity are filtered. The harmonic response of these atoms is negligible. Contrary, an atom that has undergone a non-affine displacement will experience considerable residual forces  $\vec{F}$ . Thus, residual forces are strongly localized on the centers of relaxation and they vanish in the surrounding matrix [69]. An example of the harmonic response resulting from a thermally activated rearrangement is shown in figure 2.8.

The residual forces calculated via equation (2.27) are an atomistic observable. Often, it is of interest not only to identify single rearranging atoms but moreover a region in space that has rearranged. For this purpose, the residual forces (equation (2.27)) are coarse grained. The following procedure is applied: first, a regular grid of width  $R_{sampling}$  is spanned over the full system; then, on every grid node a circular inclusion (also called patch) of radius  $R_{free}$  is defined. All atoms within a patch contribute with equal weights to the coarse grained field. Finally, the average over the residual forces belonging to the same inclusion is attributed to the respective grid node

$$(\mathcal{H} \cdot \vec{u})_{cg}(p) = \frac{1}{N_p} \sum_{n \in patch} \sqrt{F_{nx}^2 + F_{ny}^2}, \quad (2.28)$$

where  $p$  indicates the grid node and  $N_p$  is the number of atoms belonging to the former. A maximum in the  $(\mathcal{H} \cdot \vec{u})_{cg}$  field reveals the location of a rearrangement. Clearly, a conscious choice has to be made for the two parameters  $R_{sampling}$  and  $R_{free}$ . In order to be in accordance with other measurements,

## 2.6 Implementation of the local yield stress method

---

especially the local yield stress calculations (c.f. section 2.6),  $R_{sampling} = 2.5$  and  $R_{free} = 5$  are used throughout this thesis.

As aforementioned, snapshots of the system are saved at logarithmically increasing points in time. Especially at higher temperatures, several rearrangements can occur between two snapshots. Generally speaking, local maxima in the  $(\mathcal{H} \cdot \vec{u})_{cg}$  field correspond to rearrangements, but a threshold still helps to distinguish a local maximum belonging to a rearrangement from noise in the data. The threshold needs to be chosen carefully. If its value is too small, one might falsely detect a rearrangement, whereas for a value too large some events will be missed. Here, the following choice is made: for each sample, the coarse grained field of residual forces is calculated between all time wise neighboring snapshots and the global maximum for each pair is identified. The result is a time series of global maxima of  $(\mathcal{H} \cdot \vec{u})_{cg}(t)$ . The threshold  $\kappa$  is chosen to be the minimum among all the maxima

$$\kappa = \min_{time}(\max_{space}(\mathcal{H} \cdot \vec{u})_{cg}(t)). \quad (2.29)$$

It is important to note that the minimum is with respect to time, while the maximum is with respect to space. One advantage of this choice is that sample to sample fluctuations are considered. With the help of the threshold  $\kappa$ , it is possible to assign one of the two states to all sites at any time during the simulation: between two inherent states separated by a time interval  $\Delta t$ , a site is either said to be “active” if  $(\mathcal{H} \cdot \vec{u})_{cg}(\Delta t) \geq \kappa$ , or “passive” if the site does not meet the threshold value.

**First passage time  $\tau_{FP}$ .** The previously introduced classification gives access to several observables. Of special interest is the first passage time  $\tau_{FP}$ . It is the point in time, when a site has reached the threshold  $\kappa$  for the first time during a simulation run. More detailed, if  $(\mathcal{H} \cdot \vec{u})_{cg}$  is calculated between two configurations at time  $t_n$  and  $t_{n+1}$  and the value of a site is larger than the threshold  $\kappa$ ,

$$\tau_{FP} = \frac{t_n + t_{n+1}}{2} \quad (2.30)$$

is attributed to that site.

## 2.6 Implementation of the local yield stress method

As aforementioned, the local yield stress method probes the mechanical response on a local scale. In this section, details of the implementation are outlined, which also have been also described in refs. [13, 88]. Furthermore, the physical observables accessible with this tool are introduced.

To begin, the inherent state of a system is prepared. Next, a circular inclusion with radius  $R_{free}$  (Region I in schema 2.9) is defined. Within the inclusion, atoms are fully relaxed. On the outside of it, particles are constrained. Next, an athermal quasistatic pure shear deformation is applied. In this formalism, two steps are alternated [80]: first, a homogeneous strain is applied to the simulation box. In a second stage, the potential energy of the particles is minimized. Due to the applied constraints in

## Materials and methods

---

Region II, atoms on the outside of the inclusion will deform in an affine manner, whereas inside the Region I atoms can also move in a non-affine way. Upon deformation, an irreversible rearrangement of atoms (also called local event) is forced to occur in Region I.

As a result of the randomness of the atomistic structure of amorphous solids, the mechanical response depends on the direction of the applied shear  $\alpha$ . A unique feature of the local yield stress method is the access to a number of physical measurements (see schema 2.10) as a function of the loading direction. During the deformation, the stress tensor  $\sigma$  (calculated using the Irving and Kirkwood formula [56]) can be measured as a function of the applied strain  $\gamma$ . The shear stress  $\tau^i$  in the undeformed state ( $\gamma = 0$ ), as well as the shear stress  $\tau^c$  at the critical strain  $\gamma_c$ , when the local event is set off is of special interest. Between these two stress states, it is possible to define the local residual plastic strength

$$\Delta\tau^c = \tau^c - \tau^i. \quad (2.31)$$

This distance to threshold describes the amount of stress needed to locally trigger the rearrangement. Furthermore, neglecting nonlinear elasticity, the local elastic modulus  $\mu$  can be estimated via

$$\mu = \frac{\Delta\tau^c}{\gamma_c}. \quad (2.32)$$

During the local event, part of the accumulated stress is dissipated into the surrounding medium. The amount of dissipated stress is given by

$$\Delta\tau^{rel} = \tau^f - \tau^c. \quad (2.33)$$

After the stress drop, the deformation is continued until the shear stress starts to increase again. This marks the final point of a local rearrangement, where the final shear stress  $\tau^f$  is calculated.

In section 3.2 the relation between local yield stresses and plastic rearrangements due to remote loading is discussed. In this discussion, the simplifying assumption is made that elasticity is homogeneous within the system. Using this approximation, the stress felt by a local region due to remote loading can be estimated. Yet, one has to be conscious, that at such length scales elasticity is heterogeneous and can lead to non-affine displacements [120]. Under the assumption of homogeneous elasticity, for a given site a rearrangement will be activated, where  $\Delta\tau^c(\alpha)$ , projected along the direction of remote loading  $\alpha_l$  is minimal. This may be mathematically expressed as

$$\Delta\tau_y = \min_{\alpha} \left( \frac{\Delta\tau^c(\alpha)}{\cos(2(\alpha - \alpha_l))} \right), \quad (2.34)$$

with  $|\alpha - \alpha_l| < 45^\circ$ .

To balance the computational cost, two more measures are taken: first, atoms at a distance greater than  $R_{free} + 2R_{cut}$  from the center of the patch are deleted. This corresponds to all particles on the outside of Region II in schema 2.9. Due to the potential cutoff at  $R_{cut} = 2.5$ , these particles do not affect the atoms in Region I. Second, local yield stresses are calculated on a regular grid of size  $R_{sampling}$ .

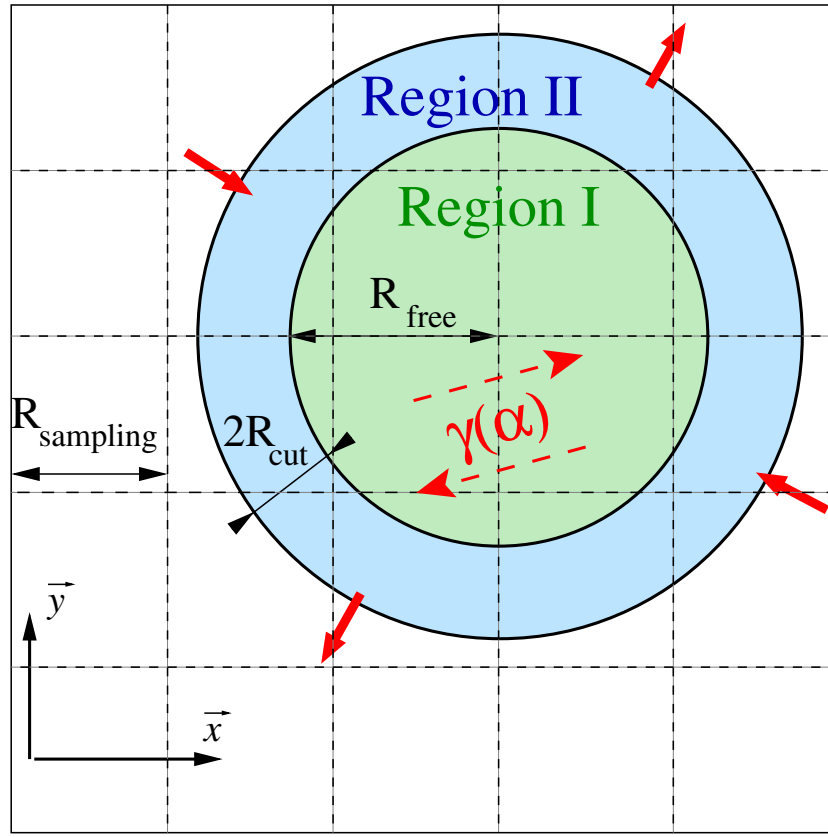


Fig. 2.9 Schematic representation of the local yield stress computation. Atoms within the Region I (radius  $R_{free}$ ) are fully relaxed, whereas atoms in Region II are constrained and deform in an homogeneous affine way due to pure shear in the loading direction  $\alpha$ . Figure adapted from ref. [13].

If not explicitly mentioned otherwise, local yield stress calculations have been performed with the following set of parameters: the size of the inclusion is set to  $R_{free} = 5$ , and  $R_{sampling} = 2.5$ . This sampling is in agreement with the harmonic response computation. For a configuration containing 10,000 atoms, this leads to a grid of size  $39 \times 39$ . The local mechanical response is probed in 18 uniformly distributed directions between  $0^\circ$  and  $170^\circ$  ( $\Delta\alpha = 10$ ). The strain increment during the loading procedure is  $\Delta\gamma = 10^{-3}$ . All minimizations are executed up to machine precision.

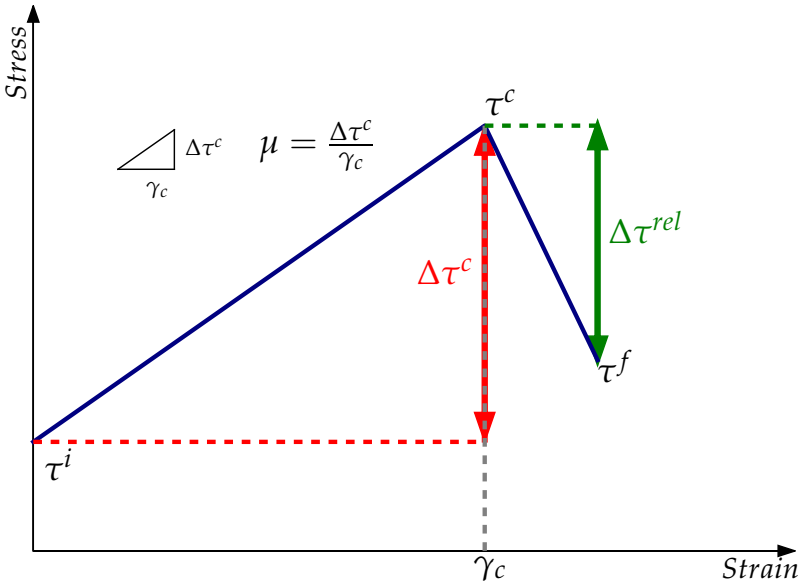


Fig. 2.10 Schematic shear stress as a function of the applied strain and the physical observables which can be measured using the local yield stress method. The nonzero prestress  $\tau^i$ , the critical yield stress  $\tau^c$  and the shear stress at the end of an event  $\tau^f$  are of special interest. With these three values, it is possible to calculate the local residual plastic strength  $\Delta\tau^c$  and the relaxation amplitude  $\Delta\tau^{rel}$ . The ratio of  $\Delta\tau^c$  and the critical strain  $\gamma_c$  gives an estimate for the local elastic modulus  $\mu$ .

## Chapter 3

# Micromechanics

### 3.1 Preliminary remarks

When applying a shear deformation to a material, the system's response passes through a series of regimes. This can be best illustrated by studying its stress response. For small strains, the stress will increase linearly. In this elastic regime, any deformation is reversible, i.e. upon unloading, the system returns to the same initial, undeformed configuration. For a larger deformation, the sample undergoes the yielding transition, resulting in an irreversible deformation of the material. The nature and precise location of the yielding transition in amorphous matter is an active field of research [84, 94, 103]. Yet, there is a consensus in the research community that amorphous plasticity on a macroscopic level results from the succession of atomistic rearrangements (shear transformations). Hence, it can be interpreted as collective effect and phenomenologically described.

In this chapter, the lower limit of the continuum description is explored. The mechanical properties of the 2D mixture are examined at length scales of approximately ten interatomic distances. The object of study are shear transformations activated through the local yield stress method and analyzed with tools more commonly used on the macroscopic scale. To prevent any possible confusion at a later point, some vocabulary used throughout this part should be defined: the main feature of the local yield stress method is to apply a pure shear deformation to an inclusion (also called small region, patch or site) until a drop of the shear stress in the loading direction occurs. This marks the appearance of a plastic event (rearrangement, shear transformation). During the loading, any deformation is reversible and the system is in the elastic regime. In the present context, a site has yielded once a rearrangement occurs. Here, it is worthwhile to mention that the inclusion is not stress free in its initial, undeformed state. It is characterized by an internal stress, inherited from the glass preparation procedure. In the following, a distinction is made between two quantities: the local residual plastic strength (or distance to threshold)  $\Delta\tau^c$  is the additional amount of stress needed to trigger a shear transformation. The critical local shear stress  $\tau^c$  corresponds to the value of the  $xy$ -component of the stress tensor along the loading direction at the onset of the instability. In analogy to the potential energy landscape,  $\Delta\tau^c$  corresponds to the barrier height, while  $\tau^c$  characterizes the stress state at the saddle point.

An important length scale of the local yield stress method is the size at which the local mechanical response of the system is probed. Hence, its influence on the measurement is discussed first.

### 3.2 Length scale of the probing zone

This aspect of the discussion has been adapted from the work published in ref. [13]. The aim of this article was to investigate the relation between local yield stress thresholds and plastic activity due to remote loading. Among others, the effect of the size of the probing zone has been examined. Two aspects need to be considered, when studying the size of the inclusion. On the one hand, the search focuses on the optimal length that maximizes the correlation between plastic activity and local residual plastic strength; i.e. to what extent the knowledge of local stress barriers, computed in the undeformed state, gives access to the sequence of first plastic rearrangements activated upon remote loading. On the other hand, it is of interest to understand how the size of the probing zone affects the distribution of the local residual plastic strength.

To investigate these two aspects, three kinds of systems are prepared: a high temperature liquid (HTL), an equilibrated supercooled liquid (ESL) and a gradual quench (GQ). The preparation of the HTL and ESL follows the equilibrated supercooled liquid protocol. In this study, the temperature of the HTL is  $T = 7.89 T_{MCT}$  and that of the ESL is  $T = 0.93 T_{MCT}$ . The GQ configurations were prepared following the gradual quench protocol, previously described in chapter 2. HTL, ESL and GQ are three highly distinct types of amorphous solids. Due to the different temperatures, at which the systems were prepared, their level of relaxation differs. Generally speaking, the lower the temperature at which the liquid falls out of equilibrium, the more relaxed the system. This is also reflected in the potential energy per atom in the final inherent states

$$E_{pot} = -2.3977 \pm 0.0019 \quad \text{for GQ,} \quad (3.1)$$

$$E_{pot} = -2.3248 \pm 0.0015 \quad \text{for ESL,} \quad (3.2)$$

$$E_{pot} = -2.1015 \pm 0.0011 \quad \text{for HTL.} \quad (3.3)$$

Plastic rearrangements are generated through remote loading. A simple shear deformation along the loading direction  $\alpha_l = 0^\circ$  is applied, following the procedure described in section 2.1. Local yield stresses are computed in the undeformed state for five different length scales  $R_{free} = 2.5, 5, 7.5, 10$  and  $15$ . At the same time, the spatial resolution of the sampling grid is kept constant at  $R_{sampling} = 2.5$ . The local mechanical response is probed for 18 angles, equally distributed between  $\alpha = 0^\circ$  and  $\alpha = 170^\circ$ . As aforementioned (c.f. section 2.6), the smallest positive stress barrier projected in the direction of remote loading  $\alpha_l$  is of special interest:

$$\Delta\tau_y = \min_{\alpha} \left( \frac{\Delta\tau^c(\alpha)}{\cos(2(\alpha - \alpha_l))} \right), \quad (3.4)$$

with  $|\alpha - \alpha_l| < 45^\circ$ . To perform a robust statistical analysis, 100 initial configurations are prepared for every quench protocol.

### 3.2.1 Optimal length scale of the probing zone

The size of the inclusion, Region I in figure 2.9, has a significant influence on the measurement of local stress thresholds. This part seek to determine an optimal length scale for  $R_{free}$ , by calculating several measures of correlation between plastic activity and local yield stress thresholds, as a function of  $R_{free}$ . However, before presenting and discussing the results of this quantitative approach, one can perform a gedankenexperiment on how the size of the inclusion affects the measurement: for small values of  $R_{free} \rightarrow 0$ , no local event is possible, as the frozen boundary conditions will over-constrain the system. In contrast, for  $R_{free} \rightarrow L/2$ , where  $L$  is the linear system size, no longer the local mechanical response will be probed but moreover the macroscopic one. The optimal length scale for the size of the inclusion will be somewhere in between: it is a compromise between a size large enough to activate a shear transformation without over-constraining the atoms, and small enough to preserve spatial heterogeneity of the sample.

The configurations prepared following the previously described protocols are subject to remote loading. The material's response is typical for amorphous solids: one observes a reversible elastic branch, interspersed by plastic events. Previously, it has been shown that these first plastic rearrangements tend to occur in regions of small  $\Delta\tau_y$  [88]. The relation between the location of the plastic events and the structure of the undeformed configuration can be quantified using the following equation

$$C_{\Delta\tau_y} = \langle 1 - 2CDF(\Delta\tau_y; \gamma_{xy}) \rangle. \quad (3.5)$$

$CDF(\Delta\tau_y)$  is the cumulative distribution function of projected stress thresholds  $\Delta\tau_y$ , computed in the as quenched state and  $\langle \dots \rangle$  denotes the ensemble average. If for a given strain  $\gamma_{xy}$ , a plastic rearrangement is detected, the corresponding site contributes to the calculation of  $\mathcal{C}_{\Delta\tau_y}$ . By design,  $\mathcal{C}_{\Delta\tau_y}$  is close to 1 if the event occurs in one of the weakest sites, where the stress threshold is small. A value of  $\mathcal{C}_{\Delta\tau_y} = 0$  indicates that there is no significant relation between the location of plastic rearrangements and  $\Delta\tau_y$ . Equation (3.5) considers neither the renewal of thresholds after an event nor the elastic noise due to previous plastic rearrangements. Figure 3.1 shows  $\mathcal{C}_{\Delta\tau_y}$  as a function of the applied strain  $\gamma_{xy}$  for the three systems under investigation. The data presented is calculated with the radius of the inclusion set to  $R_{free} = 5$ . As one can see, the amplitude of the correlation coefficient depends on the preparation protocol. The more relaxed the system, the higher the correlation. In the small strain limit ( $\gamma_{xy} \rightarrow 0$ ) a value of  $\mathcal{C} = 0.67, 0.79$  and  $0.89$  is measured for the HTL, ESL and GQ system, respectively. With an increase of the applied strain, the system loses the memory of the initial configuration. As a result, the correlation decreases. The protocol dependence of the correlation amplitude can also be alternatively quantified by looking at the location of the first ten plastic rearrangements. These local events occur in zones, belonging to the softest 23, 13 and 8.5% of sites for the HTL, ESL and GQ systems, respectively.

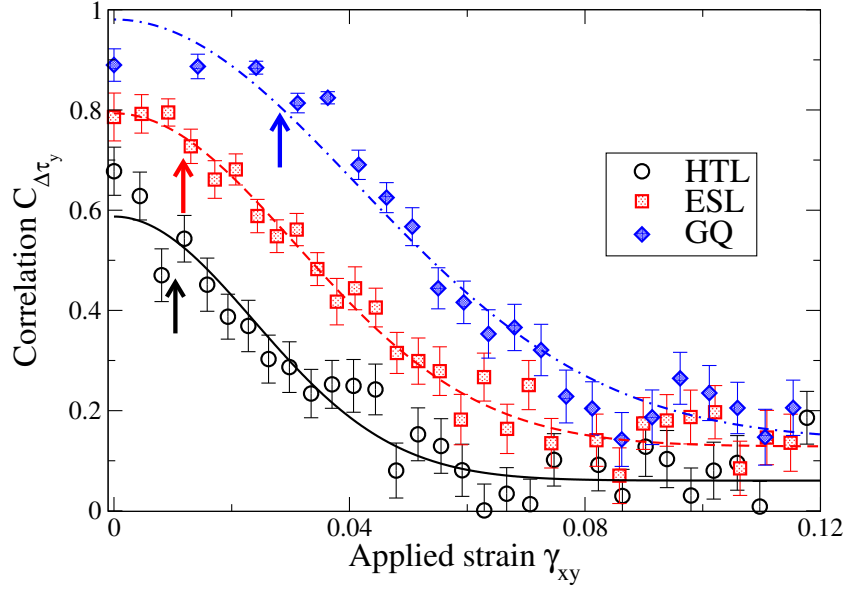


Fig. 3.1 Correlation between the location of the first plastic events and their corresponding value of  $\Delta\tau_y$  using eq. (3.5). The size of the inclusion is set to  $R_{free} = 5$ . The arrows indicate the average strain of the tenth plastic rearrangement. The solid lines result from an empirical fit  $f(\gamma_{xy}) = A + B \exp[-(\gamma_{xy}/\gamma_d)^2]$ . Using the fit, the decorrelation strain  $\gamma_d$  can be estimated.

Interestingly, one observes a drop in the correlation coefficient for GQ at approximately  $\gamma_{xy} = 0.04$ . At this amount of strain, one observes a softening of the material due to the localization of deformation.

Three correlation indicators are calculated and their dependence on the size of the inclusion  $R_{free}$  is examined, to determine the optimal size of the inclusion. The three measures are: first, the location of the first plastic rearrangement and its corresponding value of  $\Delta\tau_y$ . Second, a characteristic deformation strain  $\gamma_d$ , where the material has forgotten its undeformed configuration and third, the average correlation over a strain window. All of these measures are based on equation (3.5).

The first correlation indicator studied as a function of  $R_{free}$ , is the value of  $C_{\Delta\tau_y}$  for the first plastic event that occurs due to the remote loading  $C_{\Delta\tau_y}(\gamma \rightarrow 0^+)$ . As expected, the correlation strengthens considerably as  $R_{free}$  is increased. With the enlargement of the radius, more elastic loading heterogeneities are integrated into the patch. As a result, the loading applied to the inclusion will converge towards the remote loading procedure. Hence, with increasing  $R_{free}$ , it becomes easier to identify the weakest site that will rearrange first. Furthermore, regardless of the the system preparation, a significant decrease in the correlation  $C_{\Delta\tau_y}(\gamma \rightarrow 0^+)$  is observed for the smallest calculated inclusion size ( $R_{free} = 2.5$ ). This can be explained by the frozen boundary conditions that over constrain the patch and, thus, influence the measurement significantly. The behavior of this first correlation indicator is reported in the top part of figure 3.2.

The second correlation indicator that is estimated is the amount of strain needed, until the glass has forgotten its initial, undeformed configuration. As shown in figure 3.1, the data points obtained from

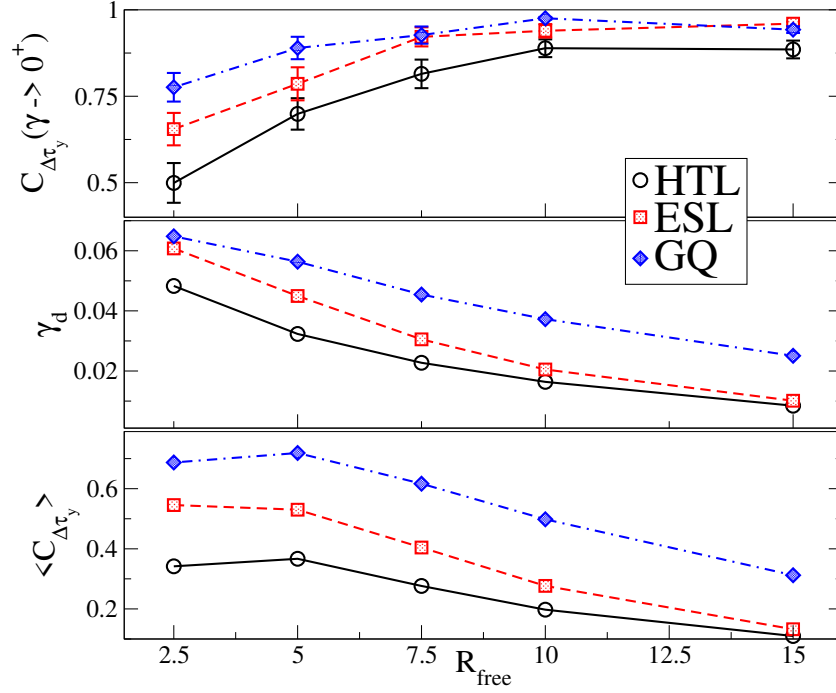


Fig. 3.2 Three correlation indicators computed as a function of the size of the probing zone  $R_{free}$ . Top: correlation between  $\Delta\tau_y$  and the location of the first plastic rearrangement. Middle: decorrelation strain. Bottom: averaged correlation over a strain window.

equation (3.5) are well described by the empirical law

$$f(\gamma_{xy}) = A + B \exp \left[ - \left( \frac{\gamma_{xy}}{\gamma_d} \right)^2 \right], \quad (3.6)$$

where  $\gamma_d$  is interpreted as a decorrelation strain. At this degree of deformation, the system has lost its memory of the as quenched state. As illustrated in the middle part of figure 3.2, the decorrelation strain decreases for larger radii. This can be explained as follows: smaller probing zones allow a higher spatial resolution and can, for instance, take into account harder zones that get advected due to the remote loading.

The third and last indicator considered is the average correlation between the location of the plastic rearrangements and the initial structure over a strain window. Mathematically speaking, equation (3.5) is integrated over a certain amount of deformation  $\gamma_*$

$$\langle C \rangle = \frac{1}{\gamma_*} \int_0^{\gamma_*} \mathcal{C} d\gamma_{xy}. \quad (3.7)$$

In the present study,  $\gamma_*$  is chosen to be the largest aforementioned decorrelation strain

$$\gamma_* = \gamma_d(R_{free} = 2.5). \quad (3.8)$$

As shown in the bottom part of figure 3.2, overall, the average correlation decreases, the larger the inclusion is. Yet, both HTL and GQ have their maximum for  $R_{free} = 5$ .

From the three correlation measures discussed above, one can conclude that a size of the inclusion with  $R_{free} = 5$  is a good compromise in terms of the correlation between the plastic activity and the projected stress threshold field  $\Delta\tau_y$ . This length scale allows a precise prediction of the first plastic events, while the overall heterogeneous structure of the amorphous material is still preserved.

### 3.2.2 Statistical size effects

As an example, maps of  $\Delta\tau_y$  for different values of  $R_{free}$ , computed for the same GQ initial configuration, are shown in the top row of figure 3.3. One observes that the amplitude of local yield stress is controlled by the weakest zone in a patch. With an increase of  $R_{free}$ , these zones enlarge their area of influence as they become more dominant. This effect leads to an overall modification of the statistics of the stress thresholds. As  $R_{free}$  is increased, the distributions are shifted considerably to smaller values of  $\Delta\tau_y$  (see. figure 3.4). One can try to reproduce the maps calculated with  $R_{free} = 7.5, 10$  and  $15$  from the one computed with  $R_{free} = 5$ , by making a simple geometrical argument: all grid nodes take the value of the smallest local minimum located inside a disk of radius  $R_{free}$ . This approach shows a remarkable agreement with the actual local yield stress maps calculated, as can be seen by comparing the top and bottom row of figure 3.3. This promising results allows to go a step further and use the same procedure to deduce the distributions of  $R_{free} = 7.5, 10$  and  $15$  from the one computed for  $R_{free} = 5$ . As reported in figure 3.4, the actual calculated distributions and those estimated show a satisfactory superposition. However, the agreement is less good for the HTL, which has been prepared at a higher temperature, and larger radii. This can be explained on the one hand by the larger elastic disorder, and on the other hand each single local minimum becomes less dominant due to the initially overall narrower distribution.

It can thus be concluded that the variation of  $\Delta\tau_y$  is dominated by statistical effects. The increase of  $R_{free}$  acts as a low-pass filter for the stress thresholds, shifting their distributions towards smaller values.

## 3.3 Characterization of local rearrangements

In the previous section, the optimal size of the probing zone was determined. Furthermore, the effect of this length scale on the ensemble of local yield stress thresholds was investigated. This section focuses on plastic rearrangements that occur when applying the local yield stress method and their comportment upon a variation of the loading conditions.

To properly characterize local events, first, the behavior of  $\tau^c$  as a function of the loading direction  $\alpha$  is studied. Next, the variation of the critical shear stress in space is examined. Lastly, the pressure dependence of  $\tau^c$  is investigated. For this purpose, a single configuration containing 10,000 atoms is prepared following the previously described GQ protocol. With this preparation protocol, a stable glass is obtained. Throughout this part, local stress calculations are performed with a set of precise parameters:

### 3.3 Characterization of local rearrangements

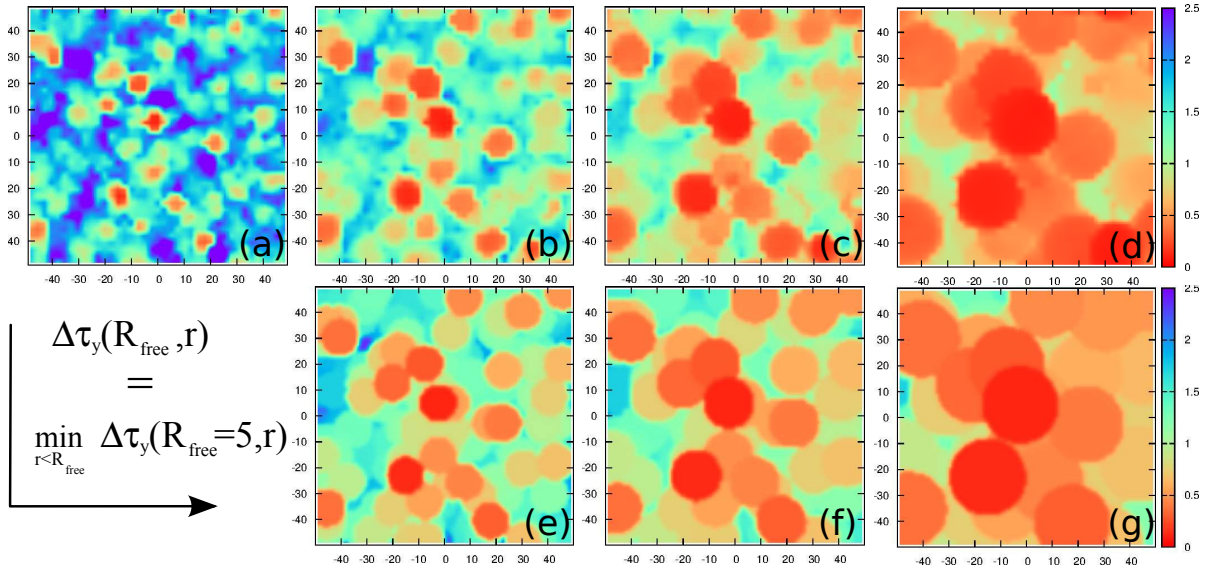


Fig. 3.3 In the top row local yield stress maps of the same GQ configuration are shown for values of  $R_{free} =$  (a) 5, (b) 7.5 (c) 10 and (d) 15. Bottom row: from panel (a) deduced local yield stress maps making a geometrical argument.

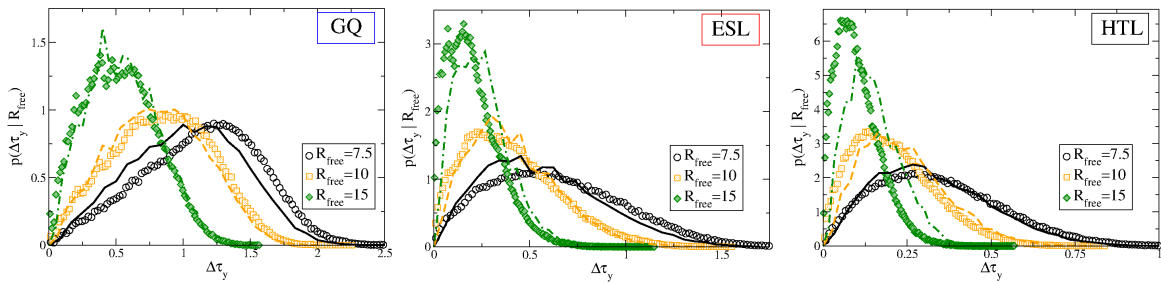


Fig. 3.4 Probability distribution function of  $\Delta\tau_y$  for the three preparation protocols and three patch sizes. The lines are obtained from the distribution calculated with  $R_{free} = 5$  as well as a geometrical argument outlined in the text and exemplified in the bottom row of figure 3.3.

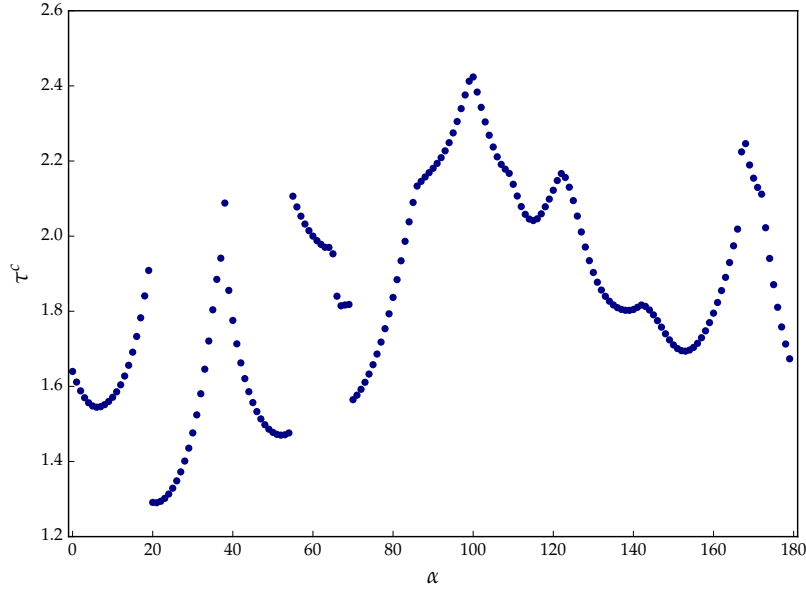


Fig. 3.5 Critical local yield stress for a particular inclusion of a GQ configuration as a function of the loading direction  $\alpha$ . Eye catching is the juxtaposition of (partial) wells. Every one of them belongs to the same local rearrangement. Due to the amorphous nature of the object of study,  $\tau^c$  does not show any elastic symmetry. Lastly, the loading protocol yields periodic boundary conditions. The well that begins on the far right hand side continues on the left hand side at  $\alpha = 0$ .

the local response is probed along 180 direction between  $\alpha = 0^\circ$  and  $\alpha = 179^\circ$  with  $\Delta\alpha = 1^\circ$ . The shear increment is set to  $\Delta\gamma = 10^{-4}$ . The size of each patch is set to  $R_{free} = 5$ .

### 3.3.1 Angular dependence of local yield stress thresholds

Figure 3.5 shows the critical yield stress  $\tau^c$  of a single inclusion as a function of the loading direction  $\alpha$ . A first noticeable feature is the juxtaposition of stress wells as a function of  $\alpha$ . The transition between two wells is either smooth or marked by a sharp discontinuity. Second, the critical yield stress  $\tau^c(\alpha)$  does not show any symmetry, as a consequence of the underlying amorphous atomistic structure. Its value depends only on the orientation of the loading direction  $\alpha$  considered. The final remark concerns the periodic boundary conditions along the loading direction. Due to the  $\pi$ -symmetry of the applied deformation, a loading along  $\alpha$  and  $\alpha + \pi$  yields the same result. Hence, in the representation of figure 3.5, the well that starts on the far right hand side continues on the left hand side at  $\alpha = 0^\circ$ .

Each well belongs to the same shear transformation. This becomes even clearer when looking at the non-affine displacement field of the instability, i.e. the loading step at which the stress drop occurs. Non-affine implicates that the applied deformation is already subtracted. From a technical stand point, one obtains this displacement field by storing the atom positions before and after the minimization step of the athermal quasistatic shear protocol. The normalized dot product  $C$  measures the similarity between two displacements fields  $\vec{u}(\alpha_1)$  and  $\vec{u}(\alpha_2)$  resulting from loading the inclusion into two directions  $\alpha_1$

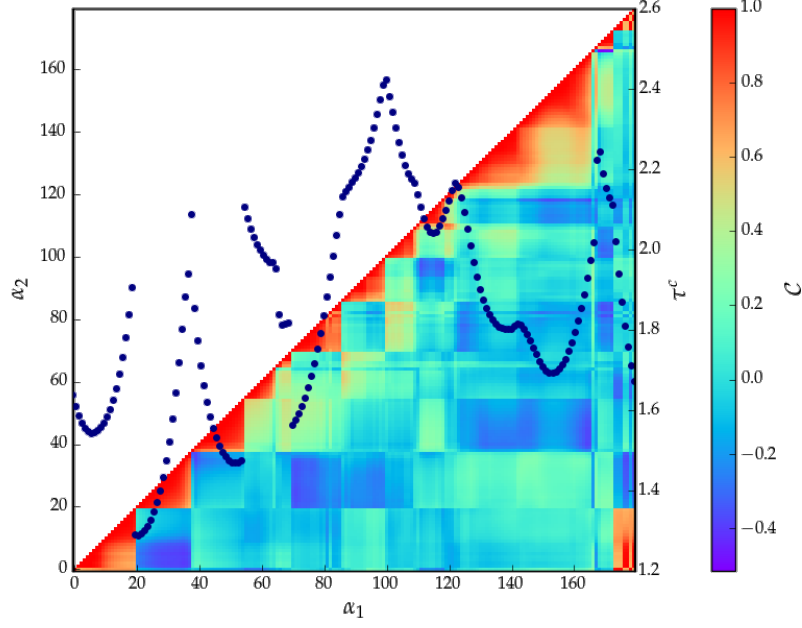


Fig. 3.6 The colormap represents the normalized dot product of the non-affine displacement field at the onset of the instability between two loading direction  $\alpha_1$  and  $\alpha_2$ . Red triangles indicate a high correlation coefficient. The system has been loaded towards the same instability. The superposed blue data points correspond to the critical local yield stress of the inclusion, also shown in fig. 3.5. The wells of  $\tau^c$  coincide with the red triangles.

and  $\alpha_2$ :

$$C(\alpha_1, \alpha_2) = \frac{1}{N} \sum_{i=1}^N \frac{\vec{u}_i(\alpha_1) \cdot \vec{u}_i(\alpha_2)}{|\vec{u}_i(\alpha_1)| |\vec{u}_i(\alpha_2)|}, \quad (3.9)$$

where  $N$  is the number of atoms in the patch. A value of  $C$  close to 1 indicates the inclusion is loaded towards the same instability for both directions  $\alpha_1$  and  $\alpha_2$ . Figure 3.6 shows  $C$  for the previously discussed inclusion. The red triangles correspond to a high correlation coefficient. As one can see, their angular range coincides with the critical shear stress wells. A discontinuity of the critical shear stress is accompanied by a sharp drop in the dot product.

As there is only a finite number of stress wells, only a limited number of shear transformations over the full loading range is accessible. Two things can be pointed out about the discrete number of rearrangements: first, this observation is a manifestation of discrete effects. The size of the inclusion under study (approximately ten interatomic distances) is clearly at the lower limit of the continuum description. Second, this juxtaposition of stress wells is very reminiscent of slip planes of dislocations in crystals, where due to the long range order, a dislocation can only slip along specific directions.

To summarize, by loading an inclusion in 180 directions, one can see that the local critical shear stress depends on the loading direction and shows no symmetry. Yet, over a range of loading angles, the patch is loaded towards the same instability. This can be verified by looking at the non-affine displacement of the instability. From this observation, one can conclude that there are only a discrete

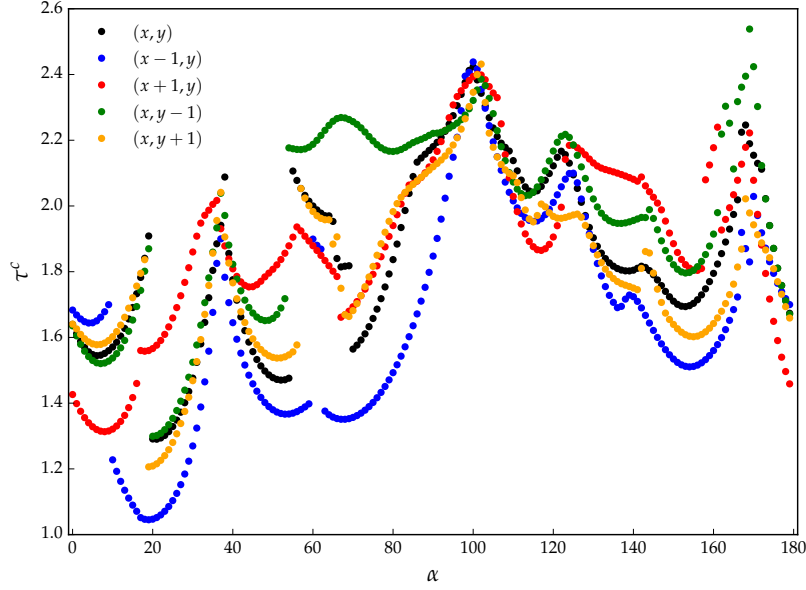


Fig. 3.7 Critical shear stress  $\tau^c$  as a function of the loading directions  $\alpha$ , for five patches, where the center has been slightly displaced ( $x \pm 1$  and  $y \pm 1$ ). The radius of a inclusion is  $R_{free} = 5$ , so there is a significant overlap between the patches.

number of rearrangements accessible. For each one of these rearrangements, the local critical shear stress shows a characteristic stress well.

### 3.3.2 Spatial resolution of local yield stress thresholds

In the previous section, the angular dependence of local stress thresholds was investigated. In this part, the aim is to examine the variation of the critical yield stress in space. The center of the inclusion is slightly displaced and then loaded again in 180 directions. For this purpose, the center point of the patch is moved  $x \pm 1$  and  $y \pm 1$  with respect to the initial position of the inclusion. As the radius of the inclusion is  $R_{free} = 5$ , there is a significant overlap between the patches. In figure 3.7, the critical shear stress is shown for the five overlapping inclusions. It becomes immediately evident, that the same wells appear multiple times, sometimes slightly shifted. This suggests that the same local event is activated multiple times.

As before, the dot product (equation (3.9)) is used to measure the similarity between the displacement fields of two patches. Only the common atoms between two inclusions contribute to  $C$ . For instance, for  $(x, y)$   $\alpha_1 = 47^\circ$  and  $(x - 1, y)$   $\alpha_2 = 49^\circ$  a correlation coefficient of  $C = 0.86$  is found. At the same time, the critical shear stress threshold is  $\Delta\tau^c(\alpha_1) = 1.51$  and  $\Delta\tau^c(\alpha_2) = 1.39$ , thus lower in the second case. Looking at the displacement fields (c.f. figure 3.8), one can see that in the second case  $(x - 1, y)$  the rearrangement is located closer to the center of the inclusion. As a result, the rigid boundary conditions surrounding the patch have less influence on the local shear transformation, resulting consequently in a lower stress barrier.

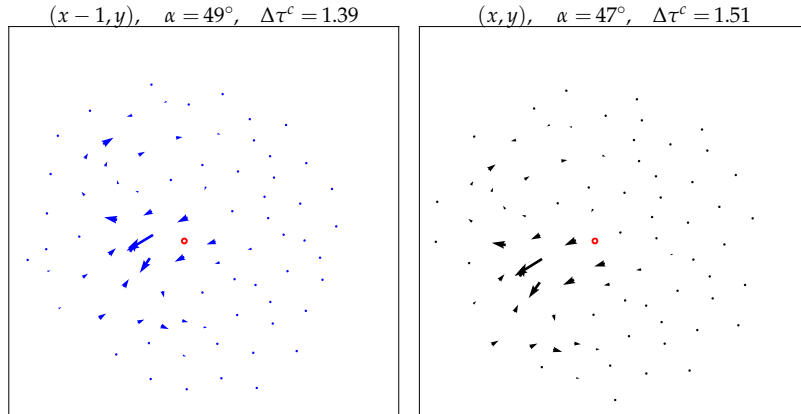


Fig. 3.8 Although the center of the inclusion is slightly displaced between the two inclusions, the same shear transformation is activated. For this example a correlation coefficient of  $C = 0.86$  is found. The measured stress barrier is lower on the left hand side. This is attributed to the fact that the rearrangement is closer the center of the patch (red dot).

From this observation it can be concluded that the same shear transformation is in fact activated multiple times for overlapping patches. Moreover, these results suggest that the glassy structure is made up of a collection of soft spots. Each one of them is characterized by a weak plane and a critical shear stress. The local yield stress method allows to scan the glassy structure and reveals the presence of these soft spots. Consequently, the question arises, if the density of these shear transformations can be estimated.

#### 3.3.3 Pressure dependency of local yield stress thresholds

Dislocations in a crystal interact only weakly with a pressure field [103]. In contrast, experimental studies have revealed that the yield stress of metallic glasses differs under tensile loading and compression [75, 76]. Hence, the question arises how the local critical shear stress depends on the pressure.

The surface of the simulation box can be rescaled in two dimensions to induce a pressure variation. This makes it possible to study the pressure dependency of the shear events. In the following, a label of  $+\delta\%$  implies that the surface has been increased by  $\delta\%$ . Likewise,  $-\delta\%$  indicates a surface reduction by  $\delta\%$  with respect to the undeformed simulation box.

Figure 3.9 shows the critical shear stress of the same patch as previously but for three different deformations  $\delta\%$ . As expected, a tighter packing ( $\delta < 0$ ) is accompanied by larger values of  $\tau^c$ . At the same time, a pressure reduction ( $\delta > 0$ ) leads to lower critical stress values. Additionally, with the looser packing, the stress landscape becomes smoother: the local minima are less pronounced and the amplitude of the jumps at a discontinuity is smaller compared to the undeformed simulation box. Yet, it is possible to identify the same well for different pressure values. Hence, the same rearrangement is activated for different pressures. However, the angular range over which the same event is triggered,

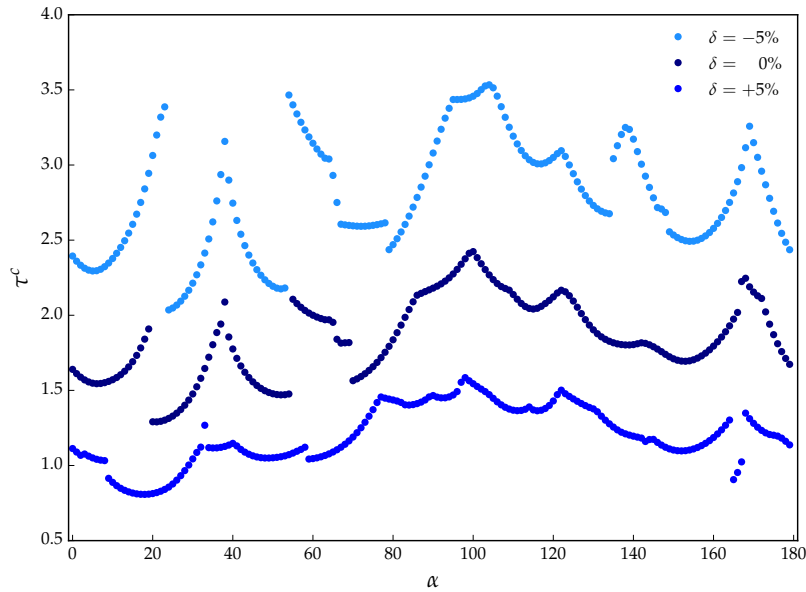


Fig. 3.9 The critical shear stress  $\tau^c$  shows a high pressure sensitivity. An increase of the surface of the simulation box  $\delta = +5\%$  lowers the yield stress considerably. On the contrary, a tighter packing increases the critical shear stress (here as an example  $\delta = -5\%$ ). A change of pressure can make new rearrangements accessible as wells appear and disappear as a function of  $\delta$ .

is not fixed. The angular range of a weak plane can either increase or decrease as well as drift slightly as the pressure changes. Furthermore, it is possible that between two existing wells a new (partial) well appears as the pressure is increased or decreased. In other words, a new rearrangement becomes accessible as pressure is applied or released on the system. Overall, the response of  $\tau^c$  to a change of the simulation box indicates a coupling between the critical shear stress and hydrostatic pressure  $p$ .

### 3.3.4 Yield criterion

In the previous parts, it was shown that only a limited number of shear transformations is accessible. Hereinafter, the comportment of the critical shear stress  $\tau^c$  for a single rearrangement will be elucidated and explained using a yield criterion. More commonly, yield criteria are applied on macroscopic length scales, where the mechanical properties of the material are well described by continuum mechanics.

In the continuum description of solids, the stress tensor can be used to define a space, where the principal components are the orthogonal axes. Any stress state of the system can be mapped to a point in this space. Through deformation, the system can explore the stress space [71]. Within this space lays a surface, called yield surface, that separates the elastic from the plastic regime. Below the surface, any deformation is reversible, while the system is irreversibly deformed as soon as it touches the yield surface. An equation describing the yield surface is called yield criterion. In crystalline materials, the fundamental process of deformation is the motion of dislocations. This mechanism shows a weak pressure dependence. Hence, the yield surface of crystals is characterized by a criterion that neglects any

### 3.3 Characterization of local rearrangements

pressure dependence and focuses on the maximum shear stress. Examples of such criteria are the von Mises or Tresca yield criteria [75]. However, the situation is different for amorphous materials; e.g. in metallic glasses, the pressure has an important influence on plastic deformation [76]. As also previously discussed in figure 3.9, the critical shear stress  $\tau^c$  shows a strong pressure dependence. Additionally, the existence of stress wells excludes a homogeneous von Mises yield criterion, as it is intrinsically isotropic. In that case, the critical yield stress would not depend on the loading direction  $\alpha$ . Therefore, a yield criterion that incorporates the pressure dependency as well as the anisotropy is needed. In the present study, the Mohr-Coulomb yield criterion

$$\tau^c = \tau_0 - \varphi p, \quad (3.10)$$

is applied.  $\tau^c$  is the critical shear stress at which failure occurs and  $\tau_0$  and  $\varphi$  are two parameters. The latter controls the influence of the pressure  $p = -\frac{\sigma_{xx} + \sigma_{yy}}{2}$ . Previously, the Mohr-Coulomb yield criterion has proven to accurately describe the yield surface of a metallic glass subject to a variety of biaxial stress states [76]. Especially, the Mohr-Coulomb criterion accounts for the asymmetry between the magnitude of the yield stress in tension and compression. However, there are also other yield criteria available. For example, in ref. [95] a pressure modified von Mises criterion is used to characterize an amorphous polymer glass under various deformations.

Equation (3.10), with its parameters  $\tau_0$  and  $\varphi$ , describes the critical shear stress for one loading direction. As previously discussed and shown, the same local event is activated for multiple loading angles  $\alpha$ . A single set of parameters  $\tau_0$  and  $\varphi$  should detail the same shear transformation. To describe a rearrangement with the same parameters, the stress tensors, measured for various angles  $\alpha$ , must be projected onto a common direction  $\theta$ . The angle  $\theta$  is the characteristic weak plane of the shear transformation. For the shear component of the stress tensor, this projection is given by

$$\tau^c(\theta) = \frac{\sigma_{yy}^c(\alpha) - \sigma_{xx}^c(\alpha)}{2} \sin(2(\theta - \alpha)) + \tau^c(\alpha) \cos(2(\theta - \alpha)) \quad (3.11)$$

By combining equation (3.10) and (3.11) one obtains for the yield criterion

$$\tau^c(\alpha) = \frac{\tau_0 - \varphi p}{\cos(2(\theta - \alpha))} - \frac{\sigma_{yy}^c(\alpha) - \sigma_{xx}^c(\alpha)}{2} \tan(2(\theta - \alpha)). \quad (3.12)$$

Before applying equation (3.12) on the simulation data, a couple of remarks must be listed: the  $1/\cos(2(\theta - \alpha))$  dependency in first term on the right hand side can be understood as the penalty of shearing in an suboptimal direction. More figuratively speaking, the inclusion is most easily deformed (smallest critical stress) in the direction of the weak plane  $\theta$ . If the patch is loaded in a suboptimal direction, more effort (higher critical stress) is needed to activate the same rearrangement. The second term on the right hand side has two origins: on the one hand, the anisotropic response of the material leads to a variation of the components  $\sigma_{xx}^c$  and  $\sigma_{yy}^c$  of the stress tensor. On the other hand, this term accounts also for the non-zero pre-stresses in the probe.

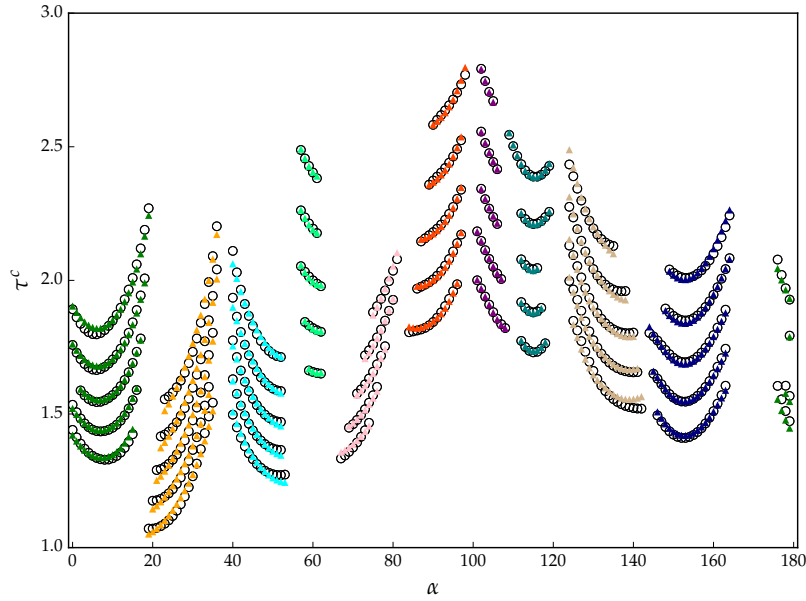


Fig. 3.10 The same inclusion as previously under study is loaded in 180 directions for five different levels of pressure varying between  $\delta = -2\%$  and  $\delta = +2\%$  (black points). Ten rearrangements are identified and then fitted via the Mohr-Coulomb yield criterion (colored triangles). The values of the fit parameters are listed in table 3.1.

For the following analysis, the same inclusion as before is examined. Five pressure levels are considered as the size of the simulation box surface varies between  $\delta = -2\%$  and  $\delta = +2\%$  with steps of  $\delta = 1\%$ . The following steps are performed to detect local shear transformations: first, for every single pressure level, two neighboring critical shear stress values  $\tau^c(\alpha)$  and  $\tau^c(\alpha + 1)$  do not belong to the same local event if one of them is either a local maximum or the computed correlation field  $C(\alpha, \alpha + 1) < 0.8$ . This separates the wells for a given pressure level. Then, for a given  $\alpha$ , if a shear transformation has been identified in two adjacent pressure levels, the two data points are attributed to the same local event. Shear transformations with less than ten data points are neglected in the following analysis. With this algorithm, ten rearrangements were selected for the inclusion under study.

After the correct identification of the wells, all data points belonging to the same event are fitted using equation (3.12). Overall, the measured values of the critical local yield stress and the fitted data show a high degree of agreement (c.f. figure 3.10). Piecewise,  $\tau^c$  is accurately described by a Mohr-Coulomb yield criterion. Sometimes, the fit shows larger discrepancies towards the angular boundaries of a local event. This is possibly due to competing effects between neighboring shear transformations.

Additionally, this particular inclusion seems to be particularly homogeneous: the values of  $\tau_0$  (c.f. tab. 3.1) show only a small variation for the ten events (mean: 1.24, standard deviation: 0.16, min: 0.93, max: 1.47). This observation holds even more for the pressure influence parameter  $\varphi$  (mean:  $-0.24$ , standard deviation: 0.05, min:  $-0.31$ , max:  $-0.16$ ).

### 3.3 Characterization of local rearrangements

Table 3.1 For the inclusion shown in figure 3.10, ten rearrangements were identified and fitted with the Mohr-Coulomb yield criterion (equation (3.12)). The resulting fit parameters  $\tau_0$  and  $\varphi$  are listed in the table below.

	$\theta [^\circ]$	$\tau_0$	$\varphi$
▲	$6 \pm 6$	$1.15 \pm 0.27$	$-0.21 \pm 0.12$
▲	$14 \pm 11$	$0.93 \pm 0.28$	$-0.16 \pm 0.15$
▲	$56 \pm 14$	$1.10 \pm 0.32$	$-0.20 \pm 0.15$
▲	$69 \pm 60$	$1.28 \pm 0.66$	$-0.26 \pm 0.41$
▲	$65 \pm 33$	$1.23 \pm 0.42$	$-0.17 \pm 0.36$
▲	$87 \pm 24$	$1.47 \pm 0.41$	$-0.31 \pm 0.22$
▲	$106 \pm 35$	$1.34 \pm 0.62$	$-0.31 \pm 0.27$
▲	$114 \pm 15$	$1.39 \pm 0.50$	$-0.26 \pm 0.17$
▲	$139 \pm 10$	$1.32 \pm 0.30$	$-0.22 \pm 0.15$
▲	$154 \pm 7$	$1.20 \pm 0.28$	$-0.25 \pm 0.13$

Hitherto, the analysis focused on a single inclusion: a circle of radius  $R_{free} = 5$  containing 80 atoms. Naturally, one would like to extend the study to the entire sample to answer the following questions: what is the number of weak planes in the full system? In other words, how many shear transformations are accessible? What are the distributions of the two parameters  $\tau_0$  and  $\varphi$ ? How does the number of encoded shear transformations change with the preparation of the sample, e.g. for supercooled liquids at different temperatures?

Heretofore, there are no answers to these questions. The difficulty remains to accurately and automatically detect the wells, i.e. the shear transformations. In the following section, first, an example will be given that illustrates the problem. Subsequently, possible solutions will be proposed and discussed.

#### 3.3.5 Problems to detect wells in the shear stress landscape

Until now, the analysis discussion has focused on a single inclusion. This is due to the fact, that the critical shear stress  $\tau^c$  does not show the behavior depicted in figure 3.10 for all patches. For other inclusions, there are hardly any wells in the critical shear stress landscape identifiable (c.f. figure 3.11). Remarkably, the vertical shift due to a pressure change is still observable for most loading directions. Yet, the dot product  $C$  between the displacement field of two instabilities shows the characteristic red triangles (see figure 3.12). Measurements, as shown in figure 3.11, make it difficult to automatically detect shear transformations. In the following section, an explanation for these observations is given. Afterwards, possible solutions are proposed.

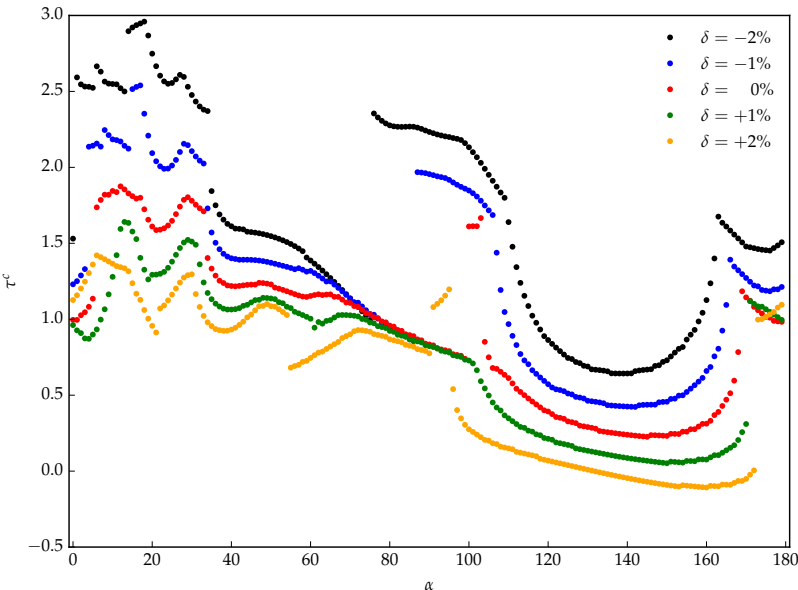


Fig. 3.11 Example of an inclusion, for which it is difficult to identify wells in the critical shear stress landscape.

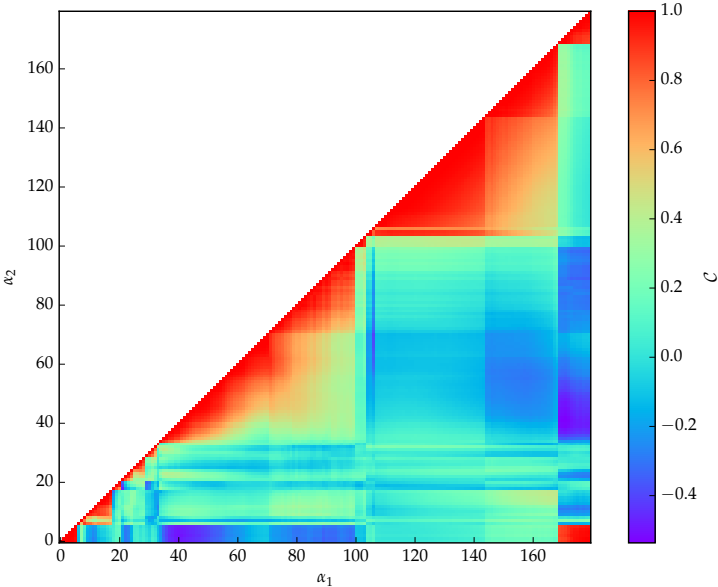


Fig. 3.12 Although, the critical shear stress does not show the typical wells (c.f. figure 3.11), the dot product of the displacement field of two instabilities  $C$  shows the characteristic red triangles. As an example,  $C$  is shown for  $\delta = 0\%$  for the same inclusion depicted in figure 3.11.

#### 3.3.6 Suggested solutions

The local yield stress method allows one to look at the atomistic structure of a glass through a mesoscope - it unveils the shear transformations encoded into the glassy structure. Yet, to continue the analogy, the mesoscope seems to be sometimes out of focus, as some inclusions do not show the characteristic stress wells. One can try to focus on a shear transformation by adjusting the position or the size of the inclusion. Yet, this approach is not easily feasible to perform a statistical analysis.

There are several approaches to deal with these difficulties: one can use the local yield stress method in its current implementation and try to clean up the data i.e. eliminate the data points that do not correspond to characteristic wells. Alternatively, one can also try to improve the local yield stress method: the goal is to place the inclusion in a more natural environment and remove the frozen boundaries. At the same time, it is desirable not to lose control over the size of the inclusion. A shear transformation should still only be activated within a predefined length scale.

A simple means to limit the influence of the frozen boundaries is to increase the size of the inclusion. However, this comes with two caveats: first, as aforementioned, a larger patch acts as a low pass filter. Within a given site, only the smallest stress barrier can be detected. Hence, a larger patch size reduces the spatial resolution, as rearrangements, characterized by larger stress barriers cannot be identified. Additionally, there is no guarantee that the weakest stress shear transformation is close to the center of the inclusion. Thus, the problem of the frozen boundaries persists.

In another attempt to improve the measurement, the criterion to detect a local event was changed. Instead of a drop in the shear component of the stress tensor, a reduction of the von Mises stress

$$\sigma_{vM} = \sqrt{\left(\frac{\sigma_{yy} - \sigma_{xx}}{2}\right)^2 + \sigma_{xy}^2} \quad (3.13)$$

signals the occurrence of a plastic rearrangement. This however, has only minuscule effects on the resulting measurement itself. The aforementioned problems recur.

A more promising approach seems to improve the method itself by removing the frozen boundaries. The idea is to place the inclusion in a continuous elastic medium. Thereby, a local event is forced to occur within the patch, where the atoms are fully relaxed. While the principal idea of an elastic medium is compelling, its implementation has its challenges. For instance, the elastic matrix surrounding the patch can be modeled by replacing the Lennard-Jones interactions with harmonic springs. However, this leads - for certain distances - to an unphysical model with a negative spring constant. This can be overcome by replacing the Lennard-Jones potential in this range by a polynomial function of higher order. A drawback of this approach is that a priori there is no cut off for the elastic medium. One has to deal with the entire sample. The local yield stress method loses one of its features: being computationally efficient by dividing the system into small parts and parallelizing the calculation.

### 3.4 Conclusions

In chapter 1, it was pointed out that plasticity in amorphous materials is an active field of research. Due to the lack of long range order, there are an overwhelming number of degrees of freedom on the atomistic level. Trying to capture and describe all this information to understand the material's behavior on the macroscopic level is in vain. Therefore, it is desirable to have an observable on the mesoscopic scale, which filters out the relevant information of the microscopic level. Local yield stresses prove to be a promising candidate.

In the first part of this chapter, an optimal size for the inclusion size of the local yield stress method is estimated. For this purpose, three correlation indicators that assess the relation between local yield stresses and the location of plastic rearrangements forced by remote loading are calculated. From the results obtained, one can conclude that a radius of  $R_{free} = 5$  is a good compromise: such an inclusion size captures the spatially heterogeneous nature of the underlying structure, while at the same time, the patch size is large enough so that the frozen boundaries do not over constrain the system and severely influence the measurement.

Next, the distributions obtained from different values of  $R_{free}$  are compared. Additionally, it is shown, that a model, based on the weakest link assumption, can be used to derive the distributions for  $R_{free} > 5$  from the one calculated for  $R_{free} = 5$ . This model also explains that a larger probing radius acts as a low pass filter, since only the smallest stress barrier within a inclusion is detected.

In the second part of this chapter, the object of study are shear transformations activated through the local yield stress method. It is demonstrated that the critical yield stress is sensitive towards the loading direction  $\alpha$ , the overall position of the inclusion and the pressure in the simulation box.

The local yield stress method allows to look at the atomistic configuration of a glass through a mesoscope like apparatus - it unveils the shear transformations encoded into the glassy structure. One can see, that for inclusions with a diameter of approximately ten interatomic distances, discrete effects play a significant role. For a local region, a finite number of configurations are accessible through a shear deformation. Over a range of loading directions, the same instability is activated. This observation is evocative of slip planes of dislocations in crystalline materials.

Furthermore, the critical local shear stress is sensitive towards the pressure in the simulation box. A higher pressure is accompanied by a higher critical shear stress. Additionally, the critical local shear stress of one shear transformation for several pressure levels, is well described by the Mohr-Coulomb yield criterion. The notion of yield criteria has its roots in the description of a material's mechanical response on a macroscopic level. Since the size of a patch is at the lower limit, at which a continuum mechanics description can be applied, the characteristic  $1/\cos(2(\theta - \alpha))$  dependency is not observed for all local rearrangements. In addition, in the current implementation of the local yield stress method, the frozen boundaries constrain the patch and can influence the resulting measurements. This chapter concludes with a series of suggestions how the method itself can be enhanced, by placing the inclusion in an elastic medium.

## Chapter 4

# Relation between local yield stresses and the dynamics of supercooled liquids

### 4.1 Preliminary remarks

Over the last 10-15 years, many different order parameters (also called structural indicators) have been proposed to capture the subtle structural change a liquid undergoes upon cooling. The argument put forward is usually based on the capability of the order parameter to predict the kinetics of a supercooled liquid, when only the initial configuration of the material is known. The aim is to show, for instance, that dynamical heterogeneities can already be seen in the initial configuration, when applying the right structural measure. Most of the proposed order parameters have a common denominator: they do not allow any conclusion on the nature of the actual relaxation mechanism [69]. This, however, is needed to better understand structural relaxation itself and lead the way to new theoretical ideas to elucidate the glass transition.

In this thesis, a viscous supercooled liquid is regarded as a solid which flows [38, 69]. Adopting this point of view allows to explain structural relaxation using the mechanical properties of the system in its inherent state [1, 74, 119]. This approach lead, for instance, to the development of the shoving model, previously described in chapter 1. Moreover, it was shown that structural relaxation in supercooled liquids can be seen as a series of Eshelby events that introduce long range stress correlations [69]. More commonly, Eshelby events are discussed in the context of plasticity of amorphous solids [70, 80].

In this part, the dynamics of three different supercooled liquids are studied as a series of inherent structures. The succession of local minima of the potential energy not only eliminates thermal vibrations, but enables to focus on the mechanical description of supercooled liquids. The novelty in the present study is given by the characterization of the structure using local yield stresses. Local yield stresses have not only shown a high predictability of mechanically activated events, but they also allow a judgment on the nature of the rearrangements. By design, they are shear transformations.

In this chapter, the connection between local yield stresses and the dynamics of glassy systems is investigated. The main focus is to test the capability of local yield stresses to predict the dynamics.

## 4.2 Simulation setup

All measurements and observations presented in this chapter were obtained from the following setup of simulations: three temperatures were chosen ( $T = 0.32$ ,  $T = 0.351$  and  $T = 0.5$ ), to cover a wide range of the supercooled regime. The lowest temperature at  $T = 0.32 \simeq 0.85 T_{MCT}$  is located in the deeply supercooled regime. Activated processes dominate the relaxation process. In contrast, the highest temperature  $T = 0.5 \simeq 1.04 T_{onset}$  is close to the onset temperature  $T_{onset}$ . At this temperature, activated dynamics start to set in, but they are not the dominant contribution to diffusive behavior. The third temperature  $T = 0.351 \simeq 0.93 T_{MCT}$  is in between the two. At each temperature, 20 configurations containing  $10^4$  atoms each were equilibrated. To limit the influence of thermal fluctuations, molecular dynamics simulations were performed in the isoconfigurational ensemble. For every initial configuration, 100 independent equilibrium molecular dynamics runs were performed using randomized starting velocities. For the molecular dynamics simulations, the integration step was set to  $dt = 0.01$  and the simulated time span (in Lennard-Jones units) was  $10^6$  for  $T = 0.32$ ,  $10^4$  for  $T = 0.351$  and  $10^3$  at the highest temperature  $T = 0.5$ . Snapshots of the system were saved at logarithmically increasing time points. Nine configurations per decade are stored.

Local yield stresses are calculated for the initial inherent structures. Contrary to mechanically activated rearrangements, thermally induced excitations are statistically isotropic, in the sense that they do not have a preferred direction. Moreover, for activated dynamics, it is expected that the smallest accessible barrier dominates the transition statistics. Thus, a new observable  $\Delta\tau_{min}^c$  is introduced.  $\Delta\tau_{min}^c$  is the minimum measured local yield stress barrier among all of the probed directions

$$\Delta\tau_{min}^c = \min_{\alpha}(\Delta\tau^c(\alpha)). \quad (4.1)$$

$\Delta\tau_{min}^c$  is sensitive towards the temperature at which the liquid was prepared. Figure 4.1 shows the distribution of  $\Delta\tau_{min}^c$  for the three investigated temperatures. As one can see, the lower the temperature the more the distribution is shifted towards larger values of  $\Delta\tau_{min}^c$ .

Before starting to examine the correlation between local stress barriers and the dynamics, some time scales for the binary mixture at these three temperatures are introduced. Figure 4.2 shows the self-intermediate scattering function for the three temperatures. Using the self-intermediate scattering function, one can deduce the macroscopic relaxation time, as described in section 2.2

$$\tau_{\alpha} = 12,100 \pm 355 \quad \text{for } T = 0.32, \quad (4.2)$$

$$\tau_{\alpha} = 289 \pm 4 \quad \text{for } T = 0.351, \quad (4.3)$$

$$\tau_{\alpha} = 8.97 \pm 0.18 \quad \text{for } T = 0.5. \quad (4.4)$$

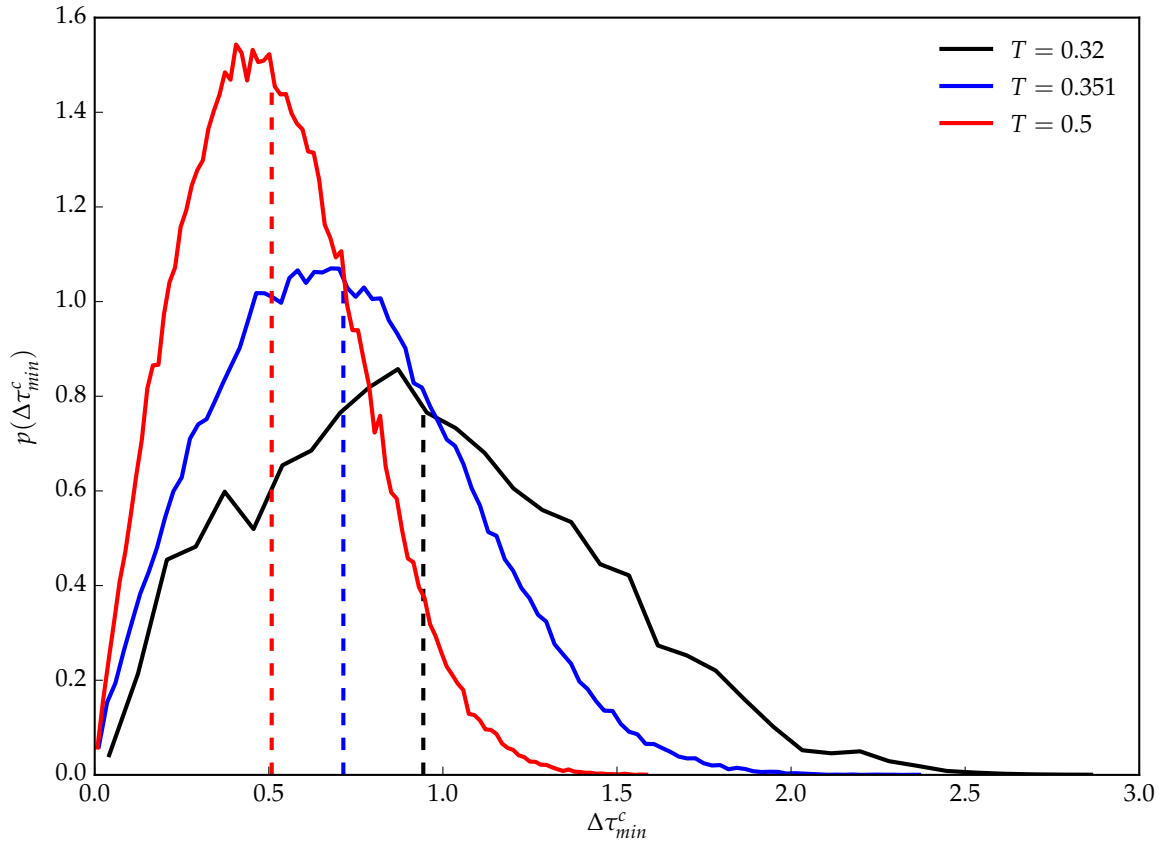


Fig. 4.1 Probability distribution of  $\Delta\tau_{min}^c$  for the three investigated temperatures. The dotted lines correspond to the mean value of the distribution  $\langle\Delta\tau_{min}^c\rangle = 0.94, 0.71$  and  $0.51$  for  $T = 0.32, 0.351$  and  $0.5$ , respectively.

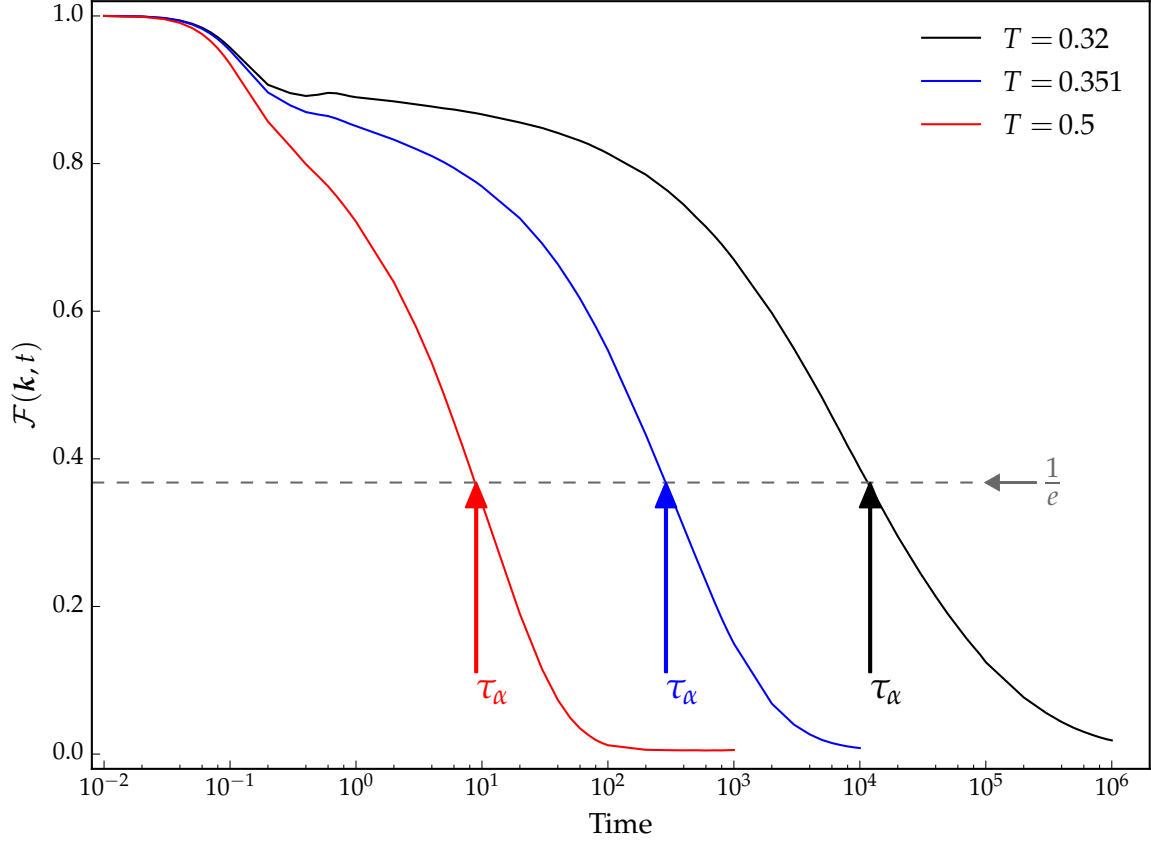


Fig. 4.2 Self-intermediate scattering function for the three temperatures under investigation. The arrows indicate the macroscopic relaxation time  $\tau_\alpha = 9, 289$  and  $12072$  from highest to lowest  $T$ .

In figure 4.3, the average mean squared displacement

$$\langle \mathbf{r}^2 \rangle = \left\langle \frac{1}{N} \sum_{i=1}^N |\mathbf{r}_i(t) - \mathbf{r}_i(0)|^2 \right\rangle \quad (4.5)$$

is reported. Similar to the self-intermediate scattering function, one can identify different regimes. Through the change of slope one can distinguish the ballistic regime on short time scales and the diffusive behavior at long time scales [18]. Similar to the self-intermediate scattering function, the two regimes are separated by a plateau at lower temperatures. Its length corresponds to the time molecules need to break out of the cage formed by their neighbors.

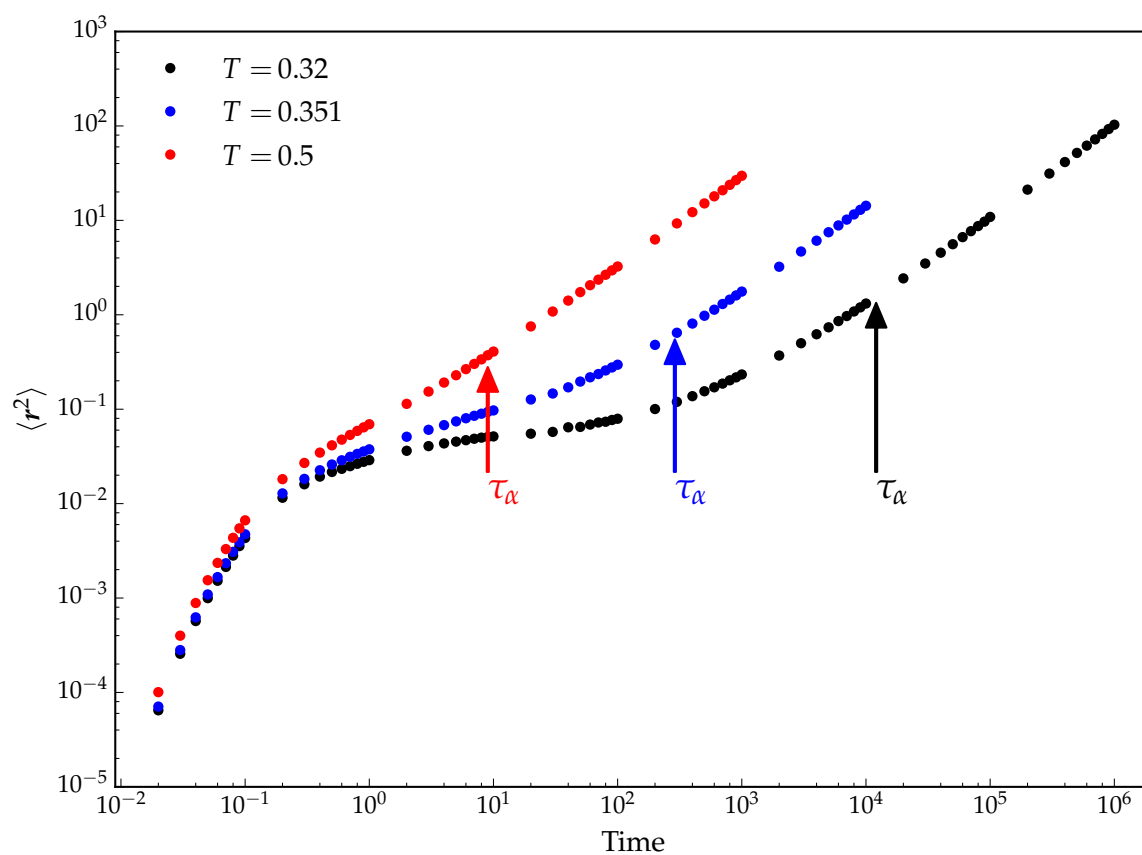


Fig. 4.3 Mean square displacement  $\langle r^2 \rangle$  as a function of time on log-log scale. On short time scales, molecules rattle in the cages formed by their neighbors (ballistic regime). On long time scales, a diffusive behavior sets in. At lower temperatures, similar to the self-intermediate scattering function, a plateau separates the two dynamic regimes.

### 4.3 Correlation between local yield stresses and the dynamics of supercooled liquids

In this part, the correlation between local yield stresses and equilibrium dynamics is presented. Local yield stresses are calculated in the initial inherent state. Their evolution in time is not considered throughout this part. The dynamics of a supercooled liquid can be captured by various physical observables. In the present case, three of them are chosen: the first passage time  $\tau_{FP}$ , the local relaxation time  $\tau_{\alpha}^i$  and the dynamic propensity  $\mathcal{D}$ . Their connection with local yield stresses is quantified through correlation coefficients (c.f. section 4.3.2). In the following section, 4.3.1, the correlation between local yield stresses and the location of local events on short time scales is examined.

#### 4.3.1 Local yield stresses and the location of local rearrangements

A first approach to analyze the correlation between local yield stress thresholds and dynamics is to compare the former to the location of local rearrangements in the system. On short time scales, events are expected to primarily occur in zones of small local yield stresses. Figure 4.4 shows a local yield stress  $\Delta\tau_{min}^c$  map of a supercooled liquid equilibrated at  $T = 0.32$ . Additionally, black circles indicate the location of the first ten rearrangements, numbered in order of appearance. These were detected from a single simulation run, using the aforementioned coarse grained harmonic response. As one can see, most local events occur in blueish regions, characterized by small values of  $\Delta\tau_{min}^c$ .

To further quantify the connection between local yield stress thresholds and the location of local events, the same method as in ref. [13, 88] is applied. A rank correlation coefficient  $\mathcal{C}$  is computed from the cumulative distribution function of local yield stress thresholds  $CDF(\Delta\tau_{min}^c)$

$$\mathcal{C}(\Delta\tau_{min}^c) = \langle 1 - 2CDF(\Delta\tau_{min}^c) \rangle. \quad (4.6)$$

At a site, where a local rearrangement was detected, the corresponding value of  $CDF(\Delta\tau_{min}^c)$  contributes to  $\mathcal{C}$ .  $\langle \dots \rangle$  denotes the ensemble average. By design,  $\mathcal{C}$  is close to 1 (-1), if an event occurs in a region of small (large)  $\Delta\tau_{min}^c$ . A value of  $\mathcal{C} = 0$  means that there is no valuable relation between local yield stresses and the location of rearrangements. It has to be mentioned that equation (4.6) takes neither the renewal of sites nor the elastic noise of rearrangements into account as the cumulative distribution function is only calculated from the as quenched, initial inherent state.

Figure 4.5 shows  $\mathcal{C}$  as **a)** a function of time and **b)** as a function of the total number of occurred events. In both graphs, the correlation shows a strong temperature dependence. The lower the equilibration temperature, the higher the correlation, the slower the decay of  $\mathcal{C}$ . The higher correlation at lower temperatures can be explained as follows: the kinetic behavior is modeled through an activated process. The picture of a system vibrating a long time around a local minimum and only jumping from time to time from one inherent state to another, becomes more accurate as the temperature is lowered. In this

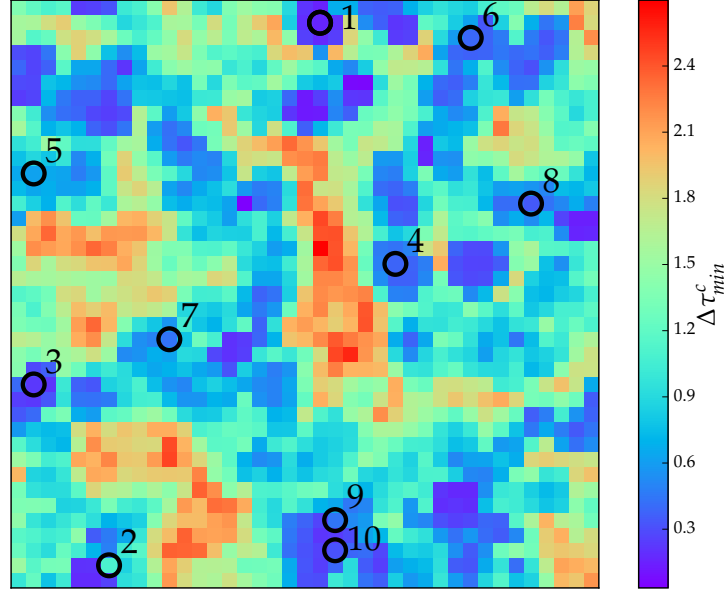


Fig. 4.4 Local yield stress  $\Delta\tau_{min}^c$  map of a configuration equilibrated at  $T = 0.32$ . The location of the first ten rearrangements detected from a single simulation run are indicated by the black circles (numbered in order of their appearance). The events occur primarily in blue regions, corresponding to small values of  $\Delta\tau_{min}^c$ .

description, the height of the barrier  $\Delta$  contributes exponentially to the escape probability

$$p \propto \exp\left(-\frac{\Delta}{T}\right). \quad (4.7)$$

In other words, the system is much more likely to escape over the smallest barrier than any other. Generally speaking, a lower equilibration temperature leads to, on average, larger barriers. Hence, the global minimum becomes more pronounced and completely dominates the escape probability. Contrary, at higher temperatures there are more often several barriers of similar height. The probability that the system escapes via a path other than the global minimum increases. As the *CDF* in equation (4.6) is only calculated from  $\Delta\tau_{min}^c$ , the maximum amplitude of  $\mathcal{C}$  increases for lower temperatures. In figure 4.5 b), the correlation coefficient shows a plateau for the first 25-30 events for the three temperatures under investigation. A plateau in the observable suggests that the same site contributes several times to  $\mathcal{C}$ . Possibly several mechanism are involved, for instance, back and forth type events [25, 35]. For a site, there are two neighboring inherent configurations easily accessible and the system moves back and forth in between the two. Apart from that, it is also imaginable, that a patch visits a series of configurations. In both cases, the events occur in the same location and therefore, the same value of  $\Delta\tau_{min}^c$  contributes several times to  $\mathcal{C}$ , leading to a persistence of the correlation coefficient. Alternatively, it could be possible, that the first events occur on sites with similar *CDF* values and the plateau occurs as a result of the ensemble averaging.

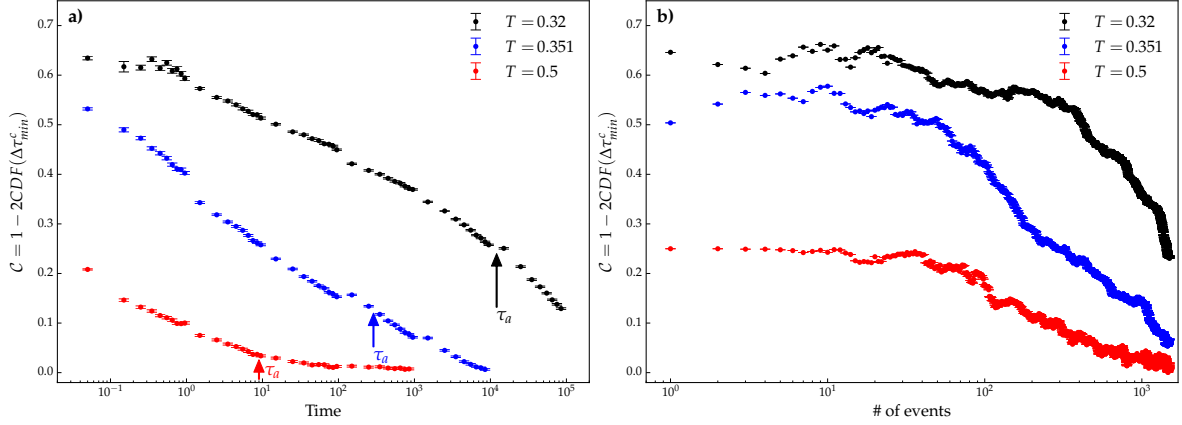


Fig. 4.5 Correlation between the local stress barriers calculated in the as quenched state and the location of local rearrangements as **a)** function of time and **b)** as function of total number of events.

### 4.3.2 Correlation between local yield stresses and dynamic observables

Any structural measure, that claims to capture the complex nature of glassy dynamics, must be held accountable by its ability to predict the dynamics of the system. The question to be answered, is how well the structural measure correlates with the kinetic behavior of the system. For this part of the study, the structure is characterized by the smallest measured stress barrier  $\Delta\tau_{min}^c$ . Local yield stresses are calculated in the as quenched state at time  $t = 0$ . To limit the influence of thermal fluctuations on any kinetic measurement, molecular dynamic simulations are performed in the isoconfigurational ensemble. Prior to the calculation of the correlation between  $\Delta\tau_{min}^c$  and the kinetics of the system, the relation between local yield stresses and the system's dynamic behavior at different temperatures is discussed qualitatively. This section starts with an introduction of three dynamic observables. The focus is on their definition in the isoconfigurational ensemble.

**Dynamic propensity**  $\mathcal{D}_i$ . First introduced by Widmer-Cooper and co-workers in ref. [126], the dynamic propensity is a measure of mobility on the atomistic level. It is defined as follows

$$\mathcal{D}_i(t) = \langle (\mathbf{r}_i(t+t_0) - \mathbf{r}_i(t_0))^2 \rangle_{iso}. \quad (4.8)$$

$\mathcal{D}_i(t)$  corresponds to the isoconfigurational ensemble average of the squared displacement of particle  $i$ . The dynamic propensity has proven to be a meaningful measurement, when trying to relate structure and dynamics in glassy systems [12, 21, 24, 117, 125].

The left column of figure 4.6 shows for each temperature an example of the dynamic propensity. In the right column,  $\Delta\tau_{min}^c$  of the corresponding initial structure computed at  $t = 0$  is depicted. One observes a remarkable similarity between the kinetics (left) and the structure (right). Areas of low propensity are at the same time characterized by larger values of  $\Delta\tau_{min}^c$ . On the contrary, the structure of highly mobile particles (large propensity) shows smaller values of  $\Delta\tau_{min}^c$ . As the temperature is lowered and

### 4.3 Correlation between local yield stresses and the dynamics of supercooled liquids

dynamical heterogeneities become more pronounced, the connection between structure and dynamics is more apparent.

**Coarse graining procedure.** The dynamic propensity as defined by equation (4.8) is an atomistic quantity. Yet, local yield stresses are, by design a coarse grained observable. To compute a correlation coefficient between these two measurements, the following coarse graining procedure is applied on  $\mathcal{D}$ : in accordance with local yield stress computations, a regular lattice with  $R_{sampling} = 2.5$  is defined. The average over all atoms within a coarse graining length  $L$  of a grid node is computed

$$\mathcal{D}(t) = \frac{1}{N} \sum_{i \in L} \mathcal{D}_i(t), \quad (4.9)$$

to obtain the coarse grained dynamic propensity  $\mathcal{D}$ .

Obviously, other coarse graining methods are possible. The influence of the method itself and the coarse graining length  $L$  will be discussed at a later point. For the following calculations, the coarse graining length is set to  $L = 2.5$ , which corresponds also to the interatomic potential cutoff.

**Spearman's rank correlation coefficient.** A correlation coefficient can help to evaluate the strength of the relationship between the dynamics and the structure. Various correlation functions exist to quantify the relation between two observables. In the present case, the Spearman's rank correlation coefficient  $\rho_S$  is used, which was previously applied in similar contexts [24, 51, 118]. An advantage of  $\rho_S$  is its non-parametric nature. It evaluates the statistical dependence between the ranking of two variables. In other words,  $\rho_S$  describes how well the relationship between two variables can be expressed using a monotonic function.  $\rho_S$  can be computed using the following formula

$$\rho_S(X, Y) = 1 - \frac{6 \sum_{i=1}^N d_i^2}{N(N^2 - 1)}, \quad (4.10)$$

$$d_i = rg(X_i) - rg(Y_i), \quad (4.11)$$

where  $rg(X_i)$  corresponds to the rank of the observable  $X_i$ ,  $d_i$  is the rank difference between the two variables and  $N$  is the number of observations. A perfect correlation of  $+1$  or  $-1$  is achieved if  $X$  is a monotone function of  $Y$  (or vice versa).

Figure 4.7 shows the absolute value of Spearman's rank correlation coefficient between the local yield stresses, computed in the initial state and the dynamic propensity as a function of time. As one can see, the correlation is weak both for short times, where the dynamics did not have enough time to develop spatial correlations, and for long times, where the memory of the initial configuration is lost. For the three temperatures, the peak of the correlation is shortly before the macroscopic relaxation time  $\tau_\alpha$ . The maximum value of  $\rho_S$  strongly depends on the temperature. The lower the temperature, the

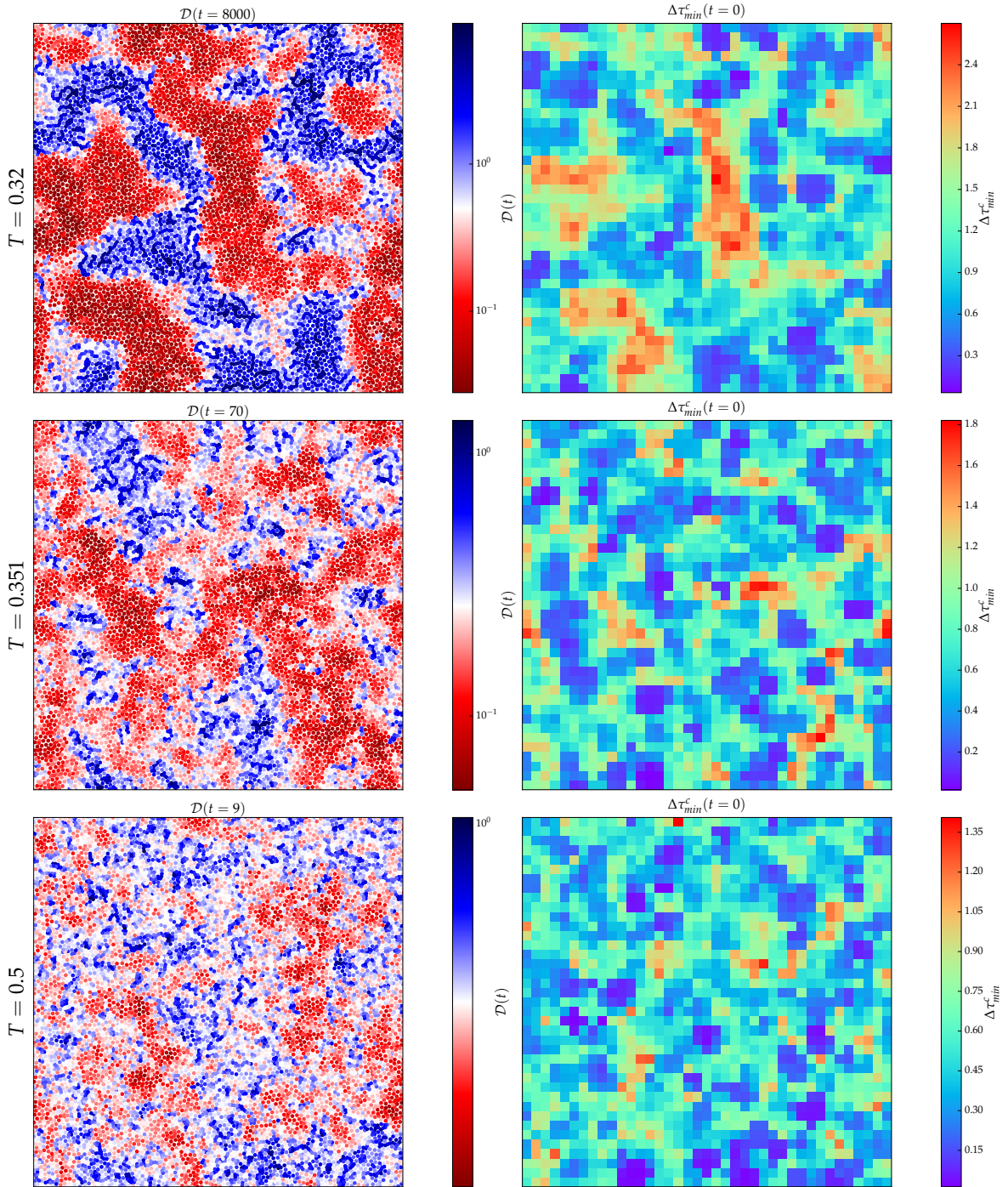


Fig. 4.6 For the three temperatures, the dynamical propensity is shown in the left column. The color of every atom corresponds to its dynamic propensity value. Highly mobile particles are blue, whereas atoms that hardly moved are colored in red. in the right column,  $\Delta\tau_{min}^c$ , computed from the initial configuration is shown. Zones of high propensity are marked by smaller stress barriers. Atoms in patches with large stress barriers barely move. As the temperature is lowered, this connection becomes more apparent .

### 4.3 Correlation between local yield stresses and the dynamics of supercooled liquids

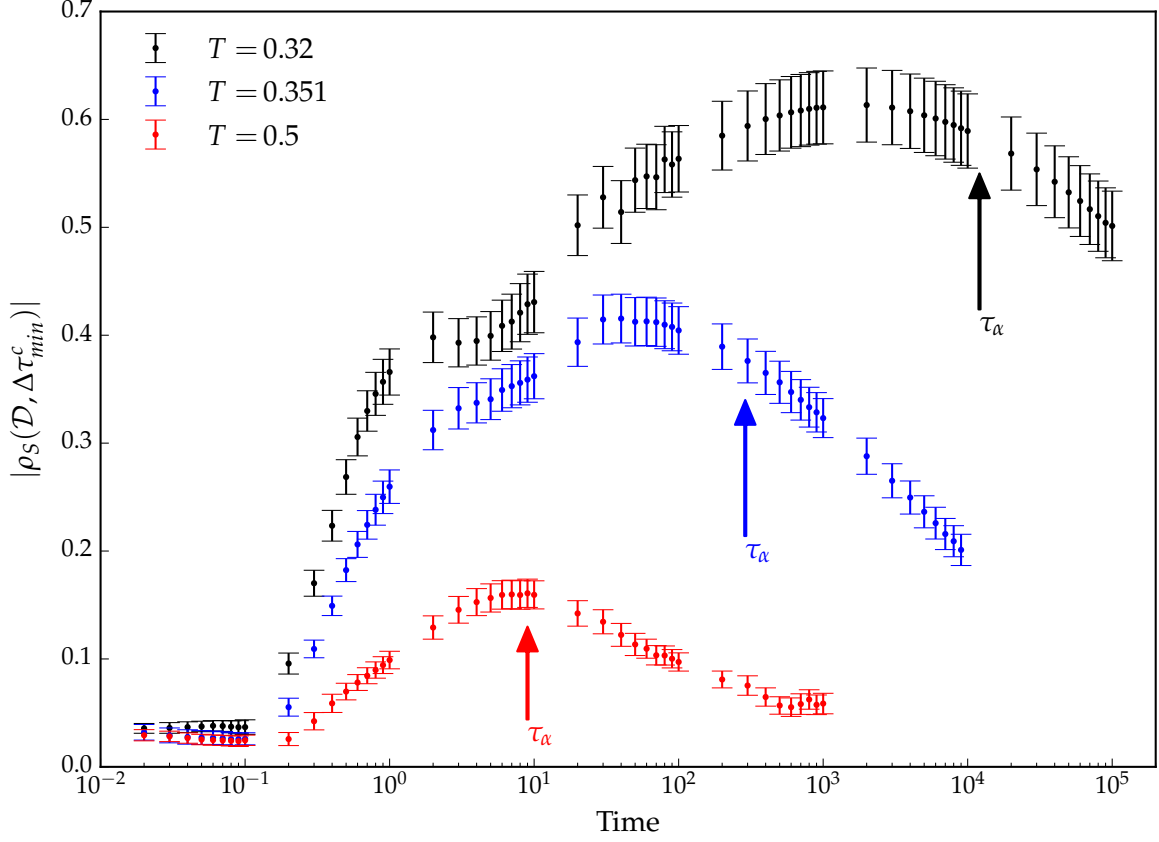


Fig. 4.7 Absolute value of Spearman's rank correlation coefficient between the coarse grained dynamic propensity  $\mathcal{D}$  and  $\Delta\tau_{min}^c$  for the three investigated temperatures. The coarse graining length is set to  $L = 2.5$ . The arrows indicate the macroscopic relaxation time  $\tau_\alpha$ .

better the correlation. A peak of

$$\max(\rho_S(\Delta\tau_{min}^c, \mathcal{D}; t = 7000)) = 0.61 \pm 0.03 \quad \text{for } T = 0.32, \quad (4.12)$$

$$\max(\rho_S(\Delta\tau_{min}^c, \mathcal{D}; t = 40)) = 0.42 \pm 0.02 \quad \text{for } T = 0.351, \quad (4.13)$$

$$\max(\rho_S(\Delta\tau_{min}^c, \mathcal{D}; t = 7)) = 0.16 \pm 0.01 \quad \text{for } T = 0.5, \quad (4.14)$$

is measured for the three supercooled liquids, respectively. This strong correlation at low temperatures demonstrates, that local yield stresses indeed capture a significant part of the structural information relevant for the ensuing activated dynamics. Additionally, this confirms that dynamical heterogeneities are of structural origin: configurational stable regions, with large local yield stress values, do not move significantly over an extended period of time.

**Local relaxation time  $\tau_\alpha^i$ .** Another observable that captures the structural relaxation process is the local relaxation time  $\tau_\alpha^i$ . Following the idea proposed by Tong and Tanaka [118],  $\tau_\alpha^i$  is an atomistic

## Relation between local yield stresses and the dynamics of supercooled liquids

quantity. It is calculated similar to its macroscopic counterpart (c.f. section 2.2). To distinguish the two, a superscript  $i$  is added to the local quantity. The local relaxation time is calculated in the following way: first, the self-intermediate scattering function per atom is calculated and averaged over the isoconfigurational ensemble

$$\mathcal{F}^i(\mathbf{k}, t) = \langle \exp(-i\mathbf{k} \cdot (\Delta\mathbf{r}_i(t) - \Delta\mathbf{r}_i^{cage}(t))) \rangle_{iso} \quad (4.15)$$

$$\Delta\mathbf{r}_i(t) = \mathbf{r}_i(t_0 + t) - \mathbf{r}_i(t_0) \quad (4.16)$$

$$\Delta\mathbf{r}_i^{cage} = \frac{1}{N_i} \sum_{j=1}^{N_i} \mathbf{r}_j(t_0 + t) - \mathbf{r}_j(t_0). \quad (4.17)$$

As for the macroscopic computation of  $\mathcal{F}$ , the cage relative displacement field is used and  $\mathbf{k}$  is set to the first peak of the static structure factor. Next, for every atom the local relaxation time  $\tau_\alpha^i$  is defined as follows

$$\mathcal{F}^i(\mathbf{k}, t = \tau_\alpha^i) = \frac{1}{e}. \quad (4.18)$$

$\mathcal{F}^i(\mathbf{k}, t)$  measures locally the similarity of two atomistic configurations. The local relaxation time thus indicates the point in time, when, due to local rearrangements, the similarity of two configurations has reached a value of  $1/e$ . However,  $\tau_\alpha^i$  does not contain any information about how often a zone has rearranged during this time span.

At the lower temperatures, parts of the systems are so stable that the atoms do not move enough to assign a local relaxation time. Consequently, these atoms are omitted for the subsequent computations of correlations coefficients. This concerns only 0.744% of all atoms at  $T = 0.32$  and 0.025% of all particles at  $T = 0.351$ . The local relaxation time can be attributed to all atoms at  $T = 0.5$ .

The same coarse graining procedure, previously described for the dynamic propensity, is applied to the local relaxation time  $\tau_\alpha^i$ . The coarse graining length is set to  $L = 2.5$ . For each temperature, one example of the coarse grained  $\tau_\alpha^i$  is shown in the left column of figure 4.8. The corresponding  $\Delta\tau_{min}^c$  field of the initial configuration is depicted in the right column. Visually, one can identify a strong connection between the local relaxation time and the local structure. Particles in soft areas have a shorter relaxation time. On the contrary, atoms in patches with large stress barriers have a longer local relaxation time. At lower temperatures, this connection between dynamics and structure becomes stronger, as the underlying landscape increasingly influences the kinetics. This observation can be quantified, using Spearman's rank correlation coefficient. Averaged over 20 samples, one obtains for the three temperatures

$$\rho_S(\Delta\tau_{min}^c, \tau_\alpha^i) = 0.67 \pm 0.01 \quad \text{at } T = 0.32, \quad (4.19)$$

$$\rho_S(\Delta\tau_{min}^c, \tau_\alpha^i) = 0.45 \pm 0.01 \quad \text{at } T = 0.351, \quad (4.20)$$

$$\rho_S(\Delta\tau_{min}^c, \tau_\alpha^i) = 0.18 \pm 0.01 \quad \text{at } T = 0.5, \quad (4.21)$$

respectively.

### 4.3 Correlation between local yield stresses and the dynamics of supercooled liquids

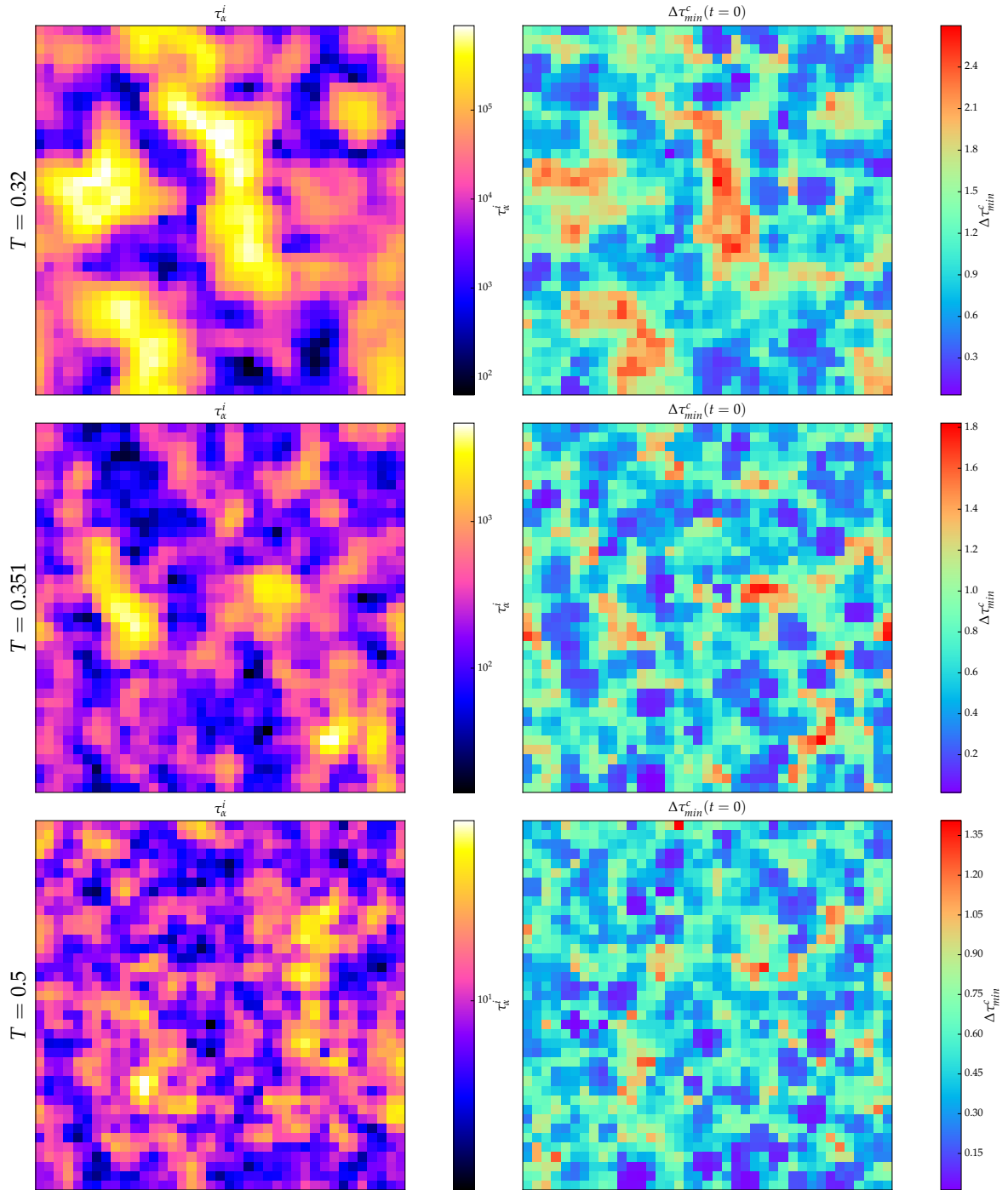


Fig. 4.8 An example of the coarse grained ( $L = 2.5$ ) local relaxation time for each temperature is shown in the left column. On the right hand side, the corresponding  $\Delta\tau_{min}^c$  field is shown. The correlation coefficient between the two fields is  $\rho_S = 0.75$ ,  $\rho_S = 0.48$  and  $\rho_S = 0.25$  from top to bottom.

## Relation between local yield stresses and the dynamics of supercooled liquids

---

**First passage time  $\tau_{FP}$ .** The third kinetic observable, considered in the present study, is the first passage time  $\tau_{FP}$ . It signals the point in time during a simulation run, when a region in space rearranges for the first time. It thus indicates, how long the initial structure has not changed. At the same time, it is also an estimate what temporal resolution is needed to observe a local event. To attribute  $\tau_{FP}$  to a site, local rearrangements are detected using the coarse grained harmonic response, described previously in section 2.5. The spatial resolution of sites, for which the first passage time is determined, is the same as for the computation of local yield stresses. Conceptually, the first passage time is very similar to the trapping time commonly used in the context of kinetic Monte Carlo simulations [109].

As before for the dynamic propensity and the local relaxation time, the isoconfigurational ensemble average is calculated for every site

$$\tau_{FP} = \langle \tau_{FP} \rangle_{iso}. \quad (4.22)$$

Especially at the lower temperatures, not all sites in all replica registered a rearrangement over the full course of the simulation run. As a consequence, these sites are omitted for the subsequent analysis. At the lowest temperature  $T = 0.32$ , there are 0.25% of the sites, where not all replica rearranged. At  $T = 0.351$  and at the highest temperature  $T = 0.5$ , every site in all replica has undergone a local rearrangement.

Averaged over 20 samples one obtains for Spearman's rank correlation coefficient between the local yield stress  $\Delta\tau_{min}^c$  and the first passage time  $\tau_{FP}$  for the three temperatures

$$\rho_S(\Delta\tau_{min}^c, \tau_{FP}) = 0.69 \pm 0.01 \quad \text{for } T = 0.32, \quad (4.23)$$

$$\rho_S(\Delta\tau_{min}^c, \tau_{FP}) = 0.53 \pm 0.01 \quad \text{for } T = 0.351, \quad (4.24)$$

$$\rho_S(\Delta\tau_{min}^c, \tau_{FP}) = 0.19 \pm 0.01 \quad \text{for } T = 0.5. \quad (4.25)$$

At the lowest temperature, an excellent correlation coefficient of almost 0.7 is achieved. The decrease of the correlation coefficient at higher temperatures is expected as the imprint of the structure vanishes.  $T = 0.5$  is close to the onset temperature ( $T_{onset} = 0.48$ ), which marks the beginning of the landscape influence regime.

The comparison between the local yield stresses computed in the initial state and the three kinetic observables delivers a coherent picture: a strong connection between the initial structure and the ensuing kinetics is established. Particles in regions, characterized by small stress barriers, move greater distances; hence, their local relaxation time is shorter. Additionally, they overcome their initial barrier sooner as a shorter first passage time is observed for these sites. In contrast, if for an inclusion a larger stress barrier is measured, during the ensuing dynamics, the atoms will stay in their initial configuration for a longer period of time. It takes these particles more time to rearrange for the first time. Consequently, their dynamic propensity is smaller over the duration of the simulation run.

### 4.3 Correlation between local yield stresses and the dynamics of supercooled liquids

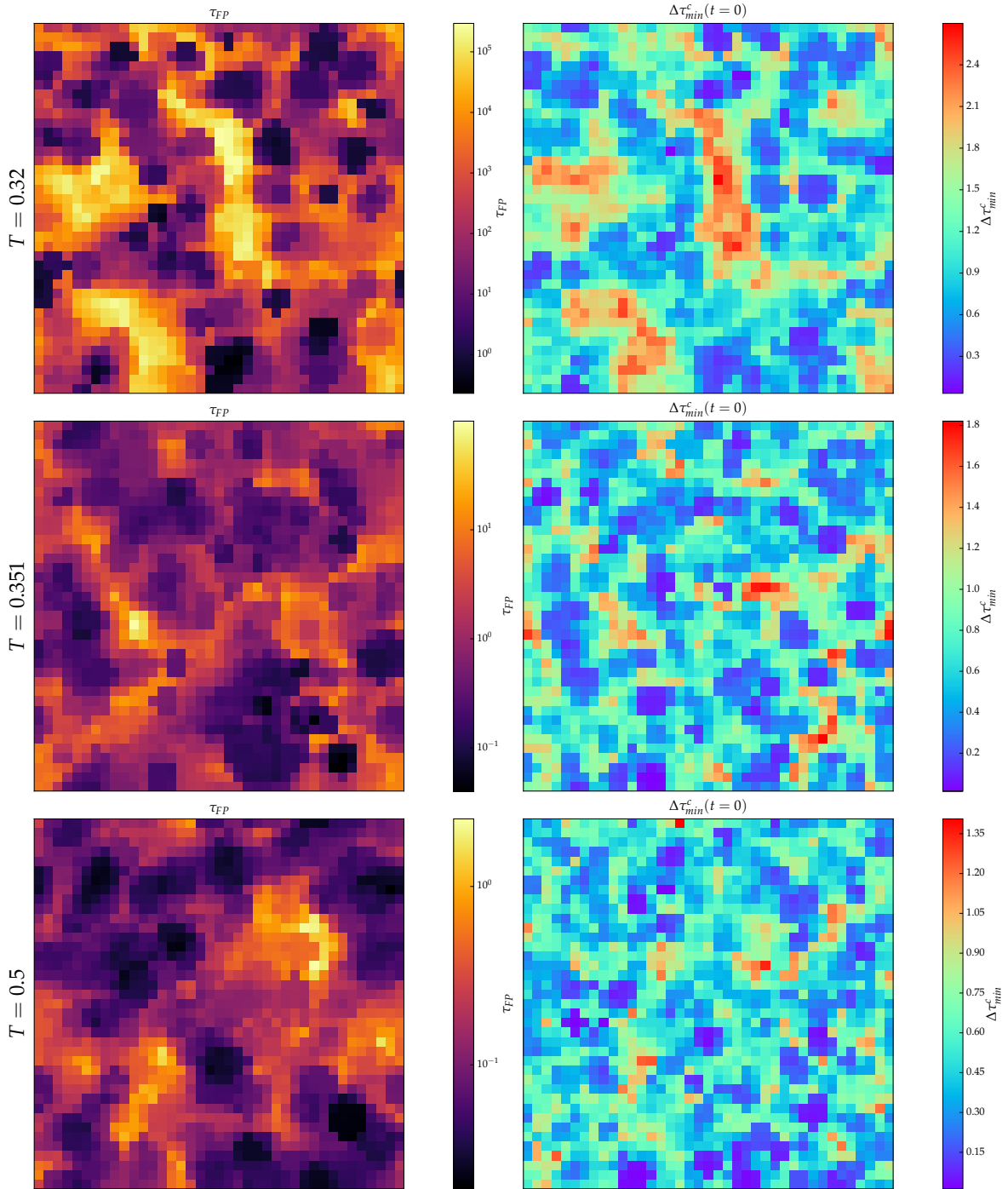


Fig. 4.9 The left column shows for each temperature one example of the isoconfigurational ensemble averaged first passage time  $\tau_{FP}$ . In the right column the corresponding  $\Delta\tau_{min}^c$  field calculated at  $t = 0$  is shown. As for the dynamic propensity (fig. 4.6) and the local relaxation time (fig. 4.8) the connection between structure and dynamics becomes stronger as the temperature is lowered. For these three examples, Spearman's rank correlation is  $\rho_S = 0.78$ ,  $\rho_S = 0.52$  and  $\rho_S = 0.23$  from top to bottom.

### 4.3.3 On the influence of the coarse graining procedure

In the previous section, the correlation between the coarse grained dynamic propensity as well as the local relaxation time and the local yield stresses was presented. In the following paragraphs, the influence of the coarse graining protocol itself and the dependency on the length scale  $L$  will be discussed.

Berthier and Jack conclude in ref. [21] that the search for a meaningful relation between static and dynamic properties of glass forming liquids on an atomistic level is fruitless. However, there exists a connection between the two on a larger length scale. Therefore, a coarse graining procedure is needed for atomistic observables.

A first procedure was earlier given by equation (4.9): first, a lattice with  $R_{sampling} = 2.5$  is defined. The coarse grained quantity of the atomistic field is the mean of all atoms within a distance  $L$  of a grid node

$$\mathcal{D} = \frac{1}{N} \sum_{i \in L} \mathcal{D}_i. \quad (4.26)$$

$\mathcal{D}$  denotes the coarse grained field and  $\mathcal{D}_i$  is the atomistic observable. All particles within a radius  $L$  of a lattice point contribute equally to the coarse grained field.

Yet, other coarse graining procedures are possible: for instance, the contribution of every particle (within the length  $L$ ) can be exponentially weighted as a function of its distance  $d$  to the lattice point

$$\mathcal{D} = \frac{\sum_{i \in L} \mathcal{D}_i \exp\left(-\frac{d}{L}\right)}{\sum_{i \in L} \exp\left(-\frac{d}{L}\right)}. \quad (4.27)$$

As before,  $\mathcal{D}$  denotes the coarse grained field and  $\mathcal{D}_i$  is the atomistic observable.

In order to test the influence of the coarse graining protocol, the absolute value of Spearman's rank correlation coefficient  $\rho_S$ , computed between  $\mathcal{D}$  and  $\Delta\tau_{min}^c$ , is shown in figure 4.10. The dynamic propensity is coarse grained using equation (4.26) as well as equation (4.27). Both times, the coarse graining length is set to  $L = 2.5$ . As one can see, the coarse graining protocol itself does not change the results qualitatively. Also quantitatively, there are only minor differences between the two procedures. At intermediate time scales, the exponential weighted curve is always slightly lower than the simple mean. After the correlation peak, both methods yield the same result, as the two curves start to superimpose each other.

In the previous paragraph, it was shown that the coarse graining method itself does not change the interpretation of the results. Next, the dependency of the correlation on the coarse graining length scale  $L$  will be examined. For this purpose, the local relaxation time is coarse grained using equation (4.26) for different lengths between  $L = 1$  and  $L = 5$ . In addition, no coarse graining is applied and the correlation is computed using the trajectory of single particles. To this end, only the atom closest to the grid point is taken into consideration ( $L = 0$ ). The resulting correlation coefficients are plotted as a function of  $L$  in figure 4.11. As one can see, the correlation is weak for single particle trajectories. Yet, a rapid increase in the correlation is observed for small values of  $L$ . For all three temperatures, the peak of the correlation is at  $L = 3$ . This length is slightly larger than the potential cut off  $R_{cut} = 2.5$ .

### 4.3 Correlation between local yield stresses and the dynamics of supercooled liquids

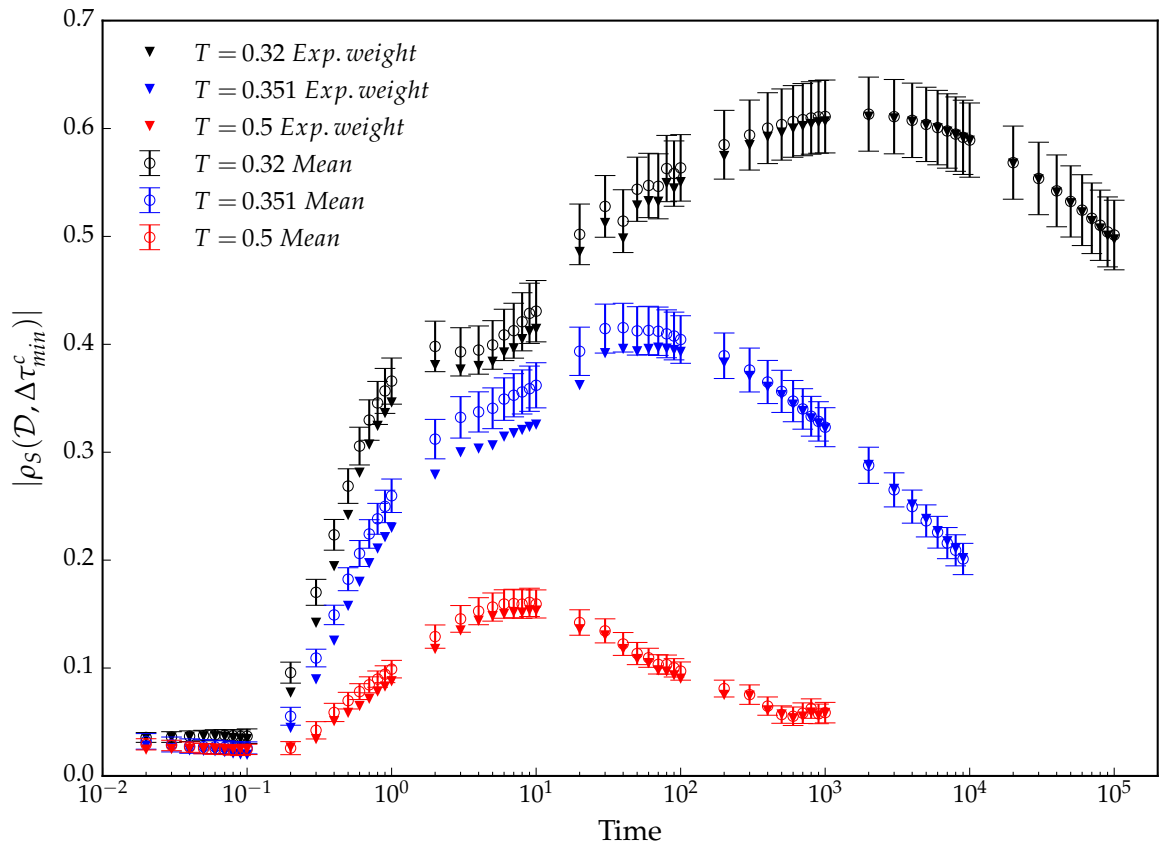


Fig. 4.10 For most data points,  $\rho_S$  calculated using the exponentially weighted dynamic propensity (filled triangles) is within the uncertainty of the correlation computed using equation (4.26) (open symbols with errorbars).

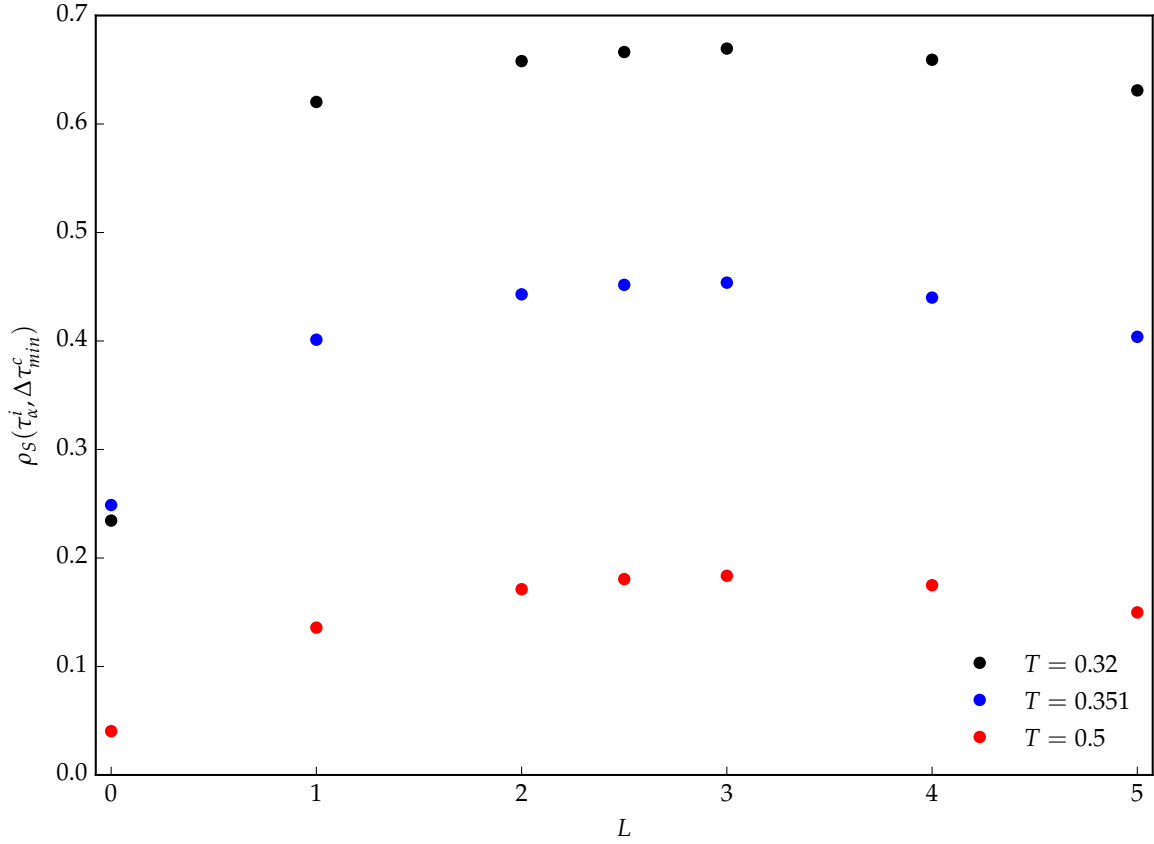


Fig. 4.11 Spearman's rank correlation coefficient computed between  $\Delta\tau_{min}^c$  and the local relaxation time  $\tau_\alpha^i$  as a function of the coarse graining length  $L$ . The correlation between structure and single particle trajectories is weak ( $L = 0$ ). Yet, there exists a strong connection on a greater length scale. For all three temperatures, the highest correlation is found for  $L = 3.0$ . This length is slightly larger than the potential cut off ( $R_{cut} = 2.5$ ).

One last remark has to be made concerning the coarse graining procedure: by looking at figure 4.6, one might rightly ask, whether a coarse graining on the dynamic propensity is necessary. Indeed, qualitatively, the behavior of the resulting Spearman's correlation coefficient does not change whether a coarse graining is applied or not. Yet, at the lowest temperature, the maximum value of  $\rho_S$  is approximately 4 percentage points higher if a coarse graining length  $L = 2.5$  is used.

#### 4.3.4 Comparison with other structural indicators or computational methods

It might be interesting to compare how the previously presented predictability of local yield stresses compares with other structural indicators and computational methods. However, a one-on-one comparison remains difficult, as the systems under study vary. Not only are different particle mixtures and interaction potentials used, but also the dimensionality alternates between two and three. Yet, an attempt

### 4.3 Correlation between local yield stresses and the dynamics of supercooled liquids

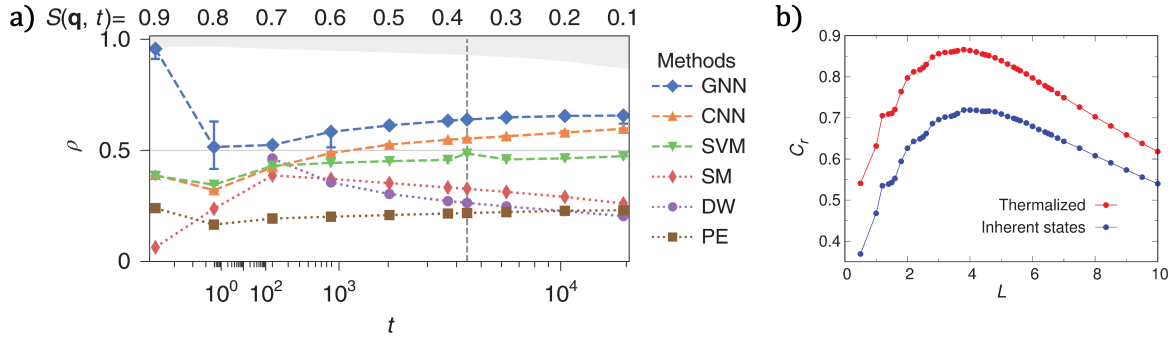


Fig. 4.12 In **a)** on the left hand side, the Pearson correlation of propensity predictions is depicted. The graph neural network (GNN) outperforms other machine learning techniques (e.g. convolutional neural networks (CNN)). The persistence of the correlation at over a long period of time is remarkable. In **b)** on the right hand side, the Spearman's rank correlation coefficient between the local relaxation time and structural order as a function of the coarse graining length  $L$  is shown. Figures a) and b) are adapted from refs. [12] and [118], respectively.

is made to put the computed correlation coefficients into perspective. All results discussed below are obtained using supercooled liquids, where the relaxation time is in the order off  $\tau_\alpha \approx 10^4$ .

Bapst and co-workers use a state of the art machine learning technique [12]. Their graph neural network achieves on very short time scales an almost perfect Pearson correlation for the prediction of the propensity (c.f. figure 4.12 a) ) Next, as the simulated time span increases, the correlation sharply drops to about 0.5 and afterwards slowly increases to approximately 0.6. The last data point of the correlation is recorded at a time, where the self-intermediate scattering function has already declined to 0.1. This long persisting, high predictability of the propensity is a remarkable feature of the graph neural network. Yet, the insight into the physical processes at play remain very limited using a graph neural network.

Tong et al. use a geometric indicator to characterize the structure [117, 118]. In 2D, the basic structural unit are triangles formed by three neighboring particles. Structural order is expressed as the deviation from a “perfect triangle”, where all three neighbors are in touch. At the lowest temperature studied, Spearman's rank correlation between this structural order parameter and the local relaxation time reaches values greater then 0.85, when using an appropriate coarse graining (c.f. figure 4.12 b) ). Interestingly, they obtain this correlation using the thermalized dynamics. The correlation coefficient computed using inherent states is lower, approximately 0.7. In sharp contrast to the machine learning approach, this real space structural indicator has a straight forward interpretation: sterically favored structures, with a high local packing, show slow dynamics. Although, these vastly different approaches made it possible to establish an unprecedented link between the dynamics and structure of supercooled liquids, the underlying mechanism of structural relaxation remains elusive.

This comparison shows that local yield stresses can compete with other structural indicators to predict the dynamics of an equilibrated supercooled liquid and they need not to shy away from any other computational method. Additionally, due to their real space nature, all measurements have a physical

meaning and do not need an complex interpretation: structural relaxation events can be understood as shear events along weak planes and are strongly localized in space.

#### 4.4 First passage time as a random variable

A welcome feature of the first passage time is, in combination with the isoconfigurational ensemble, its interpretation as a random variable. Its statistics can give insights into the process involved in structural relaxation. For instance, the distribution of  $\tau_{FP}$  can help to illustrate what kind of statistical processes and random variables can be used to describe and model the relaxation of supercooled liquids.

For example, one can think of a simplistic and maybe naive approach: the object of study is a liquid in the deeply supercooled regime, well below the mode coupling temperature  $T_{MCT}$ . Activated dynamics dominate the relaxation process. As an additional simplification, interactions between rearrangements (long range elastic interactions, avalanches, etc.) are neglected. Each local event is considered to be independent of its environment. Under these assumptions, the first passage time of a given site is exponentially distributed

$$p(\tau_{FP}) = \lambda \exp(-\lambda \tau_{FP}), \quad (4.28)$$

where the parameter  $\lambda$  determines the rate of a local event.  $\lambda$  depends on the location in the sample. A soft region will have a higher rate than a hard region.

To test this hypothesis, the distribution of first passage times must be calculated. From a technical point of view, 100 replica, which corresponds to 100  $\tau_{FP}$  measurements for a single site, are insufficient to provide a meaningful distribution. Yet, by rescaling every random variable by its mean  $\tau_{FP}/\langle\tau_{FP}\rangle$ , one can circumvent this problem by gathering the statistics of all sites: if all random variables are exponentially distributed, the resulting distribution of the rescaled random variables is an exponential distribution with a rate of  $\lambda = 1$ .

Figure 4.13 shows the distribution of the rescaled first passage time  $\tau_{FP}/\langle\tau_{FP}\rangle$  for the three temperatures. The additional green line corresponds to an exponential distribution with  $\lambda = 1$ . For small values of  $\tau_{FP}/\langle\tau_{FP}\rangle$ , the distribution decreases in lockstep with the green curve. Surprisingly, the measured distributions deviates significantly for the three temperatures from the green curve for larger values of  $\tau_{FP}/\langle\tau_{FP}\rangle$ : the slope of the measured distributions decreases considerably. It is much shallower. Moreover, there seem to be two kinetic regimes: the first regime for small values of  $\tau_{FP}/\langle\tau_{FP}\rangle$  and the second regime for larger values of the rescaled relaxation time. The change of slope suggests that the dynamics slow down, as it is observed for aging dynamics. This phenomenon seems to be very robust: the same behavior is also observed, when only a subset of the complete data is considered (e.g. only sites with  $\Delta\tau_{min}^c$  or  $\langle\tau_{FP}\rangle$  within a certain range).

A similar behavior was previously reported in ref. [47], where the cavitation in a glass is examined. In this context of aging dynamics, it is the expected behavior, as the stability of the material increases with time. Yet, in the present study, the object of study is the dynamics of a supercooled liquid at thermal equilibrium. A given site should not age before its first rearrangement. However, it needs to be pointed

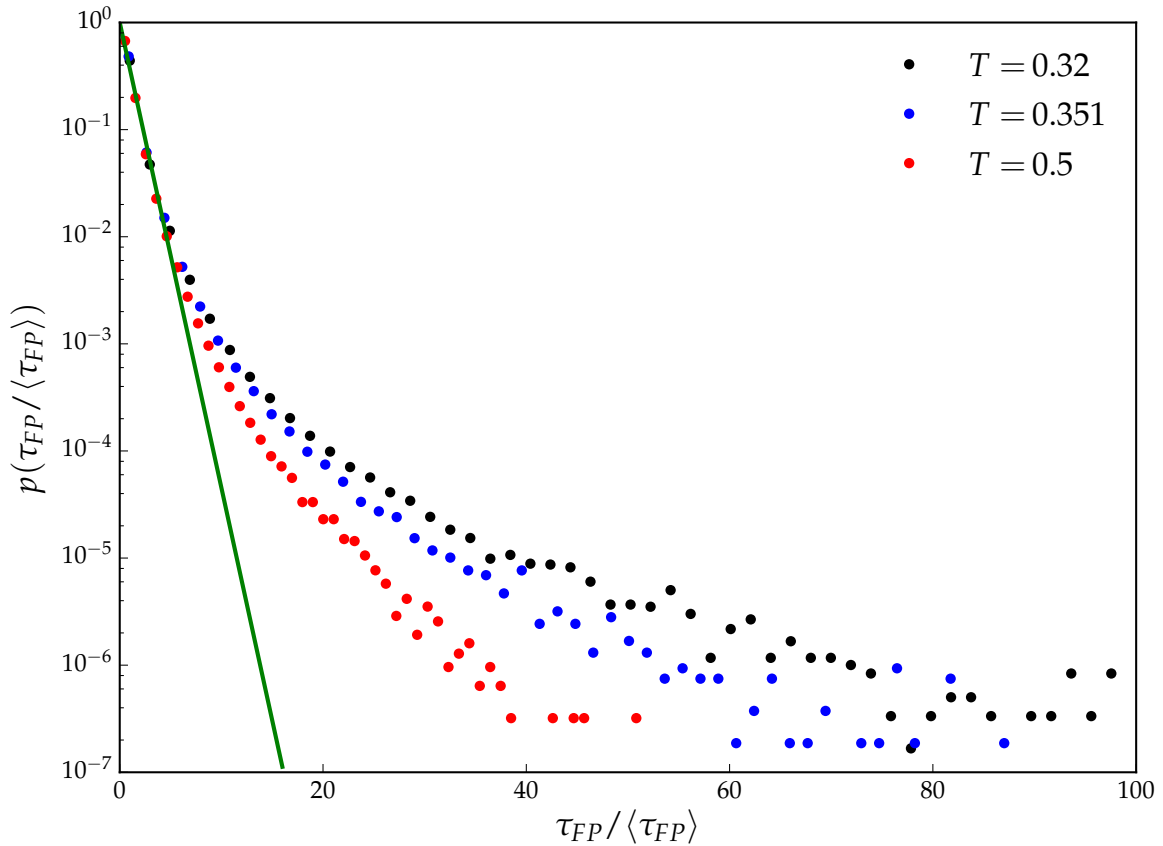


Fig. 4.13 Distribution of the rescaled first passage time  $\tau_{FP}/\langle\tau_{FP}\rangle$  for the three temperatures. The green line corresponds to an exponential distribution with a rate  $\lambda = 1$ . For larger  $\tau_{FP}/\langle\tau_{FP}\rangle$  values, the distribution deviates significantly from the green model line.

out, that Candelier et al. also observe two dynamical regimes in the dynamics of a supercooled liquid at thermal equilibrium [29]. According to the authors, there exists a spatiotemporal hierarchy of relaxation events. The basic process of structural relaxation is a cage jump. Multiple cage jumps form a cluster. Clusters again aggregate into avalanches. In fact, Candelier et al. observe for the lag time between two spatially adjacent clusters two kinetic regimes. As in figure 4.13, the rate of the second regime is much smaller than the one of the first regime. Candelier et al. give the following explanation for this phenomenon: the long lag times correspond to the average time spent in a cage. In other words, the long time regime can be interpreted as the waiting time until a cluster gets underway. However, there exist strong correlations among adjacent clusters. More figuratively speaking, once several cage jumps have formed a cluster, it is highly probable that another cluster close by is activated. These strong spatial correlations between clusters accelerate the dynamics and explain the short time regime. In the literature, the acceleration of the kinetics is more commonly discussed in the context of dynamic facilitation [17, 61, 122].

## Relation between local yield stresses and the dynamics of supercooled liquids

---

After this short digression into the literature, the discussion of figure 4.13 is continued: before proposing possible explanations, of what could cause the two dynamical regimes, the following is remarked. First, at the lowest temperature  $T = 0.32$ , for a given site, the first passage time of the slowest replica is up to two orders of magnitude longer than the fastest replica for that specific site. Second, the two dynamical regimes are not equally distributed. For 98% of all data points  $p(\tau_{FP}/\langle\tau_{FP}\rangle) \geq 10^{-2}$ . It is the short time regime that dominates the distribution.

Previously, it was shown that there is a strong connection between structure and the dynamics of a supercooled liquid. One can suggest that this relation is based on the dominant regime. Under this assumption, the short time regime would be heavily influenced by the initial structure, i.e. the local yield stresses. The origin of the long time regime remains an open question. In the beginning of this part, the assumption was made that each local event is independent and that no interactions occur between them. However, as shown by Lemaître, atomistic rearrangements cause long range elastic interactions [69]. Could this elastic noise cause the aging-like effect? If this is the case, the elastic interactions would lead to a stabilization of certain sites, i.e. the barrier, which a site has to overcome increases. However, new questions arise: why would the elastic noise on average slow down the mechanics? Could these elastic kicks also lead to a destabilization, i.e. a decrease of the barrier height and thus, accelerate the dynamics?

This phenomenon of the two kinetic regimes can also result from an erroneous measurement. Possible methodological weaknesses need to be assessed: for instance, an incorrect detection of a plastic rearrangement can falsify the resulting distribution. In the present study, a threshold on the coarse grained harmonic response is used to decide whether or not a site has rearranged. If the threshold is too high, this will lead to an artificial increase of the first passage time, because not the first rearrangement is registered, but the second or third local event. In contrast, a threshold too small unnaturally reduces  $\tau_{FP}$ , as the harmonic response signals an event even though no rearrangement has taken place. Although, as described in section 2.5, a threshold was used that accounts for sample to sample fluctuations, the possibility that an incorrect  $\tau_{FP}$  measurement enters the distribution cannot be excluded. However, neither from the distribution of the coarse grained harmonic response nor from its atomistic counterpart, a natural threshold emerged, that would allow to separate active from passive sites. In a further analysis, one could develop the potential energy landscape up to a higher order (i.e. going beyond the harmonic response), in the hope that a natural threshold emerges. Alternatively, it is also possible to use a completely different method to detect atomistic rearrangements. For instance, the local strain per atom can also be used to detect local events [85, 132]. In that case, as soon as the strain reaches a certain value, a rearrangement has taken place. However, using this method one faces the same pitfall as before since a value for the threshold needs to be selected.

Another source of error is related to the logarithmic sampling. As the simulated time span increases, one loses temporal resolution. On short simulated time scales, the temporal resolution of ten snapshots per decade might be satisfying. Yet, the longer the simulation run, the longer the time window  $dt$  between two stored snapshots. For the lowest temperature  $dt$  is up to  $10^5$ . As a result, back and forth type of events can be missed. At the same time, a linear sampling with a sufficiently small time window

$dt$  between two snapshots demands excessive storage capacities. To add some numbers: using the logarithmic sampling, approximately 5.5 TB of storage is needed for the three temperatures. Ultimately, the trade-off for a higher temporal resolution are much shorter simulated time spans.

Since the origin of the second kinetic regime is unclear and affects only 2% of all data points, they are not considered in the ensuing analysis.

## 4.5 Escape time $\tau_{esc}$

Previously, the relation between local yield stresses and dynamic observables was quantified through a correlation coefficient. The excellent results encourage to further study the connection between local stress barriers and the first passage time  $\tau_{FP}$ .

In figure 4.14 the first passage time is shown as a function of  $\Delta\tau_{min}^c/T$ . For better clarity, not several thousand data points are plotted for every temperature, but the first passage time is averaged over  $\Delta\tau_{min}^c/T$  bins of width 0.18 (filled circles). For the two lower temperatures,  $T = 0.32$  and  $T = 0.351$ , one can clearly see that, on average, not only a greater stress barrier leads to a longer first passage time, moreover,  $\tau_{FP}$  seems to grow exponentially with the stress barriers. Even more noticeably, for values  $\Delta\tau_{min}^c/T < 4$ , the slopes of the two curves are almost the same. In contrast, the much shallower slope at  $T = 0.5$ , is a clear indicator, that for this temperature, the influence of the structure vanishes. This is also shown by the previously computed much weaker correlation between structure and dynamics. The underlying structure loses its capability to predict the dynamics. This is expected, as  $T = 0.5$  is above the onset temperature, at which the liquid starts to feel the underlying structural landscape. This confirms once again that for this temperature, activated dynamics do not accurately describe the relaxation process.

These observations support the development of a simple model that relates the  $\Delta\tau_{min}^c$  and  $\tau_{FP}$ . It is assumed that the dynamics of a supercooled liquid are activated and interactions between rearrangements are not taken into consideration. Then, for the escape time, i.e. the time the system needs to overcome a barrier and rearrange, the following ansatz was made previously [82]

$$\tau_{esc} = \frac{1}{f_0} \exp\left(\frac{\Delta E}{T}\right). \quad (4.29)$$

$f_0$  is the attempt frequency,  $T$  is the temperature of the supercooled liquid and  $\Delta E$  is energy barrier of the corresponding rearrangement. In the present study, the energy barrier of a rearrangement is unknown. Yet, the local yield stress method allows to measure a local stress barrier. In analogy with equation (4.29), the following ansatz is proposed

$$\tau_{esc} = \frac{1}{f_0} \exp\left(\frac{a\Delta\tau^c}{T}\right), \quad (4.30)$$

where the energy barrier is replaced by

$$\Delta E = a\Delta\tau^c. \quad (4.31)$$

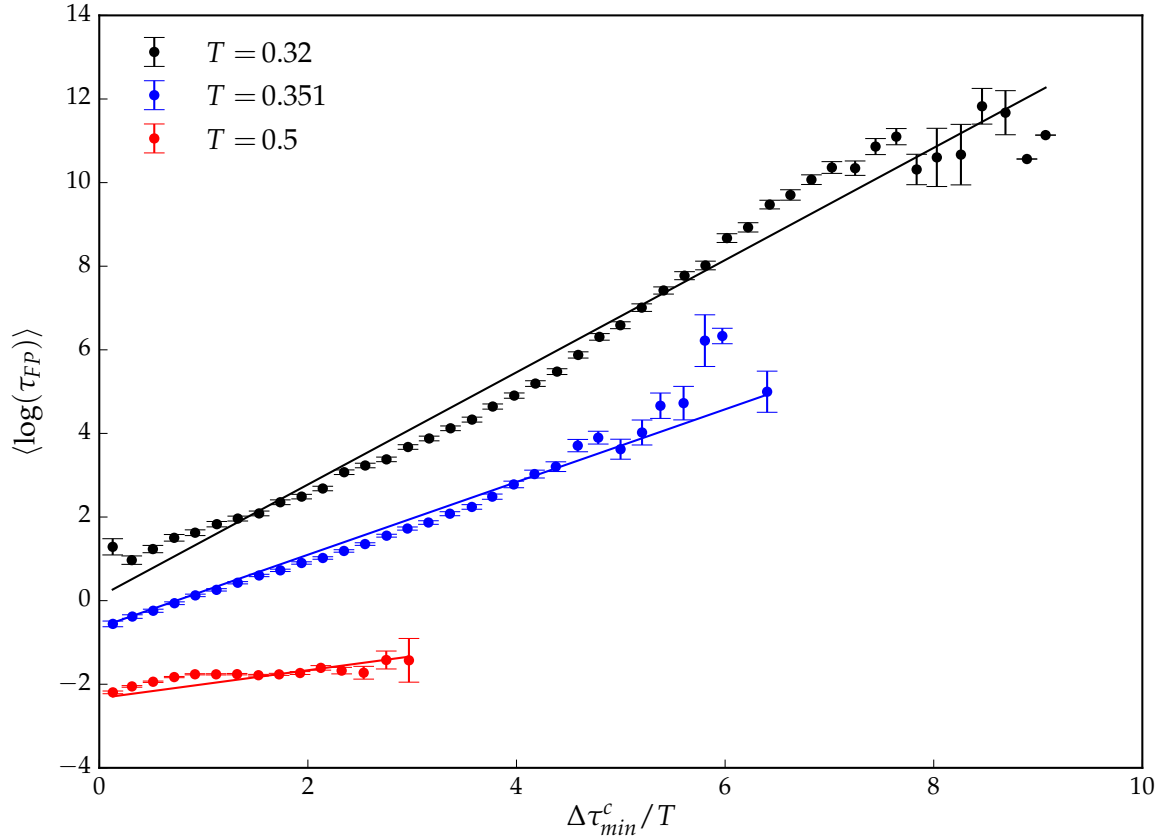


Fig. 4.14 Mean first passage time as a function of the minimum stress barrier rescaled by the temperature. For the two lower temperatures, on average, the data is well described by a fit using equation (4.30). The corresponding fit parameters  $f_0^{-1}$  and  $a$  are listed in tab. 4.1. The much shallower slope at  $T = 0.5$  indicates that the dynamics are no more activated. This is expected, since this is a liquid equilibrated above the onset temperature  $T_{onset} = 0.48$ . The solid lines are obtained by fitting the data via equation (4.30). The values of the resulting fit parameters  $f_0$  and  $a$  are listed in tab. 4.1.

Table 4.1 By fitting the first passage time  $\tau_{FP}$  and  $\Delta\tau_{min}^c$  using equation (4.30), one obtains for the fit parameters  $a$  and  $f_0$  the values listed below.

	$a$	$f_0$
$T = 0.32$	1.34	0.91
$T = 0.351$	0.87	1.89
$T = 0.5$	0.33	10.0

From a dimensional analysis, one can see that  $a$  is a characteristic volume (surface in two dimensions). Thus, it can be interpreted as the activation volume of the rearrangement.

For the three temperatures, the full data of  $\tau_{FP}$  and  $\Delta\tau_{min}^c/T$  (and not the average) is fitted using equation (4.30). The resulting curves are shown in figure 4.14 (solid lines). The values of the fit parameters are listed in tab. 4.1. As aforementioned,  $T = 0.5$  is hardly in the supercooled regime and the assumptions of the model are questionable for this temperature. Therefore, the following discussion focuses primarily on the two other temperatures  $T = 0.32$  and  $T = 0.351$ . As one can see, the model accurately describes the data. The attempt frequency decreases as the temperature is lowered. Between  $T = 0.351$  and  $T = 0.32$  its values drops from  $f_0 = 1.89$  down to  $f_0 = 0.91$ . Comparing the values of the fitted attempt frequency to the Debye model  $f_0 = (2R_{free})^{-1} \sqrt{G/\rho}$  [11, 54], which, in the context of amorphous materials, can serve as an approximation, one finds the same order of magnitude. This reinforces the view point to regard a liquid as solid which flows. The characteristic volume  $a$  increases for lower temperatures. One finds  $a = 1.34$  and  $a = 0.87$  for  $T = 0.32$  and  $T = 0.351$ , respectively.

A series of assumptions were made to deduce equation (4.30). In the following, they are revisited and discussed: first, for every site only the minimum stress barrier is taken into consideration. Obviously, the minimum barrier will dominate the transition statistics, yet there is also the possibility to have two (or more) barriers of similar height. Especially at the higher temperature, this becomes more probable, as the threshold distribution is narrower. Second, in chapter 3, it was shown that the local critical shear stress strongly depends on the loading direction. Due to a limited computational time, in the present study, an angular resolution of  $\Delta\alpha = 10^\circ$  is chosen to calculate the local yield stresses. Therefore, it is highly possible that there is a loading direction, for which a lower stress barrier is measured. Third, as aforementioned, every local event is treated independently of its environment. Yet, it has been shown that there exist spatial correlations between them [69].

## 4.6 Conclusions

In this chapter, the relation between local yield stresses and the dynamics of supercooled liquids were examined. The three temperatures for the investigated liquids were chosen to cover a wide range of the supercooled regime. From the highest to the lowest temperature, the relaxation time increases from 9 to 12000. To test the ability of local yield stresses to predict the dynamics, extensive numerical simulations were performed. On the one hand, local yield stresses are calculated for the initial configurations. On the

## Relation between local yield stresses and the dynamics of supercooled liquids

---

other hand, the simulated time span for the molecular dynamic simulation at thermal equilibrium of the supercooled liquids is orders of magnitude longer than the corresponding relaxation time. To limit the influence of thermal fluctuations, molecular dynamic simulations are performed in the isoconfigurational ensemble.

In the first step, the relationship between the location of the first atomistic rearrangements occurring during a simulation run and the corresponding value of  $\Delta\tau_{min}^c$  is examined. One finds that, first, local events occur preferably in soft zones, characterized by small stress barriers. Second, the amplitude and persistence of the correlation coefficient strongly depend on the temperature: the lower the temperature, the higher the correlation coefficient and the slower the decay. Third, for the first 25-30 events, a plateau of the correlation coefficient is observed, indicating that the same site contributes multiple times. A possible explanation for this phenomenon could be either events of back and forth type or a site visiting a series of configurations.

Next, the relationship between structure and kinetics was quantified by calculating the correlation between local yield stresses and three dynamical observables, i.e. dynamic propensity, local relaxation time and the first passage time. Overall, the results are coherent: in zones with small stress barriers, the first passage time is shorter and, at the same time, the propensity is larger, as the particles move greater distances. Consequently, the local relaxation time is shorter. In contrast, in regions with large barriers, the local atomistic structure is more stable and it takes the particles more time to break up the cage. Ergo, the dynamic propensity is small. For all three kinetic observables, a stronger correlation is found as the temperature is lowered. This confirms that the structure increasingly influences the dynamics at lower temperatures. The maximum amplitude found for the correlation between local yield stresses and the three kinetic observables is comparable to results obtained from state of the art machine learning techniques or other structural indicators [12, 117, 118].

Then, the underlying statistical process of the first passage time is studied. To this end, the distribution of the rescaled first passage time is computed. Remarkably, two dynamical regimes are observed. In the second regime, the dynamics are much slower than in the first. This phenomenon is more commonly expected when studying out of equilibrium dynamics, for instance, the aging of a glass. For now, the exact origin of the two regimes is unknown. However, a similar observation has previously been made in supercooled liquids by Candelier and co-workers [29].

Lastly, it was shown that the first passage time of an inclusion increases exponentially as a function of the smallest measured stress barrier of a patch.

In this study, a strong connection between local yield stresses and the dynamics of supercooled liquids was established. It was shown that kinetic phenomena, such as dynamical heterogeneities, can be traced back to the underlying structure, which is characterized by local stress thresholds. The values one obtains for the correlation coefficient between kinetic observables and local stress barriers are comparable to machine learning techniques and other structural order parameters. However, local yield stress have a lead over other order parameters: it is possible to draw a conclusion on the fundamental process of structural relaxation. This elementary process can be seen as a strongly localized shear event along a characteristic weak plane.

The results obtained can guide the way for future works. In the following section, remaining open questions, concerning especially the two kinetic regimes of the first passage times are addressed. Possible pathways to answer them are pointed out. Then, a glance beyond the scope of this study is taken: propositions are made, in which direction future research could continue. Additionally, a set up for future simulations is exemplified.

## 4.7 Perspectives

First, it should be clarified, whether the two kinetic regimes, observed in the distribution of the rescaled first passage time, are of physical origin or whether they are the result of an erroneous measurement. To eliminate the latter, the same analysis should be performed but with a change in the method to detect local rearrangements. For instance, one could omit the coarse graining procedure on the harmonic response or calculate the harmonic response not between two adjacent inherent states but with respect to the initial configuration. Alternatively, a completely different measure, such as a local strain could be used to identify a local rearrangement. To verify the physical origin of the phenomenon, one could try to reproduce the result using a mesoscale model [26–28]. However, one needs to be very careful interpreting the results, as the input parameters are not the same for the mesoscopic and atomistic model.

Up to now, the focus was placed on examining the influence of local yield stresses on the dynamics of a supercooled liquid. In a further study, it would be interesting to investigate the influence of the dynamics on local yield stresses. In other words, to analyze the evolution of local stress thresholds in time. In figure 4.15, the displacement field of a single rearrangement is depicted on the left hand side. The two additional figures show the critical shear stress  $\tau^c$  in 18 different directions before and after the event **a**) far away from the rearrangement and **b**) very close to the core of the rearrangement. As one can see, the critical shear stress changes in all 18 probed directions, close to core of the relaxation center. After the local event, there is a new local environment and thus, all critical stress values are renewed. Contrary, far away, one observes a persistence of critical shear stresses. They are the same before and after the local event. This example suggests that the renewal of stress thresholds is closely connected to relaxation events. Consequently, a number of questions arise: for instance, after a rearrangement, from which distribution are the new values of the stress thresholds drawn? Is it the same distribution for all sites, or is there a memory effect, i.e. will a weak site still have a small stress barrier after a local rearrangement? At the same time, the persistence of the critical stress should be evaluated. For example, one could try to quantify the amplitude of the elastic noise, by looking at the evolution of the stress tensor in the undeformed state for passive sites, i.e. patches that do not rearrange. Ultimately, once this relationship between relaxation events and the renewal of local yield stresses is verified, one could try to express structural relaxation in terms of local stress thresholds. In other words, to define a correlation function that uses the local yield stresses as input parameter.

So far, much of the discussion was focused on the dynamics at thermal equilibrium. In the future, it would be interesting to go out of equilibrium and study aging and rejuvenation effects on local yield stresses. A possible simulation setup could look as follows: one starts with an initial configuration of an

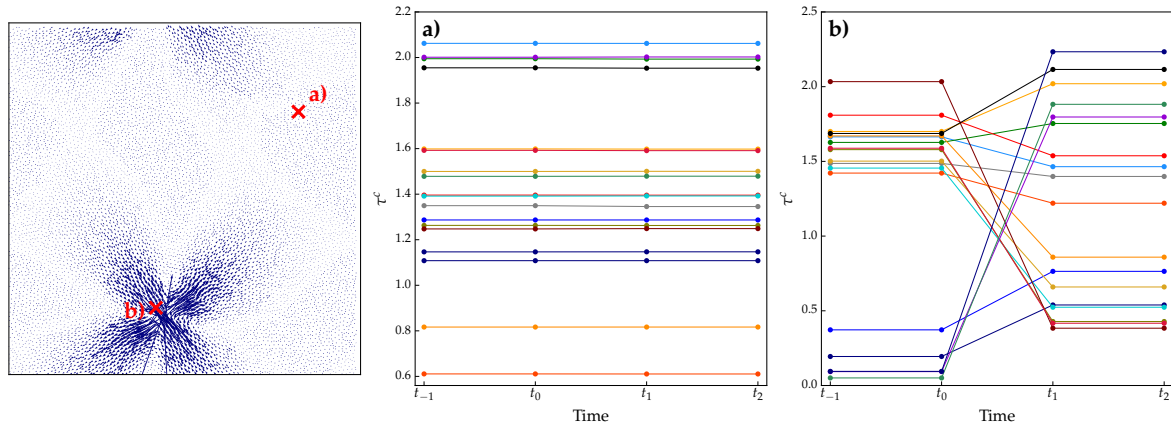


Fig. 4.15 On the left hand side the displacement field of inherent states (magnified 20 times) between  $t = t_0$  and  $t = t_1$  is shown. The two additional figures **a)** and **b)** show the temporal evolution of the local critical shear stress  $\tau^c$  in 18 different directions. As depicted in **a)**, far away, the critical shear stress  $\tau^c$  persists before and after a local event. Close to the core of a rearrangement (shown in **b)**), the critical shear stresses are renewed in all directions.

equilibrated supercooled liquid at temperature  $T = T_1$ . For the ensuing simulation run, the temperature is set to  $T = T_2$ . If  $T_2 > T_1$ , the liquid is heated up. For a simulated time period long enough, the system will be once again equilibrated at  $T_2$ . It is expected, that the distribution of local yield stress thresholds will shift with time towards smaller values, before stabilizing at the new equilibrium position. For  $T_2 < T_1$ , the results depend on the location of  $T_2$  with respect to the numerical glass transition temperature  $T_{comp}$ .  $T_{comp}$  denotes the temperature, where the time to equilibrate the liquid (approximately 100 times the relaxation time) exceeds any reasonable computational time. If  $T_2 > T_{comp}$  a similar behavior as above mentioned is expected: after a sufficiently long waiting time, one obtains once again an equilibrated supercooled liquid at  $T_2$ . This time, however, the distribution of local yield stress thresholds will be shifted to the right, towards larger stress threshold values. If  $T_2$  is below  $T_{comp}$ , the liquid will fall out of equilibrium and form a glass. The distribution of local yield stress thresholds will not await a new stable distribution but will continue to drift towards larger values.

## Chapter 5

# Conclusions

As mentioned in the beginning of this manuscript, the glass transitions remains one of the biggest unsolved problem in solid state physics. Over the last decades, various theoretical concepts were proposed to explain it. Yet, until this day, no theory can explain the glass transition and its accompanying phenomena to its full extend. Many questions remain unanswered.

In this manuscript, an infrequent view point is adopted: supercooled liquids are seen as solids which flow. From this perspective, the drastic kinetic slow down results from the change of the underlying mechanical properties of the system.

In this thesis, the previously developed local yield stress method is extended and applied on glassy systems. In chapter 3, it is shown that the local yield stress method works as a mesoscope: by using the method with an appropriate length scale, one can see that a discrete and finite number of shear transformations are encoded into the atomistic glassy structure. The multidimensional  $x - y - \alpha - p$  space is divided into zones. Each zone can be associated with a shear transformation. The local yield stress method limits the degrees of freedom of the system, by focusing on a small spatial region of the sample. Thus, one can visit these zones in the multidimensional space, which cannot be accessed through remote loading. Over a range of loading directions, the same event is activated. The critical local yield stress shows a characteristic stress well for each rearrangement. The same well can still be identified after displacing the center of the inclusion slightly. Furthermore, these stress wells are strongly pressure dependent. Upon small pressure variations, the well is moved vertically. A higher pressure is accompanied by a larger critical local yield stress; in contrast, a lower pressure leads to a reduction of the critical local yield stress. Additionally, it is found that the stress well, i.e the critical local yield stress of a shear transformation is accurately described by a Mohr-Coulomb yield criterion. However, due to difficulties in the accurate detection of wells in the stress landscape, no statistical analysis could be performed. This is mainly attributed to the frozen boundary conditions in the current implementation of the local yield stress method. Future works should focus on the development flexible boundaries. One idea could be to place the inclusion in an elastic medium.

In chapter 4, a strong connection between local slip thresholds and activated dynamics of supercooled liquids at low temperature is established. The maximum value found for the correlation coefficients

## Conclusions

---

calculated between kinetic observables and local yield stresses are comparable to state of the art machine learning techniques or other structural indicators. Yet, local yield stresses have a big advantage over other order parameters: they allow to draw a conclusion on the fundamental process of structural relaxation. This elementary process can be seen as a strongly localized shear event along a characteristic weak plane. Additionally, it was shown that the first passage time, i.e. the point in time a region rearranges for the first time during a simulation run, can be expressed as a function of the smallest probed stress barrier. Future works should focus on strengthening this relationship between the local stress barriers and the dynamics. The aim could be to describe structural relaxation using local yield stresses as input parameter.

# References

- [1] Abraham, S. and Harrowell, P. (2012). The origin of persistent shear stress in supercooled liquids. *The Journal of Chemical Physics*, 137(1):014506.
- [2] Adam, G. and Gibbs, J. H. (1965). On the Temperature Dependence of Cooperative Relaxation Properties in Glass-Forming Liquids. *The Journal of Chemical Physics*, 43(1):139–146.
- [3] Amon, A., Nguyen, V. B., Bruand, A., Crassous, J., and Clément, E. (2012). Hot Spots in an Athermal System. *Physical Review Letters*, 108(13):135502.
- [4] Andersen, H. C. (2005). Molecular dynamics studies of heterogeneous dynamics and dynamic crossover in supercooled atomic liquids. *Proceedings of the National Academy of Sciences*, 102(19):6686–6691.
- [5] Anderson, D. L. (1995). Through the glass lightly. *Science*, 267(5204):1618–1618.
- [6] Andrianov, A., Biroli, G., and Bouchaud, J.-P. (2009). Mode coupling as a Landau theory of the glass transition. *EPL (Europhysics Letters)*, 88(1):16001.
- [7] Angell, C. (1988). Perspective on the glass transition. *Journal of Physics and Chemistry of Solids*, 49(8):863–871.
- [8] Arceri, F., Landes, F. P., Berthier, L., and Biroli, G. (2020). Glasses and aging: A Statistical Mechanics Perspective. *arXiv:2006.09725 [cond-mat]*.
- [9] Argon, A. (1979). Plastic deformation in metallic glasses. *Acta Metallurgica*, 27(1):47–58.
- [10] Argon, A. and Kuo, H. (1979). Plastic flow in a disordered bubble raft (an analog of a metallic glass). *Materials Science and Engineering*, 39(1):101–109.
- [11] Ashcroft, N. W. and Mermin, N. D. (1995). *Solid State Physics*. Saunders College Publ. [u.a.], Fort Worth, internat. ed., 21. print edition.
- [12] Bapst, V., Keck, T., Grabska-Barwińska, A., Donner, C., Cubuk, E. D., Schoenholz, S. S., Obika, A., Nelson, A. W. R., Back, T., Hassabis, D., and Kohli, P. (2020). Unveiling the predictive power of static structure in glassy systems. *Nature Physics*, 16(4):448–454.
- [13] Barbot, A., Lerbinger, M., Hernandez-Garcia, A., García-García, R., Falk, M. L., Vandembroucq, D., and Patinet, S. (2018). Local yield stress statistics in model amorphous solids. *Physical Review E*, 97(3):033001.
- [14] Barbot, A., Lerbinger, M., Lemaître, A., Vandembroucq, D., and Patinet, S. (2020). Rejuvenation and shear banding in model amorphous solids. *Physical Review E*, 101(3):033001.
- [15] Bässler, H. (1987). Viscous flow in supercooled liquids analyzed in terms of transport theory for random media with energetic disorder. *Physical Review Letters*, 58(8):767–770.

## References

---

- [16] Bengtzelius, U., Gotze, W., and Sjolander, A. (1984). Dynamics of supercooled liquids and the glass transition. *Journal of Physics C: Solid State Physics*, 17(33):5915–5934.
- [17] Bergroth, M. N. J., Vogel, M., and Glotzer, S. C. (2005). Examination of Dynamic Facilitation in Molecular Dynamics Simulations of Glass-Forming Liquids <sup>†</sup>. *The Journal of Physical Chemistry B*, 109(14):6748–6753.
- [18] Berthier, L. and Biroli, G. (2011). Theoretical perspective on the glass transition and amorphous materials. *Reviews of Modern Physics*, 83(2):587–645.
- [19] Berthier, L., Biroli, G., Bouchaud, J.-P., Cipelletti, L., and van Saarloos, W., editors (2011). *Dynamical Heterogeneities in Glasses, Colloids, and Granular Media*. Oxford University Press.
- [20] Berthier, L. and Garrahan, J. P. (2003). Real space origin of temperature crossovers in supercooled liquids. *Physical Review E*, 68(4).
- [21] Berthier, L. and Jack, R. L. (2007). Structure and dynamics of glass formers: Predictability at large length scales. *Physical Review E*, 76(4):041509.
- [22] Biroli, G. and Garrahan, J. P. (2013). Perspective: The glass transition. *The Journal of Chemical Physics*, 138(12):12A301.
- [23] Blank-Burian, M. and Heuer, A. (2018). Shearing small glass-forming systems: A potential energy landscape perspective. *Physical Review E*, 98(3):033002.
- [24] Boattini, E., Marín-Aguilar, S., Mitra, S., Foffi, G., Smallenburg, F., and Fillion, L. (2020). Autonomously revealing hidden local structures in supercooled liquids. *arXiv:2003.00586 [cond-mat]*.
- [25] Büchner, S. and Heuer, A. (2000). Metastable States as a Key to the Dynamics of Supercooled Liquids. *Physical Review Letters*, 84(10):2168–2171.
- [26] Bulatov, V. V. and Argon, A. S. (1994a). A stochastic model for continuum elasto-plastic behavior. I. Numerical approach and strain localization. *Modelling and Simulation in Materials Science and Engineering*, 2(2):167–184.
- [27] Bulatov, V. V. and Argon, A. S. (1994b). A stochastic model for continuum elasto-plastic behavior. II. A study of the glass transition and structural relaxation. *Modelling and Simulation in Materials Science and Engineering*, 2(2):185–202.
- [28] Bulatov, V. V. and Argon, A. S. (1994c). A stochastic model for continuum elasto-plastic behavior. III. Plasticity in ordered versus disordered solids. *Modelling and Simulation in Materials Science and Engineering*, 2(2):203–222.
- [29] Candelier, R., Widmer-Cooper, A., Kummerfeld, J. K., Dauchot, O., Biroli, G., Harrowell, P., and Reichman, D. R. (2010). Spatiotemporal Hierarchy of Relaxation Events, Dynamical Heterogeneities, and Structural Reorganization in a Supercooled Liquid. *Physical Review Letters*, 105(13):135702.
- [30] Cavagna, A. (2009). Supercooled liquids for pedestrians. *Physics Reports*, 476(4–6):51–124.
- [31] Chandler, D. and Garrahan, J. P. (2010). Dynamics on the Way to Forming Glass: Bubbles in Space-Time. *Annual Review of Physical Chemistry*, 61(1):191–217.
- [32] Cubuk, E. D., Schoenholz, S. S., Rieser, J. M., Malone, B. D., Rottler, J., Durian, D. J., Kaxiras, E., and Liu, A. J. (2015). Identifying Structural Flow Defects in Disordered Solids Using Machine-Learning Methods. *Physical Review Letters*, 114(10).

- 
- [33] Debenedetti, P. G. and Stillinger, F. H. (2001). Supercooled liquids and the glass transition. *Nature*, 410(6825):259–267.
- [34] Denny, R. A., Reichman, D. R., and Bouchaud, J.-P. (2003). Trap Models and Slow Dynamics in Supercooled Liquids. *Physical Review Letters*, 90(2):025503.
- [35] Doliwa, B. and Heuer, A. (2003). Energy barriers and activated dynamics in a supercooled Lennard-Jones liquid. *Physical Review E*, 67(3):031506.
- [36] Dyre, J. C. (1987). Master-equation approach to the glass transition. *Physical Review Letters*, 58(8):792–795.
- [37] Dyre, J. C. (1995). Energy master equation: A low-temperature approximation to Bässler’s random-walk model. *Physical Review B*, 51(18):12276–12294.
- [38] Dyre, J. C. (2006). The glass transition and elastic models of glass-forming liquids. *Reviews of Modern Physics*, 78(3):953–972.
- [39] Dyre, J. C. and Olsen, N. B. (2004). Landscape equivalent of the shoving model. *Physical Review E*, 69(4):042501.
- [40] Dyre, J. C., Olsen, N. B., and Christensen, T. (1996). Local elastic expansion model for viscous-flow activation energies of glass-forming molecular liquids. *Physical Review B*, 53(5):2171–2174.
- [41] Ediger, M. (1998). Can density or entropy fluctuations explain enhanced translational diffusion in glass-forming liquids? *Journal of Non-Crystalline Solids*, 235-237:10–18.
- [42] Ediger, M. D. (2000). Spatially Heterogeneous Dynamics in Supercooled Liquids. *Annual Review of Physical Chemistry*, 51(1):99–128.
- [43] Falk, M. L. and Langer, J. S. (1998). Dynamics of viscoplastic deformation in amorphous solids. *Physical Review E*, 57(6):7192–7205.
- [44] Fulcher, G. S. (1925). Analysis of recent measurements of the viscosity of glasses. *Journal of the American Ceramic Society*, 8(6):339–355.
- [45] Goldenfeld, N. (2018). *Lectures on Phase Transitions and the Renormalization Group*. CRC Press.
- [46] Goldstein, M. (1969). Viscous Liquids and the Glass Transition: A Potential Energy Barrier Picture. *The Journal of Chemical Physics*, 51(9):3728–3739.
- [47] Guan, P., Lu, S., Spector, M. J. B., Valavala, P. K., and Falk, M. L. (2013). Cavitation in Amorphous Solids. *Physical Review Letters*, 110(18).
- [48] Hansen, J.-P. and McDonald, I. R. (2007). *Theory of Simple Liquids*. Elsevier / Academic Press, Amsterdam ; Boston, 3rd ed edition.
- [49] Henkelman, G. and Jónsson, H. (2000). Improved tangent estimate in the nudged elastic band method for finding minimum energy paths and saddle points. *The Journal of Chemical Physics*, 113(22):9978–9985.
- [50] Heuer, A. (2008). Exploring the potential energy landscape of glass-forming systems: From inherent structures via metabasins to macroscopic transport. *Journal of Physics: Condensed Matter*, 20(37):373101.

## References

---

- [51] Hocky, G. M., Coslovich, D., Ikeda, A., and Reichman, D. R. (2014). Correlation of Local Order with Particle Mobility in Supercooled Liquids Is Highly System Dependent. *Physical Review Letters*, 113(15):157801.
- [52] Homer, E. R. and Schuh, C. A. (2009). Mesoscale modeling of amorphous metals by shear transformation zone dynamics. *Acta Materialia*, 57(9):2823–2833.
- [53] Hufnagel, T. C., Schuh, C. A., and Falk, M. L. (2016). Deformation of metallic glasses: Recent developments in theory, simulations, and experiments. *Acta Materialia*, 109:375–393.
- [54] Hunklinger, S. (2011). *Festkörperphysik*. Oldenbourg, München, 3., verb. und aktualisierte auf edition.
- [55] Illing, B., Fritschi, S., Kaiser, H., Klix, C. L., Maret, G., and Keim, P. (2017). Mermin–Wagner fluctuations in 2D amorphous solids. *Proceedings of the National Academy of Sciences*, 114(8):1856–1861.
- [56] Irving, J. H. and Kirkwood, J. G. (1950). The Statistical Mechanical Theory of Transport Processes. IV. The Equations of Hydrodynamics. *The Journal of Chemical Physics*, 18(6):817–829.
- [57] Jack, R. L., Dunleavy, A. J., and Royall, C. P. (2014). Information-Theoretic Measurements of Coupling between Structure and Dynamics in Glass Formers. *Physical Review Letters*, 113(9):095703.
- [58] Janssen, L. M. C. (2018). Mode-Coupling Theory of the Glass Transition: A Primer. *Frontiers in Physics*, 6:97.
- [59] Jensen, K. E., Weitz, D. A., and Spaepen, F. (2014). Local shear transformations in deformed and quiescent hard-sphere colloidal glasses. *Physical Review E*, 90(4):042305.
- [60] Kauzmann, W. (1948). The Nature of the Glassy State and the Behavior of Liquids at Low Temperatures. *Chemical Reviews*, 43(2):219–256.
- [61] Keys, A. S., Hedges, L. O., Garrahan, J. P., Glotzer, S. C., and Chandler, D. (2011). Excitations Are Localized and Relaxation Is Hierarchical in Glass-Forming Liquids. *Physical Review X*, 1(2):021013.
- [62] Kim, D., Jeong, D., and Jung, Y. (2014). Dynamic propensity as an indicator of heterogeneity in room-temperature ionic liquids. *Phys. Chem. Chem. Phys.*, 16(36):19712–19719.
- [63] Kirkpatrick, T. R. and Thirumalai, D. (1987). Dynamics of the Structural Glass Transition and the  $p$ -Spin—Interaction Spin-Glass Model. *Physical Review Letters*, 58(20):2091–2094.
- [64] Kirkpatrick, T. R. and Wolynes, P. G. (1987). Connections between some kinetic and equilibrium theories of the glass transition. *Physical Review A*, 35(7):3072–3080.
- [65] Lancon, F., Billard, L., and Chamberod, A. (1984). Structural description of a metallic glass model. *Journal of Physics F: Metal Physics*, 14(3):579–591.
- [66] Landau, L. D., Lifšic, E. M., and Landau, L. D. (2008). *Theory of Elasticity*. Number Vol. 7 in Course of Theoretical Physics. Elsevier, Amsterdam, 3. engl. ed., rev. and enlarged, reprint edition.
- [67] Le Bouil, A., Amon, A., McNamara, S., and Crassous, J. (2014a). Emergence of Cooperativity in Plasticity of Soft Glassy Materials. *Physical Review Letters*, 112(24):246001.
- [68] Le Bouil, A., Amon, A., Sangleboeuf, J.-C., Orain, H., Bésuelle, P., Viggiani, G., Chasle, P., and Crassous, J. (2014b). A biaxial apparatus for the study of heterogeneous and intermittent strains in granular materials. *Granular Matter*, 16(1):1–8.

- [69] Lemaître, A. (2014). Structural Relaxation is a Scale-Free Process. *Physical Review Letters*, 113(24).
- [70] Lemaître, A. and Caroli, C. (2009). Rate-Dependent Avalanche Size in Athermally Sheared Amorphous Solids. *Physical Review Letters*, 103(6):065501.
- [71] Lemaitre, J. and Chaboche, J.-L. (1994). *Mechanics of Solid Materials*. Cambridge university press.
- [72] Lerner, E., Procaccia, I., Rainone, C., and Singh, M. (2018). Protocol dependence of plasticity in ultrastable amorphous solids. *Physical Review E*, 98(6):063001.
- [73] Leutheusser, E. (1984). Dynamical model of the liquid-glass transition. *Physical Review A*, 29(5):2765–2773.
- [74] Levashov, V. A., Morris, J. R., and Egami, T. (2013). The origin of viscosity as seen through atomic level stress correlation function. *The Journal of Chemical Physics*, 138(4):044507.
- [75] Lewandowski, J. J. and Lowhaphandu, P. (2002). Effects of hydrostatic pressure on the flow and fracture of a bulk amorphous metal. *Philosophical Magazine A*, 82(17-18):3427–3441.
- [76] Lund, A. C. and Schuh, C. A. (2003). Yield surface of a simulated metallic glass. *Acta Materialia*, 51(18):5399–5411.
- [77] Makke, A., Perez, M., Rottler, J., Lame, O., and Barrat, J.-L. (2011). Predictors of Cavitation in Glassy Polymers under Tensile Strain: A Coarse-Grained Molecular Dynamics Investigation. *Macromolecular Theory and Simulations*, 20(9):826–836.
- [78] Maloney, C. and Lemaître, A. (2004a). Subextensive Scaling in the Athermal, Quasistatic Limit of Amorphous Matter in Plastic Shear Flow. *Physical Review Letters*, 93(1):016001.
- [79] Maloney, C. and Lemaître, A. (2004b). Universal Breakdown of Elasticity at the Onset of Material Failure. *Physical Review Letters*, 93(19):195501.
- [80] Maloney, C. E. and Lemaître, A. (2006). Amorphous systems in athermal, quasistatic shear. *Physical Review E*, 74(1):016118.
- [81] Mizuno, H., Mossa, S., and Barrat, J.-L. (2013). Measuring spatial distribution of the local elastic modulus in glasses. *Physical Review E*, 87(4).
- [82] Monthus, C. and Bouchaud, J.-P. (1996). Models of traps and glass phenomenology. *Journal of Physics A: Mathematical and General*, 29(14):3847–3869.
- [83] Mooney, M. (1957). A Theory of the Viscosity of a Maxwellian Elastic Liquid. *Transactions of the Society of Rheology*, 1(1):63–94.
- [84] Nicolas, A., Ferrero, E. E., Martens, K., and Barrat, J.-L. (2018). Deformation and flow of amorphous solids: Insights from elastoplastic models. *Reviews of Modern Physics*, 90(4):045006.
- [85] Nicolas, A. and Rottler, J. (2018). Orientation of plastic rearrangements in two-dimensional model glasses under shear. *Physical Review E*, 97(6):063002.
- [86] Pastore, R., Pesce, G., Sasso, A., and Ciamarra, M. P. (2017). Cage Size and Jump Precursors in Glass-Forming Liquids: Experiment and Simulations. *The Journal of Physical Chemistry Letters*, 8(7):1562–1568.

## References

---

- [87] Patinet, S., Barbot, A., Lerbinger, M., Vandembroucq, D., and Lemaître, A. (2020). Origin of the Bauschinger Effect in Amorphous Solids. *Physical Review Letters*, 124(20):205503.
- [88] Patinet, S., Vandembroucq, D., and Falk, M. L. (2016). Connecting local yield stresses with plastic activity in amorphous solids. *Physical Review Letters*, 117(4):045501.
- [89] Plimpton, S. (1993). Fast parallel algorithms for short-range molecular dynamics. Technical Report SAND-91-1144, 10176421.
- [90] Puosi, F., Olivier, J., and Martens, K. (2015). Probing relevant ingredients in mean-field approaches for the athermal rheology of yield stress materials. *Soft Matter*, 11(38):7639–7647.
- [91] Richert, R. (2002). Heterogeneous dynamics in liquids: Fluctuations in space and time. *Journal of Physics: Condensed Matter*, 14(23):R703–R738.
- [92] Rodney, D. and Schuh, C. (2009a). Distribution of Thermally Activated Plastic Events in a Flowing Glass. *Physical Review Letters*, 102(23).
- [93] Rodney, D. and Schuh, C. A. (2009b). Yield stress in metallic glasses: The jamming-unjamming transition studied through Monte Carlo simulations based on the activation-relaxation technique. *Physical Review B*, 80(18).
- [94] Rodney, D., Tanguy, A., and Vandembroucq, D. (2011). Modeling the mechanics of amorphous solids at different length scale and time scale. *Modelling and Simulation in Materials Science and Engineering*, 19(8):083001.
- [95] Rottler, J. and Robbins, M. O. (2001). Yield conditions for deformation of amorphous polymer glasses. *Physical Review E*, 64(5):051801.
- [96] Ruta, B., Pineda, E., and Evenson, Z. (2017). Relaxation processes and physical aging in metallic glasses. *Journal of Physics: Condensed Matter*, 29(50):503002.
- [97] Sastry, S., Debenedetti, P. G., and Stillinger, F. H. (1998). Signatures of distinct dynamical regimes in the energy landscape of a glass-forming liquid. *Nature*, 393(6685):554–557.
- [98] Schall, P., Weitz, D. A., and Spaepen, F. (2007). Structural Rearrangements That Govern Flow in Colloidal Glasses. *Science*, 318(5858):1895–1899.
- [99] Schoenholz, S. S. (2018). Combining Machine Learning and Physics to Understand Glassy Systems. *Journal of Physics: Conference Series*, 1036:012021.
- [100] Schoenholz, S. S., Cubuk, E. D., Kaxiras, E., and Liu, A. J. (2017). Relationship between local structure and relaxation in out-of-equilibrium glassy systems. *Proceedings of the National Academy of Sciences*, 114(2):263–267.
- [101] Schoenholz, S. S., Cubuk, E. D., Sussman, D. M., Kaxiras, E., and Liu, A. J. (2016). A structural approach to relaxation in glassy liquids. *Nature Physics*, 12(5):469–471.
- [102] Schroeder, T. B., Sastry, S., Dyre, J. C., and Glotzer, S. C. (2000). Crossover to Potential Energy Landscape Dominated Dynamics in a Model Glass-forming Liquid. *The Journal of Chemical Physics*, 112(22):9834–9840.
- [103] Schuh, C. A. and Lund, A. C. (2003). Atomistic basis for the plastic yield criterion of metallic glass. *Nature Materials*, 2(7):449–452.
- [104] Shi, Z., Debenedetti, P. G., and Stillinger, F. H. (2013). Relaxation processes in liquids: Variations on a theme by Stokes and Einstein. *The Journal of Chemical Physics*, 138(12):12A526.

- [105] Shiba, H., Kawasaki, T., and Kim, K. (2019). Local Density Fluctuation Governs the Divergence of Viscosity Underlying Elastic and Hydrodynamic Anomalies in a 2D Glass-Forming Liquid. *Physical Review Letters*, 123(26):265501.
- [106] Shiba, H., Yamada, Y., Kawasaki, T., and Kim, K. (2016). Unveiling Dimensionality Dependence of Glassy Dynamics: 2D Infinite Fluctuation Eclipses Inherent Structural Relaxation. *Physical Review Letters*, page 6.
- [107] Sollich, P. (2011). Local strains and yield strains in shear flow of amorphous materials. In *CECAM Workshop*, ACAM, Dublin, Ireland.
- [108] Spaepen, F. (1977). A microscopic mechanism for steady state inhomogeneous flow in metallic glasses. *Acta Metallurgica*, 25(4):407–415.
- [109] Stariolo, D. A. and Cugliandolo, L. F. (2020). Barriers, trapping times, and overlaps between local minima in the dynamics of the disordered Ising p -spin model. *Physical Review E*, 102(2):022126.
- [110] Stillinger, F. H. (1988). Relaxation and flow mechanisms in “fragile” glass-forming liquids. *The Journal of Chemical Physics*, 89(10):6461–6469.
- [111] Stillinger, F. H. and Debenedetti, P. G. (2013). Glass Transition Thermodynamics and Kinetics. *Annual Review of Condensed Matter Physics*, 4(1):263–285.
- [112] Stillinger, F. H. and Weber, T. A. (1982). Hidden structure in liquids. *Physical Review A*, 25(2):978–989.
- [113] Tammann, G. and Hesse, W. (1926). The dependence of viscosity upon the temperature of supercooled liquids. *Z. Anorg. Allg. Chem*, 156:245–257.
- [114] Tanguy, A., Leonforte, F., and Barrat, J. L. (2006). Plastic response of a 2D Lennard-Jones amorphous solid: Detailed analysis of the local rearrangements at very slow strain rate. *The European Physical Journal E*, 20(3):355–364.
- [115] Tarjus, G. (2010). An overview of the theories of the glass transition. *arXiv:1010.2938 [cond-mat]*.
- [116] Tobolsky, A., Powell, R., and Eyring, H. (1943). Frontiers in chemistry. *New York*, pages 125–190.
- [117] Tong, H. and Tanaka, H. (2018). Revealing Hidden Structural Order Controlling Both Fast and Slow Glassy Dynamics in Supercooled Liquids. *Physical Review X*, 8(1):011041.
- [118] Tong, H. and Tanaka, H. (2019). Structural order as a genuine control parameter of dynamics in simple glass formers. *Nature Communications*, 10(1):5596.
- [119] Trachenko, K. and Brazhkin, V. V. (2009). Understanding the problem of glass transition on the basis of elastic waves in a liquid. *Journal of Physics: Condensed Matter*, 21(42):425104.
- [120] Tsamados, M., Tanguy, A., Goldenberg, C., and Barrat, J.-L. (2009). Local elasticity map and plasticity in a model Lennard-Jones glass. *Physical Review E*, 80(2):026112.
- [121] Vogel, H. (1921). Das Temperaturabhängigkeitsgesetz der Viskosität von Flüssigkeiten. *Physikalische Zeitschrift*, 22:645–646.
- [122] Vogel, M. and Glotzer, S. C. (2004). Spatially Heterogeneous Dynamics and Dynamic Facilitation in a Model of Viscous Silica. *Physical Review Letters*, 92(25):255901.

## References

---

- [123] Widmer-Cooper, A. and Harrowell, P. (2005). On the relationship between structure and dynamics in a supercooled liquid. *Journal of Physics: Condensed Matter*, 17(49):S4025–S4034.
- [124] Widmer-Cooper, A. and Harrowell, P. (2006a). Free volume cannot explain the spatial heterogeneity of Debye–Waller factors in a glass-forming binary alloy. *Journal of Non-Crystalline Solids*, 352(42-49):5098–5102.
- [125] Widmer-Cooper, A. and Harrowell, P. (2006b). Predicting the Long-Time Dynamic Heterogeneity in a Supercooled Liquid on the Basis of Short-Time Heterogeneities. *Physical Review Letters*, 96(18):185701.
- [126] Widmer-Cooper, A., Harrowell, P., and Fynewever, H. (2004). How Reproducible Are Dynamic Heterogeneities in a Supercooled Liquid? *Physical Review Letters*, 93(13):135701.
- [127] Widmer-Cooper, A., Perry, H., Harrowell, P., and Reichman, D. R. (2008). Irreversible reorganization in a supercooled liquid originates from localized soft modes. *Nature Physics*, 4(9):711–715.
- [128] Widmer-Cooper, A., Perry, H., Harrowell, P., and Reichman, D. R. (2009). Localized soft modes and the supercooled liquid’s irreversible passage through its configuration space. *The Journal of Chemical Physics*, 131(19):194508.
- [129] Widom, M., Strandburg, K. J., and Swendsen, R. H. (1987). Quasicrystal equilibrium state. *Physical Review Letters*, 58(7):706–709.
- [130] Zhang, B. (2019). Long-wavelength fluctuations and static correlations in quasi-2D colloidal suspensions. *Soft Matter*, page 11.
- [131] Zhang, K. (2016). On the Concept of Static Structure Factor. *arXiv:1606.03610 [cond-mat]*.
- [132] Zimmerman, J. A., Bammann, D. J., and Gao, H. (2009). Deformation gradients for continuum mechanical analysis of atomistic simulations. *International Journal of Solids and Structures*, 46(2):238–253.

## Appendix A

# Rejuvenation and shear banding in model amorphous solids

The aim of this article was to study the evolution of local yield stresses during shear banding. To this end, 100 samples following the gradual quench protocol (c.f. chapter 2) are prepared. These configurations are then subject to a global athermal quasistatic shear deformation. Local yield stresses are calculated at various amounts of strain.

In this article, it is shown that a small amount of plastic strain suffices to erase the memory of the local, undeformed structure. Surprisingly, essentially one plastic event is enough to bring the local structure to a unique yield stress distribution, disregarding the initial state. The average of this renewal distribution is smaller than the corresponding value computed in the steady state. Remarkably, the average value of the renewal distribution is comparable to the mean local yield stress calculated from the undeformed inherent state of a supercooled liquid equilibrated at  $T = 0.9T_{MCT}$ . This is a clear indication that the temperature which separates brittle and ductile yielding transitions for amorphous materials is close to the mode coupling temperature  $T_{MCT}$ . A contrast between the local yield stresses of initial and renewed sites is necessary, in order to lead to the mechanical instability through shear band formation.

M.L. prepared initial configurations, estimated the mode coupling temperature  $T_{MCT}$  and participated at the discussion of the results during group meetings.

Rejuvenation and shear banding in model amorphous solids

Armand Barbot<sup>1</sup>, Matthias Lerbinger<sup>1</sup>, Anaël Lemaître<sup>2</sup>, Damien Vandembroucq<sup>1</sup> and Sylvain Patinet<sup>1,\*</sup>

<sup>1</sup>PMMH, CNRS, ESPCI Paris, Université PSL, Sorbonne Université, Université de Paris, 75005 Paris, France

<sup>2</sup>Université Paris-Est, Laboratoire Navier (UMR 8205), CNRS, ENPC, IFSTTAR, F-77420 Marne-la-Vallée, France



(Received 23 June 2019; accepted 19 February 2020; published 4 March 2020)

We measure the local yield stress, at the scale of small atomic regions, in a deeply quenched two-dimensional glass model undergoing shear banding in response to athermal quasistatic deformation. We find that the occurrence of essentially a single plastic event suffices to bring the local yield stress distribution to a well-defined value for all strain orientations, thus essentially erasing the memory of the initial structure. It follows that in a well-relaxed sample, plastic events cause the abrupt (nucleation-like) emergence of a local softness contrast and thus precipitate the formation of a band, which, in its early stages, is measurably softer than the steady-state flow. Moreover, this postevent yield stress ensemble presents a mean value comparable to that of the inherent states of a supercooled liquid around the mode-coupling temperature  $T_{MCT}$ . This, we argue, explains that the transition between brittle and ductile yielding in amorphous materials occurs around a comparable parent temperature. Our data also permit to capture quantitatively the contributions of pressure and density changes and demonstrate unambiguously that they are negligible compared with the changes of softness caused by structural rejuvenation.

DOI: [10.1103/PhysRevE.101.033001](https://doi.org/10.1103/PhysRevE.101.033001)

I. INTRODUCTION

Shear banding, an intense localization of plastic strain within narrow bands, is the primary mode of mechanical failure in a variety of amorphous materials including metallic glasses [1] or granular media [2]. When loading conditions permit, bands may extend throughout a piece of material and sustain repeated plastic activity while preserving their overall structure [3]. While it is thus clear that the material inside shear bands is softer than the surrounding, undeformed, glass, the structural origin of this softness contrast, and the mechanisms underlying its rapid emergence, remain highly debated topics [4–8].

Progress on these issues is hampered by basic difficulties in describing the mechanisms of plastic deformation in glasses [9–15]. In these systems, indeed, structural disorder disallows the existence of topological defects akin to crystalline dislocations [16,17], and plasticity results from the intermittent occurrence of local rearrangements (“flips”) triggered when the atoms within “zones” (small regions a few atoms wide) reach mechanical instabilities [18–20]. Although the proximity of a packing to instabilities may correlate with usual observables such as local density, pressure, or shear stress, these correlations are weak [21,22], and the question remains open of their predictive value in the context of shear banding.

Mesoscopic models [23,24] of plasticity represent a glass as an elastic continuum in which zones are embedded. They prove able to reproduce most of the phenomenology of amorphous plastic deformation, in particular the appearance of shear bands, yet only by postulating that local plastic thresholds are weakened after the occurrence of local

rearrangements [25–28]. No atomistic data, however, exist that support this idea.

In this article, we use a recently developed numerical method [22,29,30] that permits to access local yield stress at the zone scale (i.e., in regions a few atoms wide) in arbitrary orientations. This method was previously applied to quenched glasses prior to any plastic deformation. In a companion paper [31], we use it to show that the Bauschinger effect results from plasticity-induced yield strength anisotropies. Here we use this technique to resolve the local yield stress during shear banding. We thus demonstrate that the occurrence of a small amount of plastic strain erases the memory of the local structural properties acquired during aging. Moreover, it brings the average local yield stress, in all shear orientations, to a value smaller than in the steady flow state. The mean yield stress of postevent zones compares with that of supercooled liquid inherent states (ISs) around  $T_{MCT}$ : This explains that the equilibration temperature separating ductile and brittle responses is located in the vicinity of  $T_{MCT}$  [32]. When loading a well-relaxed sample, the suddenness of the rejuvenation process causes a rapid drop in the local yield stress which precipitates the formation of a band that persists over large strain scales thanks to the softness contrast.

II. NUMERICAL METHODS

We use the same atomistic model as in Ref. [30]: a two-dimensional binary system comprising  $10^4$  equal-mass atoms that interact via a Lennard-Jones (LJ) potential with second-order smoothing at cutoff. All values are given in LJ units. Preparation and deformation are performed with periodic boundary conditions at a constant volume corresponding to a density  $\rho \simeq 1.02$ . Samples are prepared via a slow temperature ramp at rate  $\dot{T} = 0.32 \times 10^{-6}$  across the glass transition temperature range. This allows for equilibration

\*sylvain.patinet@espci.fr

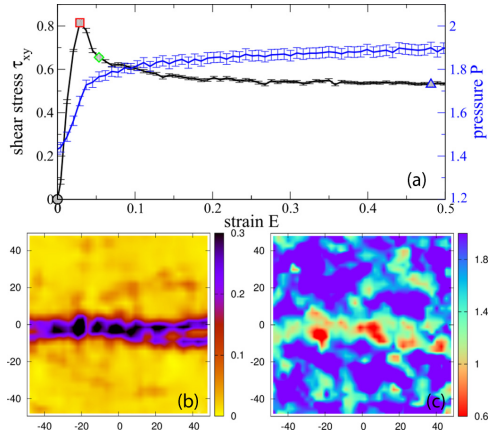


FIG. 1. (a) Mean shear stress  $\tau_{xy}$  (black) and pressure  $P$  (blue) as a function of Hencky's equivalent shear strain  $E$  during simple shear AQS loading. Bottom: Local maps at  $E = 0.05$ ; (b) accumulated strain  $\epsilon$  and (c) yield stress  $\tau_{xy}^c$ .

until the alpha relaxation time is of order  $T_g/\dot{T} \simeq 10^6$ , which corresponds to a fictive temperature  $T_f \simeq 0.29$  as detailed in Appendix A. When reaching  $T = 0.078 T_{MCT}$ , each sample is further quenched by energy minimization to obtain a mechanically equilibrated state. These initial states are then subjected to athermal quasistatic (AQS) [18,33] simple shear deformation along the  $x$  axis up to a linear strain  $\gamma = 5$ , with steps  $\Delta\gamma = 10^{-4}$  and a minimization force tolerance of  $10^{-11}$ . Unless otherwise specified, all averages and distributions are obtained by collecting data from 100 independent samples.

In such strongly deformed systems, local strains must be computed using finite-strain theory (see Appendix B). A scalar measure of local strain  $\epsilon$  is provided by the square root of the second invariant of the logarithmic (Hencky) strain. The macroscopic counterpart of this quantity is  $E = \ln(\gamma/2 + \sqrt{1 + \gamma^2/4})$ .

The sample-averaged stress-strain response during constant-volume AQS loading is reported in Fig. 1(a). It displays a typical stress overshoot followed by softening. As observed in other systems [34], macroscopic pressure  $P$  rises sharply until the peak and continues to grow, albeit more slowly, thereafter. This pressure increase in our constant-volume simulations is the analog of a volume increase in typical fixed-pressure experiments. It is the signature that plastic activity creates configurations that are less well packed than the original aged ones, an idea usually invoked to justify the still classical free-volume theory. We will, however, rule out this interpretation quantitatively by showing that the plastically induced pressure increase, or local density decrease, contributes only a minor fraction of strain softening.

The plastic response of our relaxed systems systematically involves shear banding as illustrated in Fig. 1(b): Local strain

field maps, as shown here at  $E = 0.05$ , typically display a high-strain region crossing the cell throughout. This phenomenon may only arise from structural causes, since our use of AQS shearing rules out the competition between timescales [6], inertia [8], or local heating [4].

Local yield stress values are measured in sheared configurations using the method of Refs. [22,30]. It consists in isolating circular inclusions of radius  $R_{free} = 5$  and straining them by requiring outer atoms to follow an affine motion corresponding to pure shear along an arbitrary orientation  $\alpha \in [0, \pi]$ . Inner, inclusion atoms are free to move nonaffinely and required, using the AQS method, to remain mechanically balanced. The first plastic rearrangement they undergo determines the yield point of the inclusion in orientation  $\alpha$  and defines the local yield stress  $\tau^c(\alpha)$  and critical strain  $\epsilon_c(\alpha)$ . For any considered  $\alpha$ , the yield threshold is thus identified for all inclusions centered at regular grid points. In this article, we primarily focus on the changes in softness that affect the forward barriers, in the loading orientation with  $\alpha = 0$ , due to their direct relevance to the forward plastic response. Yet, we will show [Sec. III C] that softening occurs in all shear orientations, and in particular in the backward one ( $\alpha = \pi/2$ ).

Let us emphasize that we focus here on the threshold  $\tau^c$ , not on the residual strength  $\Delta\tau^c = \tau^c - \tau$ , with  $\tau$  the local stress.  $\Delta\tau^c$  is an adequate predictor of the immediate plastic response [22,30] but explicitly depends on local stress, i.e., on elastic loading.  $\tau^c$  does not and thus constitutes an intrinsic gauge of local glassy structures.

### III. LOCAL YIELD STRESS EVOLUTION

#### A. Shear band profiles

Figure 1(c) presents the resulting local yield stress map in the loading orientation  $\tau^c(\alpha = 0) = \tau_{xy}^c$  at  $E = 0.05$ . When comparing with the strain map of Fig. 1(b), it is strikingly clear that the material in the band tends to present lower yield stress values than the material around it. We thus directly see here that, as expected, plasticity induces softening and thus localization in the band [35]. Below we use this ability to gain insight on the mechanisms underlying the band formation and stability.

To quantify the emergence and evolution of bands, we focus first on samples (53 of 100) where a single band nucleates horizontally.<sup>1</sup> We identify as band center the ordinate  $y_{SB}$  where the  $x$ -averaged local strain reaches its maximum at the macroscopic strain  $E = 0.1$  where the band is clearly visible in all samples. We then report in Fig. 2, as a function of  $y - y_{SB}$ , the  $x$ -averaged strains and yield stresses at several macroscopic strains.

The strain profiles [Fig. 2(a)] clearly show that the band grows over time [13,36]. This would be inaccessible in experiments as the band evolution is usually interrupted by mechanical failure [1]. But, in simulations, since periodic boundary

<sup>1</sup>In 25 samples, a band initially nucleates vertically yet cannot persist due to the simple shear Lees-Edwards boundary conditions: A horizontal band then emerges later. The rest of the samples exhibit more complex behavior and show intermediate crossed configurations, porelike structure [36], and multiple shear bands.

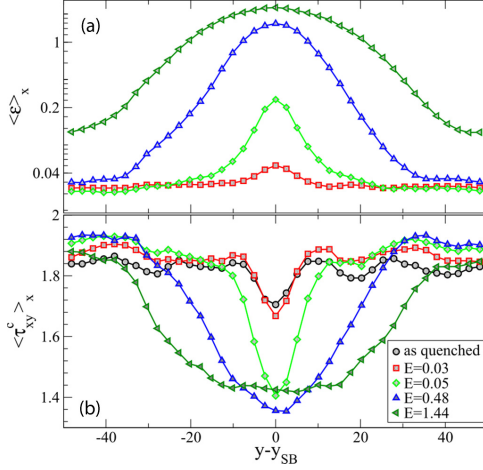


FIG. 2. Local averages computed along the shear direction  $x$  for different strain levels  $E$  as a function of the vertical position  $y$  with respect to the shear band position  $y_{SB}$ : (a) strain  $\langle \epsilon_x \rangle$  and (b) yield stress  $\langle \tau_{xy}^c \rangle$ . The symbols used for the different strain levels are the same as for Fig. 1(a).

conditions maintain the system integrity, the softness contrast eventually resorbs itself and the system reaches a unique, statistically homogeneous, steady flow state [31]. The yield stress profiles [Fig. 2(b)] distinctly show that the softer region coincides with the band and grows at a similar rate. At  $E = 0.05$ , the contrast of local yield stresses between the band and the outer region is of order 27%, in striking agreement with experimental hardness measurements in metallic glasses [37].

Similarly band-centered density, shear modulus, and potential energy profiles are displayed in Appendix C. They show that the band also presents a 2% lower density, a 17% lower shear modulus, and a 5% higher potential energy than the surrounding material. In agreement with Ref. [38], these profiles demonstrate that the position of the band correlates, albeit at different degrees, with the initial values of the considered properties in the quenched state. Although the initial central fluctuation would decrease with system size, this merely illustrates that the AQS response is completely governed by structure. Yet the question remains to understand why softening occurs just after a few percentage strains, thus promoting the formation of the band.

### B. Local yield stress vs. local plastic strain

In this perspective, we report in Fig. 3, for different  $E$ 's, the average yield stress [Fig. 3 (top)] conditioned by the local strain  $\epsilon$  from the quench state. These data are collected from all 100 systems of our ensemble (irrespective of the initial band orientation). The distribution of  $\log_{10}(\epsilon/\epsilon^*)$ , which is the abscissa of this lin-log graph, is reported in the bottom panel and shows a characteristic two-peak structure [20] that separates low-strain, elastically responding regions with the

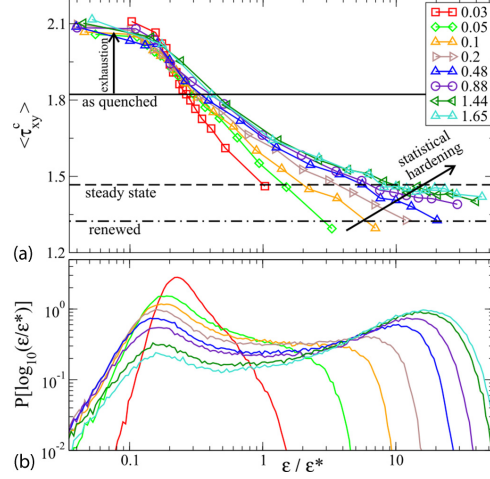


FIG. 3. Top: Average yield stresses  $\langle \tau_{xy}^c \rangle$  as a function of the normalized local strain  $\epsilon/\epsilon^*$  for various macroscopic strain  $E$ . The continuous, dashed, and dash-dotted horizontal lines correspond to  $\langle \tau_{xy}^c \rangle$  in the as-quenched, steady-state, and renewed ensembles, respectively. Bottom: Distribution of  $\log_{10}(\epsilon/\epsilon^*)$ .

high-strain ones, which have undergone local plastic events. As  $E$  increases, the first peak expectedly decreases in amplitude, while the second one grows and shifts rightward, which is expected to result from the accumulation of plastic activity. The crossover strain scale between the two peaks happens to be  $\epsilon^* \simeq 2(\epsilon_c)$ , with  $\langle \epsilon_c \rangle = 0.054$  the average critical strain in the as-quenched state.  $\epsilon^*$  thus corresponds roughly with the scale of the local strain change caused by a plastic rearrangement.

The  $\langle \tau_{xy}^c \rangle$  curves of Fig. 3(a) constitute the first *direct and quantitative* observation of local softening associated with local yielding. They systematically decay with  $\epsilon$ , with a characteristic strain of order  $\epsilon^*$ . This key observation entails that the memory of the initial state is erased with a characteristic strain corresponding to essentially one event. It explains the rapidity of softening and thus localization. Yet there are several features of these curves that are surprising and call for further explanations: (i) the very low strain ( $\epsilon/\epsilon^* \lesssim 0.1$ ), elastic regions present higher yield stress values than the quenched state; (ii) there is a significant spread between the curves, which entails that the local yield stress depends on both  $E$  and  $\epsilon$ ; and, more specifically, (iii) at small  $E$ , highly strained regions are unexpectedly softer than the steady (homogeneous) flow state, so that at a given  $\epsilon$ , the local yield stress grows with  $E$ , which constitutes a hardening effect.

To clarify these issues, we focus on  $E = 0.05$  and distinguish within each configuration two types of local environments: (a) regions where  $\epsilon < \epsilon^*/8$  are called “unyielded” and (b) those where  $\epsilon > 2\epsilon^*$  are called “yielded.” The distributions of local yield stresses in these two subsets are

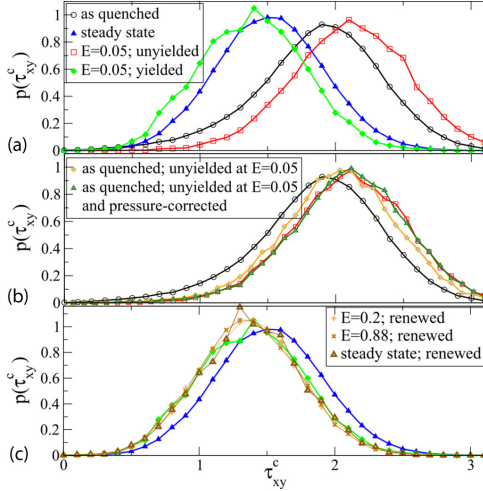


FIG. 4. (a) Distribution of local yield stresses  $\tau_{xy}^c$  in the as-quenched state (black), the steady flow state (blue), at  $E = 0.05$  in the unyielded (red) and yielded (green) areas and the renewed state (shades of brown). [(b) and (c)] The effect of pressure and statistical hardening (see text for details) for the as-quenched state and unyielded sites (b); the steady flow state and yielded sites (c).

shown in Fig. 4, along with their counterparts in the initial as-quenched ensemble and steady homogeneous flow. We find that (A) unyielded regions (mainly outside the shear band) are harder than the as-quenched state and (B) yielded ones are (unexpectedly) softer than the steady flow. The hardening and softening previously noted above under points (i) and (iii)

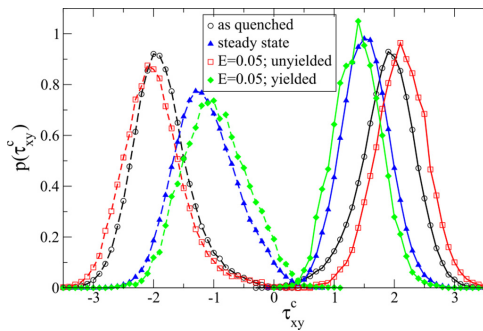


FIG. 5. Distribution of local yield stresses  $\tau_{xy}^c$  in the loading (continuous lines) and reverse directions (dashed lines) in the as-quenched state (black), the steady flow state (blue), at  $E = 0.05$  in the unyielded (red) and yielded (green) areas.

(respectively)<sup>2</sup> hence affect the whole yield stress distribution; in fact, they even occur in all orientations as shown below in Fig. 5.

The hardening of unyielded sites can be attributed primarily to a statistical effect: the progressive elimination (exhaustion) from this ensemble of the weakest sites of the quenched state when they yield [39]. Indeed, if we pick out the unyielded sites at  $E = 0.05$  and plot their yield stress distribution in the initial quenched state [Fig. 4(b), orange diamonds], then we recover the major part of the hardening. The residual difference is entirely attributable to the large (nearly 0.4) pressure increase during loading. Indeed, in unyielded sites,  $\langle \tau_{xy}^c \rangle$  depends roughly linearly, but quite weakly, on  $P$  (see Appendix C), and when both exhaustion and the linear pressure dependence of  $\langle \tau_{xy}^c \rangle$  are taken into account (green triangles), we recover the distribution of yield stress outside shear bands.

We previously observed that yielded sites at finite strains (especially  $E = 0.05$ ) are weaker than the steady flow state. We now show this results from a general property of “freshly renewed,” i.e., postyield sites. To evidence this idea, we pick out sites that yield (i.e., present a local strain change  $\Delta\epsilon > 2\epsilon^*$ ) over a fixed, small amount of macroscopic strain  $\Delta E = 0.05$  (as before), yet starting from different initial states, say, strain  $E$ . Figure 4(c) compares the yield stress distributions in these postyield states for  $E$  values ranging from 0 (as-quenched) to the steady AQS flow state. Strikingly, all these distribution collapse. This constitutes a key observation of our work. It establishes that essentially one plastic event brings the local structure to a unique yield stress distribution, regardless of the initial state.

Note that the final states explored in Fig. 4(c) present sufficiently different pressure levels that we should see systematic deviations from collapse.<sup>3</sup> This is not the case, which implies that the pressure-yield-stress relation is specific to each renewed ensemble as shown in Appendix C: The renewal process does not produce a unique structural “state” but instead a unique yield stress distribution under different conditions. This idea is often speculated to hold in the construction of mean-field [10,40,41] or mesoscale models [25] but was never directly observed. It entails that shear banding results from a process akin to nucleation: the production of structures of a specific softness level after essentially one plastic event.

The hardening of yielded sites with increasing  $E$  then appears to occur due to the rapid elimination, via further yielding, of the weakest among the freshly renewed sites. As  $E$  increases, beyond 0.05, the regions of a fixed  $\epsilon$  comprise an increasing fraction of sites that have yielded early but are strong and have resisted since. This finally explains that the steady flow state is harder than the freshly renewed sites.

<sup>2</sup>These effects can also be seen in the  $\langle \tau_{xy}^c \rangle_x$  profiles of Fig. 2(b) as material outside the band initially hardens, while the middle of the band softens at largest  $E$ 's.

<sup>3</sup>Our renewed ensembles show mean pressure differences up to 0.25 which are expected to correspond to mean yield stress differences  $\approx 0.0625$ .

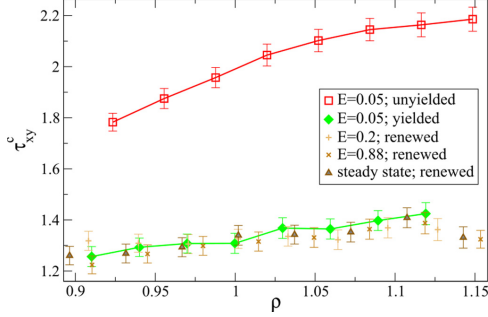


FIG. 6. Average local yield stress  $\langle \tau_{xy}^c \rangle$  as conditioned by local density in unyielded (red) and yielded (green) states at  $E = 0.05$  and in the renewed ensembles (shades of brown).

### C. Local yield stresses in other directions

The distributions of local yield stresses in the forward ( $\alpha = 0$ ) and backward ( $\alpha = \pi/2$ ) global shear directions are shown in Fig. 5. As for the forward simple shear direction investigated above, we report the yielded and unyielded states at  $E = 0.05$ , along with their counterparts in the initial as-quenched ensemble and steady homogeneous flow. Here  $\tau_{xy}^c = \tau^c$  for  $2\alpha = 0$  and  $-\tau^c$  for  $2\alpha = \pi$ , so that forward (respectively, reverse) barriers correspond to positive (respectively, negative) abscissa. The lack of  $\tau_{xy}^c \rightarrow -\tau_{xy}^c$  symmetry in all three deformed ensembles points to a flow-induced anisotropy studied in detail in Ref. [31]. We do not address this effect in this article but focus on the overall changes in softness that affect the forward barriers in the loading orientation. We see here that the rejuvenation process, in particular the strain-softening, occurs in fact in all orientations [31].

### D. Local yield stress vs. free volume

To quantify the possible role of local expansion in softening, we report in Fig. 6  $\langle \tau_{xy}^c \rangle$  as conditioned by local density in both yielded and unyielded site. These data show very clearly that, at the same  $\rho$ , yielded and unyielded sites present sharply different yield stresses: local density, hence, cannot predict local softness. The  $\simeq 2\%$  density difference seen between the band and the outer, elastic, region corresponds to a maximum  $\tau_{xy}^c$  variation of  $\simeq 4\%$ , which is insignificant compared with the observed  $\simeq 27\%$  change in  $\tau_{xy}^c$ . The leading cause of softening is the production by plasticity of packings in a different “state,” i.e., presenting different  $\tau_{xy}^c$  vs.  $\rho$  (or other) relation, than the initial material.

### E. Variation of local yield stresses with parent temperature

We report in Fig. 7 the average  $\langle \tau_{xy}^c \rangle$  computed for inherent states obtained after instantaneous quenches from different parent temperatures of equilibrated liquids. It is noteworthy that the value  $\langle \tau_{xy}^c \rangle \simeq 1.32$  in postyield states is comparable with the average yield stress in the ISs of a supercooled liquid at  $0.9 T_{MCT}$ , a range of temperatures where the dynamics of liquids enters the activated regime. This indicates that

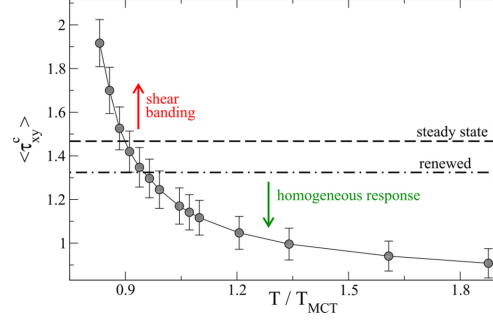


FIG. 7. Average local yield stresses  $\langle \tau_{xy}^c \rangle$  of inherent states as a function of their parent (liquid) temperatures.

postyield structures have comparable barrier heights with a liquid lying on the upper layers of the potential energy landscape (PEL). From this standpoint, the fact that the average yield stress in postyield sites compares with that of liquid ISs near  $T_{MCT}$  appears to constitute a fundamental feature of the PEL. It then explains that the critical parent temperature separating brittle and ductile yielding transitions in amorphous materials is located in the vicinity of  $T_{MCT}$  [32], since a contrast must exist between the yield stress in the initial state and in the postyield sites for shear banding to occur.

Note, however, that we consider here just an average. Furthermore, rearranged and inherent states cannot be strictly compared due to the nonzero polarization in the barrier ensemble along the loading direction [31] and to the slight increase of the pressure in flowing states. Despite this oversimplification, an inherent state obtained near  $T_{MCT}$  is therefore expected to give a good estimate of the stationary threshold distributions and thus act as a limit between softening (leading to strain localization) and hardening regimes in deeply and poorly quenched glasses, respectively [32]. This result is also fully consistent with recent findings obtained in oscillatory shear simulations [42,43], showing that the transition from annealed to yielded behavior is found for parent temperatures in the vicinity of the dynamical crossover temperature  $T_{MCT}$ .

## IV. CONCLUSIONS

All mesoscopic models of amorphous plasticity, starting from the early works by Argon and coworkers [44] to the most recent space-resolved models [24], postulate the existence of local thresholds that are reshuffled during plastic events and affected by local stress. These general assumptions have been guided by mainly two observations. First, plasticity results from the rearrangement of local packings, which suggests it is primarily controlled by local yielding thresholds. Second, it involves avalanche behavior, which implies long-range correlations mediated by elastic deformations. Mesoscopic models attempt to take these two observations into account by separating short scales (local packings, which determine local yield stresses) from large scales, i.e., the requirement of

mechanical balance which couples elastically local stress levels. So, clearly, all mesoscopic models implement, of necessity, the same general script. Yet as soon as one looks at any level of detail beyond these rough guidelines, there is a flurry of such models and no consensus on the proper way to define a reliable one.

The problem is that, until now, as far as we know, no direct observation had been made of local yield thresholds in plastically deformed amorphous media. In the absence of such an observation, it has always remained a question whether the consideration of local yield thresholds was anything more than a simplifying assumption. And the key assumption about the effect of plasticity on local thresholds could only be build on guesswork: For example, it has never been clear whether it was meaningful to assume the existence of a well-defined postyield yield stress distribution. And no test was available for the prediction of models concerning the dynamics of their core state variable: the distribution of these local yield stresses.

The present work, although it does not and cannot solve all these issues, brings hope that they can be addressed rigorously in the near future. It will not alleviate the need to rely on simplifying assumptions, and neither is it intended to provide a recipe for the construction of mesoscopic model—a still distant goal. But it probes the rejuvenation process of atomic-scale yield stresses in a model glass undergoing deformation. Thus, it brings direct observations that strongly constrain both model assumptions, especially about the effect of rejuvenation, and model predictions concerning the dynamics of local thresholds. Thanks to the focus on a system undergoing shear banding, i.e., comprising quite different local packings, we could demonstrate that there was indeed a well-defined postyield yield stress distribution, quite insensitive to the initial ensemble, and we could access it numerically. This is evidently a key input for theories of amorphous plasticity.

Moreover, we found that rejuvenation was an unexpectedly rapid process, essentially requiring a single event to bring the local packing to a well-defined softness level, comparable to that of an IS obtained from a supercooled liquid around  $T_{MCT}$ . This brings several important inputs to theories, specifically concerning our understanding of shear banding in amorphous systems. We showed indeed that the rejuvenation drop in yield stress causes the nucleation-like formation, immediately after the first yield events, of regions of well-defined softness. The rapidity of this process, resulting from the intensity and suddenness of rejuvenation softening, explains that, when starting from a well-relaxed glass, only a few plastic events suffice to locally erase the memory of the initial packing and achieve a soft state, which precipitates the shear banding instability. Also, the closeness of the postyield yield stress distribution to that of a liquid around the crossover region hint at the possibility to explain how the brittle-ductile transition depend on temperature, a very important practical issue.

By providing access to a relevant internal variable that characterizes the local mechanical properties, this work opens promising perspectives for describing nucleation and shear band dynamics in amorphous solids. It also establishes a stimulating link between mechanical and thermal properties, a necessary step to explain how the history of these

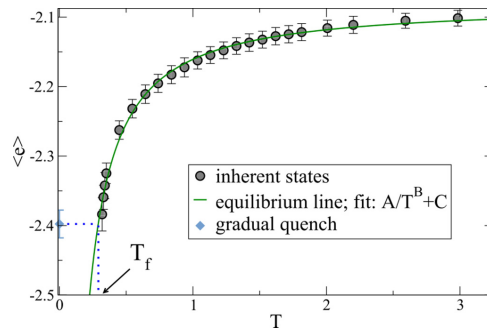


FIG. 8. Inherent-state (IS) potential energy per atom as a function of temperature in equilibrated liquids (gray circles) and in our gradually quenched system (blue diamond). The green line is a fit of the equilibrated liquid data. The fictive temperature  $T_f$  is estimated as that where the liquid IS energy extrapolates to that of the gradually quenched system (see blue dotted lines).

out-of-equilibrium and disordered systems is encoded in their structure [45].

These observations illustrate the remarkable ability of our tool to provide much-needed insights on the local mechanisms of plasticity. We are convinced that a sustained exchange between such numerical probes, which provide both input and benchmarks, and the construction of mesoscopic models, will be instrumental in the coming years for the advancement of our fundamental understanding of amorphous plasticity. We only hope the present work is an early step along this promising route.

#### ACKNOWLEDGMENTS

M.L. and S.P. acknowledge the support of French National Research Agency through the JCJC project PAMPAS under Grant No. ANR-17-CE30-0019-01.

#### APPENDIX A: EFFECTIVE TEMPERATURE SCALES

##### 1. Determination of the fictive temperature

The notion of fictive temperature  $T_f$  is classically used to map a nonequilibrium glass state onto an equilibrium liquid. Following Ref. [46], the fictive temperature of our gradually quenched glass is defined using the inherent state potential energy: Namely,  $T_f$  is defined (see Fig. 8) as the temperature at which the inherent potential energy of the glass equates that of equilibrated liquids. We obtain  $T_f = 0.291 \pm 0.007$ .

##### 2. Determination of the mode-coupling temperature

The mode-coupling temperature  $T_{MCT}$  is determined from a functional fit of the relaxation time  $\tau_\alpha$  in the dynamical regime for different temperatures  $T$  [47,48]. We first compute the self-intermediate scattering function  $F_L(\mathbf{q}, t) = \langle \cos(\mathbf{q} \cdot (\mathbf{r}_j(t) - \mathbf{r}_j(0))) \rangle$ , where the subscript  $L$  refers to the “large” particles,  $\mathbf{r}_j(t)$  is the position of the  $j$ th particle at time  $t$ , and  $\langle \dots \rangle$  denotes the average over  $j$  and the time origin.  $F_L(\mathbf{q}, t)$

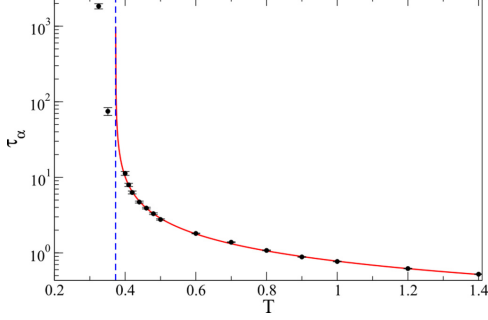


FIG. 9. Relaxation time  $\tau_\alpha$  as a function of the equilibration temperature. The red line is a power-law fit of the data points for temperatures larger than 0.4. The vertical blue line represents the location of estimated  $T_{MCT}$ .

is averaged over 100 samples, containing 1024 atoms each, for every temperature. We define the relaxation time  $\tau_\alpha$  as  $F_L(\mathbf{q}_{SF}, t = \tau_\alpha) = \frac{1}{\rho}$  with  $|\mathbf{q}_{SF}| = 6.07$  corresponding to the primary peak of the static structure factor. As reported in Fig. 9,  $\tau_\alpha$ , as computed for temperatures larger than 0.4, is well fitted by the power-law relation  $\tau_\alpha \propto (T - T_{MCT})^\gamma$ . We obtain  $\gamma = -0.818 \pm 0.005$  and  $T_{MCT} = 0.373 \pm 0.001$ .

## APPENDIX B: STRAIN MEASURES

### 1. Hencky equivalent global shear-strain

Our model glasses are deformed using AQS simple shear loading up to linear strains  $\gamma_{xy} = 500\%$ . The global strain is characterized within the finite-strain theory by using a Lagrangian description and choosing the Hencky's logarithmic strain definition [49]. The advantages of proceeding in such a way are threefold: It makes no use of small strain approximation, it allows us to eliminate rotations, and it will permit us to characterize macroscopic and microscopic strains using comparable quantities.

Given  $\mathbf{F}$  as the deformation gradient, the logarithmic (Hencky) strain is  $\mathbf{E} = \ln(\mathbf{U})$ , where  $\mathbf{U}$  is the right stretch tensor, i.e., the unique symmetric and positive-definite tensor such that  $\mathbf{F} = \mathbf{R}\mathbf{U}$ , with  $\mathbf{R}$  a rotation. Since the right Cauchy-Green strain

$$\mathbf{F}^T \mathbf{F} = \mathbf{U}^2 \quad (\text{B1})$$

is positive definite, we may also write  $\mathbf{E} = \frac{1}{2} \ln(\mathbf{U}^2)$ . Moreover,  $\mathbf{U}^2$  can be diagonalized, i.e., written as  $\mathbf{U}^2 = \mathbf{P}^{-1} \mathbf{D} \mathbf{P}$  with  $\mathbf{D}$  diagonal and  $\mathbf{P}$  the associated change of basis matrix. Finally, the invariants of  $\mathbf{E} = \mathbf{P}^{-1} \ln(\mathbf{D}) \mathbf{P}$  are those of  $\ln(\mathbf{D})$ .

For two-dimensional simple shear deformation, the deformation gradient is

$$\mathbf{F} = \begin{pmatrix} 1 & \gamma \\ 0 & 1 \end{pmatrix} \quad (\text{B2})$$

with  $\gamma$  the linear strain and the right Cauchy-Green strain

$$\mathbf{U}^2 = \begin{pmatrix} 1 & \gamma \\ \gamma & 1 + \gamma^2 \end{pmatrix}. \quad (\text{B3})$$

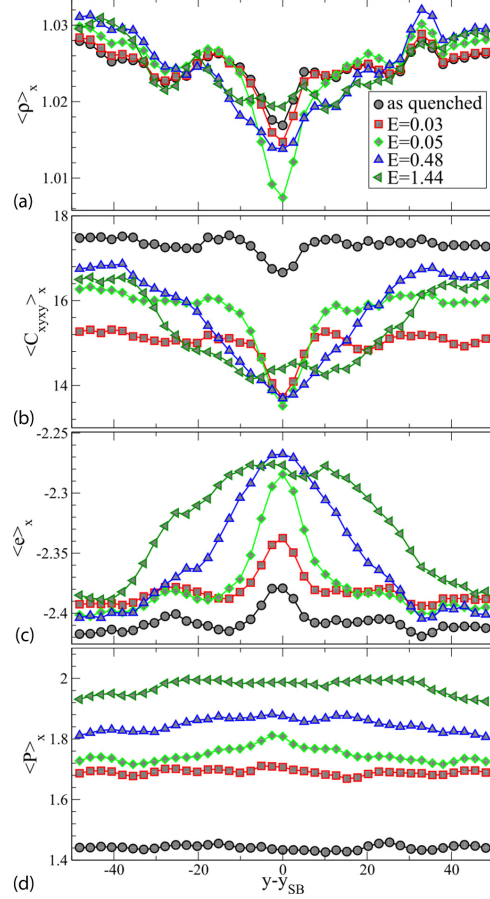


FIG. 10. Local averages computed along the shear direction  $x$  for different strain levels  $E$  as a function of the vertical position  $y$  with respect to the shear band position  $y_{SB}$ : (a) density  $\langle \rho \rangle_x$ , (b) shear modulus in the loading direction  $\langle C_{xyxy} \rangle_x$ , (c) potential energy per atom  $\langle e \rangle_x$ , and (d) pressure  $\langle P \rangle_x$ .

Its eigenvalues are  $\lambda_{\pm} = (\frac{\gamma}{2} \pm \sqrt{1 + \frac{\gamma^2}{4}})^2$ . Noting that  $\lambda_+ \lambda_- = 1$ , since  $\det(\mathbf{U}^2) = 1$ , the square-root of the second tensor invariant of  $\mathbf{E}$ ,  $E \equiv \frac{1}{4} |\ln(\lambda_+ / \lambda_-)| = \ln(\frac{\gamma}{2} + \sqrt{1 + \frac{\gamma^2}{4}})$ . This is the quantity we refer to in the manuscript as the macroscopic Hencky strain.

### 2. Local strain computation

The procedure for computing local strain tensor in our atomic system is the same as that previously employed in Refs. [22,30]. It relies on the evaluation of the local, coarse-grained, deformation gradient tensor  $\mathbf{F}$ .

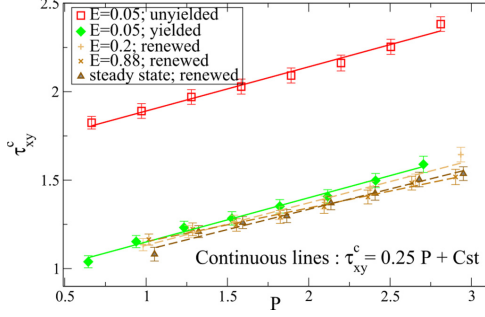


FIG. 11. Local yield stress  $\tau_{xy}^c$  as conditioned by local pressure  $P$  in yielded (green) and unyielded (red) regions at  $E = 0.05$  and for renewed sites (shades of brown) at different macroscopic strains.

In continuum mechanics  $\mathbf{F}$  relates the position in the reference (undeformed) configuration to the current (deformed) configuration through the Cauchy-Born rule. For an atomic system under affine deformation this mapping relates the vectors  $\mathbf{X}^{\alpha\beta}$  and  $\mathbf{x}^{\alpha\beta}$  connecting atoms  $\alpha$  and  $\beta$  in the reference and current configurations (respectively) by

$$x_{ij}^{\alpha\beta} = F_{ij} X_{ij}^{\alpha\beta} \quad (\text{B4})$$

with  $i$  and  $j$  coordinate components. Since local strains are not affine in general (particularly in glasses [50]) the previous formula will no longer be exact for each individual atom-neighbor pair.

For two configurations separated by a small macroscopic strain interval, as proposed by Zimmerman *et al.* [51], we define the atomic-level deformation tensor  $F_{ij}^\alpha$  for atom  $\alpha$  by minimizing the function

$$B^\alpha = \sum_{\beta=1}^n \sum_{i=1}^2 g(r_0^{\alpha\beta}) (x_i^{\alpha\beta} - F_{ij}^\alpha X_j^{\alpha\beta})^2, \quad (\text{B5})$$

where the sum runs over the  $n$  nearest neighbors of  $\alpha$  and where  $g(r_0^{\alpha\beta})$  is a smooth weighting function that only depends on the distance  $r_0^{\alpha\beta}$  between atoms  $\alpha$  and  $\beta$  in the reference configuration [38]. Thus  $F_{ij}^\alpha$  is the best fit of Eq. (B4), in the least-squares sense, for an atom in its cage. We choose for  $g$  an octic polynomial function [52]. This function has a single maximum and continuously vanishes at a coarse-graining length  $R_{CG} = 5$ :

$$g(r) = \begin{cases} \frac{15}{8\pi R_{CG}^8} \left[ 1 - 2\left(\frac{r}{R_{CG}}\right)^4 + \left(\frac{r}{R_{CG}}\right)^8 \right], & \text{for } r < R_{CG} \\ 0, & \text{otherwise.} \end{cases} \quad (\text{B6})$$

The minimization of Eq. (B5) with respect to  $\mathbf{F}^\alpha$  gives

$$F_{ij}^\alpha = \sum_{k=1}^2 Y_{ik} Z_{jk}^{-1}, \quad (\text{B7})$$

with

$$Y_{ik} = \sum_{\beta=1}^n (X_i^{\alpha\beta} X_k^{\alpha\beta}) g(r_0^{\alpha\beta}) \quad \text{and} \quad Z_{ik} = \sum_{\beta=1}^n (X_i^{\alpha\beta} X_k^{\alpha\beta}) g(r_0^{\alpha\beta}). \quad (\text{B8})$$

This procedure is used to compute the strain gradient for each atom  $\mathbf{F}$  between macroscopic configuration separated by small strain intervals  $\Delta\gamma = 0.01$ . For larger  $\Delta\gamma$ ,  $\mathbf{F}$  is numerically integrated by multiplying the deformation gradient tensors  $\mathbf{F} = \mathbf{F}_n \mathbf{F}_{n-1} \cdots \mathbf{F}_2 \mathbf{F}_1$ , where  $\mathbf{F}_i$  is the deformation gradient tensors between states  $i$  and  $i+1$  separated by  $\Delta\gamma = 0.01$ .

The local strain is reduced to a scalar following the same procedure as for the global strain  $E$ , which involves the numerical diagonalization of each  $\mathbf{F}^T \mathbf{F}$ . Finally, the atomic-level strain  $\epsilon$  is defined as the second tensor invariant of  $\frac{1}{2} \ln(\mathbf{F}^T \mathbf{F})$ .

The  $\epsilon$  field is then evaluated on a square grid  $N^2$  by assigning to each grid point the value computed for the closest corresponding atom. The regular grid lattice constant equals to  $R_{\text{sampling}} = L/39 \approx R_{\text{cut}}$ , where  $L$  is the dimension of the initially square simulation box and  $R_{\text{cut}} = 2.5\sigma$  is the cutoff interatomic potential. The grid deforms affinely with the overall applied strain in simple shear. The local yield stresses are computed on the same grid.

## APPENDIX C: LOCAL PROPERTIES

### 1. Profiles through the shear band

In Fig. 10, we report the average profiles of density  $\rho$ , elastic modulus  $C_{xyxy}$ , potential energy per atom  $e$ , and pressure  $P$  for different macroscopic strain levels. As described in the manuscript, we restrict this analysis to samples featuring only horizontal shear bands. The profiles are centered on the shear band ordinate  $y_{\text{SB}}$ , which is defined at that where the  $x$ -averaged local strain is maximum for  $E = 0.1$ .

The values of  $\langle \rho \rangle_x$ ,  $\langle C_{xyxy} \rangle_x$ , and  $\langle e \rangle_x$  in the shear band and the outer medium are visibly contrasted: The accumulation of plastic rearrangements brings the system to a less dense, less rigid, and less stable state. Note, however, that all profiles eventually become homogeneous in the stationary flow state.

Because of the constant volume loading protocol, the average of  $\rho$  is by definition equal to the mean system density. The local density in the band thus reaches transiently a minimum around  $E \simeq 0.05$  before increasing again toward the mean density, its eventual value at large macroscopic strains.

The evolution of the elastic moduli is somewhat curious. While it softens in the band,  $\langle C_{xyxy} \rangle_x$  presents an overall decrease during the early stages of loading up to the peak stress. This is expected since the approach to plastic instabilities reduces the macroscopic elastic modulus [18]. The moduli in the outer, elastic region then rapidly rises as the stress decreases from its peak, presumably because the density of near threshold zone diminishes.

The presence and broadening of the shear band can also be detected by examining the increase in  $\langle e \rangle_x$ . This increase has already been observed in a very similar atomic system [13], where it has been interpreted as a rise in effective temperature through shear-transformation-zone theory.

It is interesting to note that the shear band position at  $E = 0.1$ , which we take as reference, correlates with various local properties of the quenched state. Note, finally, that if the global pressure increases with plastic deformation (see Fig. 1 in the manuscript), then it is almost homogeneous along these average profiles due to mechanical equilibrium as reported in Fig. 10(d).

**2. Variation of local yield stresses with pressure**

We report in Fig. 11 the average of  $\langle \tau_{xy}^c \rangle$  as a function of the local pressure  $P$  in the yielded and nonyielded regions at  $E = 0.05$  and for renewed states (see manuscript) for different macroscopic strains. This plot clearly shows that, at the same  $P$ , unyielded and yielded regions present different yield stresses. Moreover, in either ensemble, the local yield stress increases nearly linearly with local pressure. This result is in agreement with the variation of the yield surface obtained numerically for a metallic glass in Ref. [53], where pressure or normal stress give results intrinsically similar to a Mohr-Coulomb criterion. The slopes of the  $\langle \tau_{xy}^c \rangle$  relations differ by

merely 10%. We therefore choose to adjust the slope on all the data. We find an empirical relationship for yielded and unyielded sites:  $\langle \tau_{xy}^c \rangle = 0.25 P + A$ , where  $A$  is a constant.

Using the identified slope of the local relation between  $\tau_{xy}^c$  vs.  $P$ , we can now take into account the effect of local pressure and correct the data in Fig. 4(b) of the manuscript. We calculate the threshold distribution of unyielded sites at  $E = 0.05$  from the corresponding thresholds in the quenched state as  $\tau_{xy}^c = \tau_{xy}^c(E = 0)E = 0.05, \epsilon < \langle \epsilon^* \rangle / 8 + 0.25 \Delta P$ , where  $\Delta P$  is the variation of local pressure on given sites between  $E = 0$  and  $E = 0.05$ . The corrected curves [green triangles in Fig. 4(b) in the manuscript] quantitatively reproduce the distributions  $\tau_{xy}^c$  of unyielded sites at  $E = 0.05$ . This establishes that changes in the local yield stress for small deformations, mainly outside of the band, can be attributed both to the depletion of weak sites and, in the case of constant volume simulations, to the increase in local pressure.

The relation between  $\langle \tau_{xy}^c \rangle$  and  $P$  for the renewed states at different macroscopic strains still shows a nearly linear dependency. It, however, slightly deviates from the relation found for the yielded sites at  $E = 0.05$ .

[1] A. Greer, Y. Cheng, and E. Ma, *Mater. Sci. Eng. R Rep.* **74**, 71 (2013).  
 [2] A. Le Bouil, A. Amon, S. McNamara, and J. Crassous, *Phys. Rev. Lett.* **112**, 246001 (2014).  
 [3] C. Pampillo and H. Chen, *Mater. Sci. Eng.* **13**, 181 (1974).  
 [4] J. J. Lewandowski and A. L. Greer, *Nature Mat.* **5**, 15 (2006).  
 [5] C. A. Schuh, T. C. Hufnagel, and U. Ramamurty, *Acta Mater.* **55**, 4067 (2007).  
 [6] K. Martens, L. Bocquet, and J.-L. Barrat, *Soft Matter* **8**, 4197 (2012).  
 [7] S. V. Ketov and D. V. Louzguine-Luzgin, *Sci. Rep.* **3**, 2798 (2013).  
 [8] A. Nicolas, J.-L. Barrat, and J. Rottler, *Phys. Rev. Lett.* **116**, 058303 (2016).  
 [9] F. Spaepen, *Acta Metall.* **25**, 407 (1977).  
 [10] P. Sollich, F. Lequeux, P. Hébraud, and M. E. Cates, *Phys. Rev. Lett.* **78**, 2020 (1997).  
 [11] M. L. Falk and J. S. Langer, *Phys. Rev. E* **57**, 7192 (1998).  
 [12] M. L. Manning, J. S. Langer, and J. M. Carlson, *Phys. Rev. E* **76**, 056106 (2007).  
 [13] Y. Shi, M. B. Katz, H. Li, and M. L. Falk, *Phys. Rev. Lett.* **98**, 185505 (2007).  
 [14] Y. Sun, A. Concustell, and A. L. Greer, *Nat. Rev. Mater.* **1**, 16039 (2016).  
 [15] Y. Tong, W. Dmowski, H. Bei, Y. Yokoyama, and T. Egami, *Acta Mater.* **148**, 384 (2018).  
 [16] H. Mecking and U. F. Kocks, *Acta Metall.* **29**, 1865 (1981).  
 [17] J. Ding, S. Patinet, M. L. Falk, Y. Cheng, and E. Ma, *Proc. Natl. Acad. Sci. USA* **111**, 14052 (2014).  
 [18] C. Maloney and A. Lemaître, *Phys. Rev. Lett.* **93**, 195501 (2004).  
 [19] A. Tanguy, F. Leonforte, and J.-L. Barrat, *Eur. Phys. J. E* **20**, 355 (2006).  
 [20] A. Lemaître and C. Caroli, *Phys. Rev. E* **76**, 036104 (2007).  
 [21] M. Tsamados, A. Tanguy, C. Goldenberg, and J.-L. Barrat, *Phys. Rev. E* **80**, 026112 (2009).  
 [22] S. Patinet, D. Vandembroucq, and M. L. Falk, *Phys. Rev. Lett.* **117**, 045501 (2016).  
 [23] B. Tyukodi, S. Patinet, S. Roux, and D. Vandembroucq, *Phys. Rev. E* **93**, 063005 (2016).  
 [24] A. Nicolas, E. E. Ferrero, K. Martens, and J.-L. Barrat, *Rev. Mod. Phys.* **90**, 045006 (2018).  
 [25] D. Vandembroucq and S. Roux, *Phys. Rev. B* **84**, 134210 (2011).  
 [26] D. Tüzes, P. D. Ispánovity, and M. Zaiser, *Int. J. Fract.* **205**, 139 (2017).  
 [27] D. F. Castellanos and M. Zaiser, *Phys. Rev. Lett.* **121**, 125501 (2018).  
 [28] M. Popovic, T. W. J. de Geus, and M. Wyart, *Phys. Rev. E* **98**, 040901(R) (2018).  
 [29] F. Puosi, J. Olivier, and K. Martens, *Soft Matter* **11**, 7639 (2015).  
 [30] A. Barbot, M. Lerbinger, A. Hernandez-Garcia, R. García-García, M. L. Falk, D. Vandembroucq, and S. Patinet, *Phys. Rev. E* **97**, 033001 (2018).  
 [31] S. Patinet, A. Barbot, M. Lerbinger, D. Vandembroucq, and A. Lemaître, *arXiv:1906.09818*.  
 [32] M. Ozawa, L. Berthier, G. Biroli, A. Rosso, and G. Tarjus, *Proc. Natl. Acad. Sci. USA* **115**, 6656 (2018).  
 [33] C. E. Maloney and A. Lemaître, *Phys. Rev. E* **74**, 016118 (2006).  
 [34] M. Utz, P. G. Debenedetti, and F. H. Stillinger, *Phys. Rev. Lett.* **84**, 1471 (2000).  
 [35] J. R. Rice, in *Theoretical and Applied Mechanics: Proceedings of the 14th International Congress on Theoretical and Applied Mechanics, Delft, 1976*, edited by W. T. Koiter, Vol. 1 (North Holland Publishing Co., Amsterdam, 1976), pp. 207–220.

- [36] D. D. Alix-Williams and M. L. Falk, *Phys. Rev. E* **98**, 053002 (2018).
- [37] J. Pan, Q. Chen, L. Liu, and Y. Li, *Acta Mater.* **59**, 5146 (2011).
- [38] A. R. Hinkle, C. H. Rycroft, M. D. Shields, and M. L. Falk, *Phys. Rev. E* **95**, 053001 (2017).
- [39] J.-C. Baret, D. Vandembroucq, and S. Roux, *Phys. Rev. Lett.* **89**, 195506 (2002).
- [40] J. P. Bouchaud, *J. Phys. I France* **2**, 1705 (1992).
- [41] P. Hébraud and F. Lequeux, *Phys. Rev. Lett.* **81**, 2934 (1998).
- [42] W.-T. Yeh, M. Ozawa, K. Miyazaki, T. Kawasaki, and L. Berthier, [arXiv:1911.12951](https://arxiv.org/abs/1911.12951).
- [43] H. Bhaumik, G. Foffi, and S. Sastry, [arXiv:1911.12957](https://arxiv.org/abs/1911.12957).
- [44] V. V. Bulatov and A. S. Argon, *Modell. Simul. Mater. Sci. Eng.* **2**, 167 (1994).
- [45] N. C. Keim, J. Paulsen, Z. Zeravcic, S. Sastry, and S. R. Nagel, *Rev. Mod. Phys.* **91**, 035002 (2019).
- [46] C. Liu, P. Guan, and Y. Fan, *Acta Mater.* **161**, 295 (2018).
- [47] T. B. Schröder, S. Sastry, J. C. Dyre, and S. C. Glotzer, *J. Chem. Phys.* **112**, 9834 (2000).
- [48] A. Cavagna, *Phys. Rep.* **476**, 51 (2009).
- [49] P. Neff, B. Eidel, and R. Martin, [arXiv:1402.4027](https://arxiv.org/abs/1402.4027).
- [50] S. Saw, S. Abraham, and P. Harrowell, *Phys. Rev. E* **94**, 022606 (2016).
- [51] J. A. Zimmerman, D. J. Bammann, and H. Gao, *Inter. J. Sol. Struct.* **46**, 238 (2009).
- [52] A. Lemaître, *Phys. Rev. Lett.* **113**, 245702 (2014).
- [53] A. C. Lund and C. A. Schuh, *Acta Mater.* **51**, 5399 (2003).





## RÉSUMÉ

---

Dans cette thèse, la méthode de la limite d'élasticité locale est appliquée et approfondie pour étudier d'une part les réarrangements atomiques isolés et irréversibles induits par cisaillement et d'autre part la relaxation structurale dans un liquide formateur de verre, un mélange binaire Lennard-Jones 2D. La méthode permet d'obtenir la réponse mécanique locale d'un état inhérent de manière directe et non-perturbative tout en contrôlant les échelles de longueur et les directions de chargement. Dans la première partie, l'accent est mis sur une petite inclusion du verre. Sa réponse micromécanique est sondée dans la limite athermique quasi-statique. L'influence de l'échelle de longueur, sur laquelle la réponse mécanique est sondée, est discutée. La variation des statistiques de seuil en fonction de la taille de la zone de sondage peut être comprise sur la base d'un argument géométrique simple et d'une hypothèse de maillon faible. Ensuite, en déterminant la limite d'élasticité critique locale avec une résolution angulaire élevée sur la direction de chargement, on observe que seul un nombre fini et discret de réarrangements de cisaillement est accessible, chacun d'eux se caractérisant par un plan faible distinct. De plus, la limite d'élasticité critique montre une grande sensibilité à la pression. On constate que pour l'échelle de longueur étudiée, le critère d'élasticité de Mohr-Coulomb décrit par morceaux la contrainte de cisaillement critique avec précision. Dans la deuxième partie, un lien fort entre la structure et la dynamique des liquides surfondus est établi. La nouveauté du présent travail est la caractérisation de la structure par des seuils de glissement locaux. Une forte corrélation est trouvée entre d'une part les barrières de contrainte dans la direction la plus faible calculée dans l'état inhérent et d'autre part les observables associées à la relaxation de la structure à l'état liquide. Comme attendu, un coefficient de corrélation plus élevé est constaté pour les liquides équilibrés à des températures plus basses, signe que le paysage d'énergie potentielle influence davantage la dynamique.

## MOTS CLÉS

---

Micro-mécanique, Solide amorphe, Liquide surfondu, Dynamique moléculaire

## ABSTRACT

---

In this thesis, the local yield stress method is applied and extended to study single, irreversible atomistic rearrangements as well as structural relaxation in a model glass-forming liquid, a two dimensional binary Lennard-Jones mixture. The method gives access to the local mechanical response of an inherent configuration in a direct and non-perturbative manner while controlling the length scales and loading directions. In the first part, the focus is on a small inclusion of the glass. Its micromechanical response is probed in the athermal quasi-static limit. The influence of the length scale, at which the mechanical response is probed, is discussed. The variation of the threshold statistics with the size of the probing zone can be understood on the basis of a simple geometric argument and a weakest link assumption. Then, upon determining the dependence of the local critical yield stress on the shear loading direction with a high angular resolution, it is observed that only a finite and discrete number of shear rearrangements is accessible, each of them having a distinct weak plane. Furthermore, the critical yield stress shows a high sensitivity towards the pressure in the simulation box. It is found that for the length scale studied, a Mohr-Coulomb yield criterion describes piecewise accurately the critical shear stress. In the second part, a connection between structure and dynamics of model supercooled liquids is established. The novelty in the present work is the characterization of the structure through local slip thresholds. A strong correlation is found between the stress barriers in the softest direction calculated in the as-quenched state and observables associated to the relaxation of the liquid structure at parent temperature. As expected, a higher correlation coefficient is detected for liquids equilibrated at lower temperatures, as the potential energy landscape increasingly influences the dynamics.

## KEYWORDS

---

Micromechanic, Amorphous solid, Supercooled liquid, Molecular dynamics